

DNA-CONJUGATED MAGNETIC NANOPARTICLES FOR BIO-ANALYTICAL AND  
BIOMEDICAL APPLICATIONS

By

SUWUSSA BAMRUNGSAP

A DISSERTATION PRESENTED TO THE GRADUATE SCHOOL  
OF THE UNIVERSITY OF FLORIDA IN PARTIAL FULFILLMENT  
OF THE REQUIREMENTS FOR THE DEGREE OF  
DOCTOR OF PHILOSOPHY

UNIVERSITY OF FLORIDA

2011

© 2011 Suwussa Bamrungsap

To my family

## ACKNOWLEDGMENTS

I am truly grateful to a long list of people. None of my success would have been possible without them. I would like to express my gratitude to my research advisor, Dr. Weihong Tan, for providing continuous guidance, support, and opportunities for my research and life throughout my PhD studies. His valuable inspiration and advices encourage me to have scientific thought which will definitely have a great impact for my future career and life.

I am pleased to thank my doctoral dissertation committee members, Dr. Alexander Angerhofer, Dr. Charles Cao, Dr. Gail Fanucci, and Dr. Christopher Batich for the helpful discussion and constructive comments. I would like to thank Dr. Benjamin Smith for all help and support during my five-year at University of Florida. I also thank The Royal Thai government for the graduate stipend and tuition fees during my whole PhD studies.

This dissertation is a result from successful collaboration with many scientists. I especially thank Dr. Yu-Fen Huang, Dr. Joshua Smith, and Dr. Colin Medley for introducing me into the nanomaterial fields, guiding, and training me in the early states of research. I also would like to express my appreciation to Dr. Kathryn Williams, Dr. Joseph Phillips, Dr. Ibrahim Shukoor, Dr. Kwame Sefah, Dr. Youngmi Kim, Dr. Arthur Hebard, and Dr. Swadeshmukul Santra for many helpful research discussions, experimental help, and all suggestions on different projects. I really appreciate Dr. Yan Chen, Dr. Zhi Zhu and Hui Wang as being supportive friends and colleagues, as well as their encouragement during my difficult times.

It has been a great experience to spend several years in the Tan research group with both previous and current group members. I would like to thank Dr. Marie Carmen

Estevez, Dr. Jilin Yan, Dr. Xiaoling Zhang, Dr. Liu Yang, Dr. Heipeng Liu, Dr. Jennifer Martin, Dr. Huaizhi Kang, Dalia Lopez Colon, Xiangling Xiong, Dimitri Van Simaey, Meghan O'Donoghue, Basri Gulbaken, Tao Chen, and others for their help and friendship.

I also would like to express special thanks to my friends Jean Palmes, Preeyanan Sriwanayos, Aay Pawinee, Pattaraporn Vanachayangkul, Witcha Imaram, and Werachart Ratanatharathorn for valuable friendship. I deeply appreciate them for being supportive during my difficult times, and sharing the good moments.

Finally, without my family, especially my parents, Somkuan and Wasana, none of this would have been possible. I sincerely thank for their continuous dedication, endless support, and constant encouragement. Their unconditional love and great attitude make me become who I am and keep me always moving on.

## TABLE OF CONTENTS

	<u>page</u>
ACKNOWLEDGMENTS .....	4
LIST OF TABLES.....	9
LIST OF FIGURES .....	10
ABSTRACT.....	13
CHAPTER	
1 INTRODUCTION.....	16
Impact of Nanoparticles for Bio-analytical Applications .....	16
Magnetic Iron Oxide Nanoparticle Fundamentals.....	18
Synthesis of Iron Oxide Nanoparticles .....	19
Iron Oxide Nanoparticle Surface Modification and Bioconjugation.....	21
Size, Shape, Magnetic properties and Surface Characterization .....	23
Magnetic Nanoparticles for Magnetic Resonance (MR) Based Assays.....	24
Basic Concept of Magnetic Resonance Imaging (MRI).....	26
Magnetic nanoparticles (MNPs) and $T_2$ relaxation.....	27
Magnetic Relaxation Switches (MRSw) .....	30
Mechanism of magnetic relaxation switches (MRSw).....	31
Instrumentation for MRSw .....	32
Nucleic Acid Probes .....	33
Selective Biorecognition Elements .....	34
DNA Molecular Machines.....	37
DNA switches .....	37
DNA walkers.....	38
DNA motors .....	39
Fluorescence Techniques for Signal Transduction.....	40
Jablonski Diagram .....	40
Fluorescence Quenching .....	41
Fluorescence Resonance Energy Transfer (FRET) .....	43
2 MOLECULAR PROFILING OF CANCER CELLS USING APTAMER- CONJUGATED MAGNETIC NANOPARTICLES.....	54
Introduction.....	54
Experimental Section.....	56
Synthesis of DNA Aptamers.....	56
Aptamer-Nanoparticle Conjugation .....	57
Cells and Culture Conditions.....	57
Determination of Conjugated Nanoparticle-Cell Specific Targeting .....	58
Sample Assays using Spin-Spin Relaxation Time Measurement.....	59

Results and Discussion .....	59
Magnetic Nanosensor Preparation.....	59
Specificity of ACMNPs .....	60
Cancer Cells Detection using Spin-spin Relaxation Time Measurement .....	60
Detection in Complex Biological Media .....	61
Detection in Mixture of Cells .....	62
Cancer Cells Profiling.....	63
Conclusion.....	64
3 DETECTION OF LYSOZYME USING MAGNETIC RELAXATION SWITCHES BASED ON APTAMER-FUNCTIONALIZED SUPERPARAMAGNETIC NANOPARTICLES .....	72
Introduction.....	72
Experimental Section.....	74
Synthesis of DNA.....	74
Lys Nanosensor Preparation.....	74
Magnetic Relaxation Measurement.....	75
Cell Samples Preparation .....	75
Results and Discussion .....	76
Clusters Formation of Lys Nanosensor .....	77
Lys-Induced Disassembly of Nanosensors .....	77
Selectivity and Specificity of Lys Nanosensors .....	78
Quantitative Analysis of Lysozyme .....	79
Analysis of Lysozyme in Cell Lysates .....	80
Conclusion.....	81
4 MAGNETICALLY DRIVEN SINGLE DNA NANOMOTOR .....	87
Introduction.....	87
Experimental Section.....	88
DNA Molecular Probes Synthesis .....	88
Molecular Probes Assays.....	89
Immobilization of DNA Molecular Probes on Glass Surface .....	90
Construction of DNA Nanomotor.....	91
Results and Discussion .....	92
Signal Enhancement of the DNA Molecular Probes by Dnase I Cleavage.....	93
DNA Nanomotor Driven by Magnetic Field .....	94
Conclusion.....	98
5 SUMMARY AND FUTURE DIRECTIONS .....	105
The Development of DNA-Conjugated Magnetic Nanoparticles for Bio-Analytical and Biomedical Applications .....	105
Future Directions .....	107
LIST OF REFERENCES.....	111

BIOGRAPHICAL SKETCH .....120

## LIST OF TABLES

<u>Table</u>		<u>page</u>
2-1	Representative cell lines and binding affinities of their selected aptamers.....	71
3-1	List of DNA sequences.....	86
3-2	The formation of magnetic clusters upon hybridization between complementary strands.....	86
4-1	DNA hairpins and biotinylated linker .....	104
4-2	The average signal enhancement of nanomotor after repeating several cycles. ....	104

## LIST OF FIGURES

<u>Figure</u>	<u>page</u>
1-1 Nanoparticle size effects on magnetism.....	45
1-2 Scheme representing the Stöber process .....	45
1-3 Scheme representing a water-in-oil (W/O) microemulsion system.....	46
1-4 Representative bioconjugation schemes for attaching biomolecules to NPs for bioanalysis .....	46
1-5 Principal of magnetic resonance imaging (MRI).....	47
1-6 The role of magnetic nanoparticles as contrast agents .....	47
1-7 Magnetic nanoparticle size and dopant effects on mass magnetization (Ms) and MRI contrast enhancement. ....	48
1-8 Magnetic nanoparticle aggregation effects on MRI. ....	49
1-9 Principle of magnetic relaxation switches (MRSw).....	49
1-10 DNA and RNA structures formed by phosphodiester linkages. ....	50
1-11 Structure of DNA double helix and base pairing.....	50
1-12 Schematic representation of DNA aptamer selection using the cell-SELEX strategy .....	51
1-13 DNA nanomachines .....	52
1-14 Jablonski diagram. ....	53
1-15 Schematic representation of FRET donor and acceptor spectra.....	53
2-1 Schematic representation of magnetic nanosensor for cancer cell detection and profiling.....	66
2-2 The specific recognition of ACMNPs to their target cells.....	67
2-3 The optimization of magnetic nanosensor concentration in PBS. ....	67
2-4 sgc8c-ACMNPs as a nanosensor for the detection of CEM cells in PBS.....	68
2-5 The dynamic detection range of Ramos cells using magnetic nanosensor in PBS. ....	68

2-6	sgc8c-ACMNPs as a nanosensor for the detection of CEM cells in Fetal Bovine Serum (FBS) .....	69
2-7	The detection of target CEM cells in plasma and whole blood .....	69
2-8	The detection of target cells in complex biological media mimics detection in real clinical samples .....	70
2-9	The detection of mixed cell samples for the development of rare tumor cells detection.....	70
2-10	Profiling of cancer cells. ....	71
3-1	Schematic representation of the magnetic nanosensor for Lys detection based on MRSw.....	82
3-2	Effect of incubating MNP-Lys aptamer with MNP-Linker at high concentration overnight .....	82
3-3	A gradual change of $\Delta T_2$ upon the addition of Lys .....	83
3-4	Selectivity of the Lys nanosensor.....	83
3-5	Specificity of the Lys nanosensor.....	84
3-6	Changes in T2 relaxation time with increasing concentrations of Lys. ....	84
3-7	The detection of Lys-spiked human serum using relaxometry measurements....	85
3-8	The detection of Lys-spiked human serum using T <sub>2</sub> -weighted MR images.....	85
3-9	Determination of Lys in cell lysates. ....	86
4-1	Concept of magnetically driven DNA nanomotor.....	99
4-2	Signal enhancement of DNA hairpins in solution after the addition of DNase I. 100	
4-3	Signal enhancement of DNA hairpins on the glass surface of micro-channel after DNase I addition .....	101
4-4	Cycles of closed-open state from DNA hairpins with 1.0 $\mu\text{m}$ magnetic beads. .	101
4-5	Cycles of closed-open state from DNA hairpins with 2.8 $\mu\text{m}$ magnetic beads. .	102
4-6	Cycles of closed-open state from DNA hairpins with 0.2 $\mu\text{m}$ magnetic beads. .	102
4-7	Magnetic beads effect on the DNA nanomotor.....	103

5-1 Schematic representation of DNAzyme-based magnetic nanosensor for Lys detection.....110

ABSTRACT OF DISSERTATION PRESENTED TO THE GRADUATE SCHOOL  
OF THE UNIVERSITY OF FLORIDA IN PARTIAL FULFILLMENT OF THE  
REQUIREMENTS FOR THE DEGREE OF DOCTOR OF PHILOSOPHY

DNA-CONJUGATED MAGNETIC NANOPARTICLES FOR BIO-ANALYTICAL AND  
BIOMEDICAL APPLICATIONS

By

Suwussa Bamrungsap

August 2011

Chair: Weihong Tan

Major: Chemistry

Magnetic nanoparticles (MNPs) can be synthesized to have various sizes, shapes, and compositions, providing distinctive magnetic, electronic and optical properties compared to their bulk counterparts. With the dimension similar to biomolecules, MNPs can be engineered to have specific properties and can be used to pursue an in-depth understanding of biochemical processes. Due to the strong and specific base-pairing of nucleic acids, as well as their ability to form self-assembled structural motifs, DNA conjugated MNPs can serve versatile functions including the investigation of biological activities and the construction of molecular machines.

First, a magnetic nanosensor prepared by aptamer conjugated MNPs (ACMNPs), was developed based on magnetic relaxation switches (MRSw) mechanism. The detection can be achieved by switching between dispersed and aggregated of MNPs upon binding with target cells resulting in a change in proton spin-spin relaxation times ( $\Delta T_2$ ). Specificity and sensitivity of nanosensors were capitalized by the ability of aptamers to specifically bind their targets and the large surface area of MNPs to accommodate multiple binding events. The detection as few as 10 target cells in buffer

and 100 cells were obtained in biological samples. Furthermore, by using an array of ACMNPs, various cell types can be differentiated through recognition patterns, thus creating a cellular molecular profile and allowing clinicians to accurately identify cancer cells at the molecular and single cell level.

Additionally, a nanosensor based on MRSw was also demonstrated for protein detection using Lysozyme (Lys) as a model protein. The nanosensor system consisted of MNPs aggregates prepared by the hybridization of MNPs conjugated with either aptamers or linker DNA that could hybridize to the extended part of Lys aptamers, leading to the cluster formation. In the presence of Lys, the aptamers bind with their targets, resulting in the disassembly of the clusters, and providing a change in  $T_2$  relaxation time. The high selectivity and sensitivity in nanomolar range of the detection was achieved in both buffer and human serum. The analysis of Lys in cancer cell lysates was also performed to validate the detection in real clinical samples.

Another area of investigation was the development of a magnetically driven DNA nanomotor. In particular, DNA hairpins were conjugated to magnetic particles and the entire conjugation was immobilized to a solid support. The DNA hairpin can be interpreted as a nanomotor because it switched between “closed” and “open” states. The applied magnetic field triggered the change of molecular conformation or drove the movement of molecular probes between closed and open states, which can be observed by the change of fluorescence. By repetitive shrinking and extending movements, DNA hairpins were considered as a nanometer-scale motor.

In summary, this research focuses mainly on the development of DNA-conjugated MNPs for the analysis of biological targets, and the construction of nanomachine.

Successful outcomes from these investigations will lead to the improvement in bioanalytical science, biomedical applications, and bionanomaterial research.

## CHAPTER 1 INTRODUCTION

### **Impact of Nanoparticles for Bio-analytical Applications**

Over the past few decades, nanoparticles have received considerable attention in the translation of nanotechnology into advanced biomedical science and other biotechnological fields. Compared to their bulk counterparts, nanoparticles provide drastically different properties, including (1) the small size in the sub-100 nanometer range resulting in high surface-to-volume ratios, (2) the size- and shape-dependent properties, such as the distinctive light scattering of gold nanoparticle and discrete luminescent behavior of quantum dots, and (3) the enhancement of physical and chemical properties of some materials in the nanoregime.<sup>1,2</sup> Additionally, with the similar dimension to biomolecules including oligonucleotides, peptides, proteins, and cells, nanoparticles can be engineered to construct versatile nano-bio hybrid materials for the development of bioanalysis tools and the investigation of biological processes.<sup>3,4</sup>

The demand for rapid and accurate disease screening has driven the development of novel bioassays having high sensitivity and selectivity with simple detection and sample preparation. The selectivity of the bioanalysis is achieved by molecular recognition properties such as receptor-ligand association, antibody-antigen binding, and oligonucleotide hybridization. In addition, the sensitivity is directly related to the transduction of the target-probe into the reporting signal. Consequently, the design of hybrid materials that link molecular probes serving as recognition units and nanoparticles which can generate measurable signals is very desirable. Generally, the most common reporting signals are based on optical techniques, including fluorescence, colorimetry, and Raman spectroscopy.<sup>5-7</sup> However, complex biological

systems generate high background interference by scattering, absorption and autofluorescence, which lower the signal/noise ratio and limit the sensitivity of detection. Therefore, sample purification and multiple preparation steps are needed, requiring complex instrumentation and time investment. Alternative techniques which are light independent are of great interest to overcome these drawbacks.

In recent years, considerable effort has been devoted to the design and construction of molecular machines. One of the most attractive materials chosen for construction of nanoscale machines is DNA, due to the specific base-pair formation, sequence programmability, and feasible synthesis.<sup>8,9</sup> DNA can be assembled to 2D or 3D structure and utilized as dynamic molecules that duplicate mechanical devices such as switches, walkers, and motors.<sup>10-12</sup> In particular, DNA nanomotors can be achieved by conformational changes in DNA induced by the energy input from sources such as DNA fuel strands and ATP molecules.<sup>13,14</sup> However, the addition of fuels results in the generation of waste products, and the accumulation of waste strands after several cycles of operation results in decreases motor efficiency. Therefore, alternative energy source such as electromagnetic fields are desired to eliminate the accumulation of waste products and to produce high efficiency nanomotors.

The ultimate goal of this dissertation is the development of DNA conjugated magnetic nanoparticles for molecular detection and the construction of DNA nanomachines. The following section will discuss the synthesis, characterization and conjugation of magnetic nanoparticles. A brief discussion of nucleic acid probes as selective recognition elements, including aptamers, and the systematic evolution of ligands by exponential enrichment (SELEX), as well as DNA nanomachines will follow.

Then, the principle of magnetic relaxation switches (MRSw), fluorescence spectroscopy, and fluorescence resonance energy transfer (FRET) will be reviewed. Finally, the overall focus of this dissertation will be outlined.

### **Magnetic Iron Oxide Nanoparticle Fundamentals**

In bulk materials, magnetic properties can be determined by multiple parameters such as susceptibility, coercivity, composition, crystallographic structure, and the presence of vacancies and defects. However, when the size of a magnetic material is reduced into the nanoregime, size is the dominant parameter, because the properties of MNPs are strongly dependent on their dimensions.<sup>15,16</sup> Bulk magnetic materials possess multiple magnetic domains due to the different alignment of electron spins generating varying magnetic moments. With decreasing size of MNPs below their critical size, they exist as a single domain with spins aligned unidirectionally (Figure 1-1). However, when the size is further reduced, the thermal energy effect is significant in the nanoregime and it is sufficient to tilt the surface spins of the MNPs. Such surface spin-canting leads to a net magnetization of zero, and this behavior is called superparamagnetism.<sup>17,18</sup> Such particles can be magnetized in the presence of a magnetic field and then return to the original state in the absence of the external field.

Superparamagnetic materials, especially iron oxide nanoparticles ( $\text{Fe}_3\text{O}_4$  or  $\text{Fe}_2\text{O}_3$ ), are extremely attractive in biotechnological research, and their crucial characteristics avoid undesired particles aggregation. Thus, iron oxide particles have been used for numerous purposes, including biosensing, bioseparation, magnetic resonance imaging (MRI), drug delivery, hyperthermia therapy, and tissue engineering.<sup>4,19</sup> Typically, a size smaller than 100 nm and a narrow size distribution are

required for biomedical applications. Therefore, the control of synthesis, surface modification, and biomolecular conjugation are extremely important.

### **Synthesis of Iron Oxide Nanoparticles**

Iron oxide nanoparticles can be synthesized by various techniques: microemulsions, sol-gel reactions, electrochemical methods, flow injection syntheses, and electrospray syntheses.<sup>18,20</sup> However, the most common methods of iron oxide nanoparticle synthesis are chemical coprecipitation and thermal decomposition reactions. The coprecipitation is the simplest way to prepare iron oxide nanoparticles of magnetite, Fe<sub>3</sub>O<sub>4</sub>, or maghemite, Fe<sub>2</sub>O<sub>3</sub>. Typically, they are prepared by aging stoichiometric mixture of ferrous and ferric salts in aqueous medium according to the reaction



In general, complete precipitation of Fe<sub>3</sub>O<sub>4</sub> takes place at pHs between 8 and 14 with a stoichiometric ration of 2:1(Fe<sup>3+</sup>/Fe<sup>2+</sup>) in a non-oxidizing environment.<sup>21</sup> Fe<sub>3</sub>O<sub>4</sub> is not very stable and can be transformed to Fe<sub>2</sub>O<sub>3</sub> in the presence of oxygen as follows



The advantages of the coprecipitation method are ease of synthesis and the capability for large-scale production. However, the drawback of this technique is the non-uniformity of the particles. During the process, two steps are involved: the nucleation occurs when the concentration of reactive components exceeds saturation and the subsequent slow growth of nuclei. In order to achieve monodisperse particles, nucleation should be avoided during the growth phase of nanocrystals. Generally, the sizes and shapes of iron oxide nanoparticles can be tuned by adjusting the Fe<sup>2+</sup>/Fe<sup>3+</sup>

ratio, pH, ionic strength, temperature, and nature of the counterions. The size of iron oxide particles increases with the ratio of  $\text{Fe}^{2+}/\text{Fe}^{3+}$ .<sup>22</sup> Higher pHs and ionic strengths lead to the smaller size of particles, because the chemical composition and electrostatic surface charge are determined by those parameters. It has also been found that the nucleation decreases when the temperature is increased.<sup>23</sup> Iron oxide nanoparticles prepared by the coprecipitation method can be dispersed in either aqueous media or a nonpolar solvent suitable for further surface modification.

Superparamagnetic iron oxide nanoparticles can also be prepared by thermal decomposition of iron organic precursors, such as iron pentacarbonyl,  $\text{Fe}(\text{CO})_5$ , iron acetylacetonate,  $\text{Fe}(\text{acac})_3$ , or iron(III) chloride,  $\text{FeCl}_3$ , using organic solvents and surfactants. MNPs with a high level of size control and monodispersity can be obtained by the control of reaction conditions, including solvent, temperature, and reaction time. The nucleation steps may be faster than the growth steps at high temperature, resulting in a decrease of particle size. However, a long reaction time facilitates the growth steps with other conditions held constant. For example, iron oleate can be formed by decomposition of  $\text{Fe}(\text{CO})_5$  in the presence of oleic acid and octyl ether at 100°C in an argon atmosphere. Then  $(\text{CH}_3)_3\text{NO}$  is added and the solution is refluxed at 300°C for the oxidation step. These processes allow the production of highly crystalline and monodisperse iron oxide nanoparticles with sizes from 4 to 16 nm.<sup>24</sup> High uniformity of iron oxide crystals with sizes ranging from 4 to 20 nm can also be achieved by a high-temperature reaction of  $\text{Fe}(\text{acac})_3$  with 1,2-hexadecanediol in the presence of oleic acid and oleylamine. The hydrophobic particles are highly dispersed in organic solvents and can be further transformed into a hydrophilic phase by adding bipolar ligands.

## Iron Oxide Nanoparticle Surface Modification and Bioconjugation

It is essential to modify iron oxide particle surfaces in order to achieve stable magnetic colloids that do not aggregate in magnetic fields and biological media. Stability of magnetic colloid results from the equilibrium between attractive and repulsive forces in suspension. In theory, interparticle interactions can be divided into four types: 1) van der Waals forces which are short-range isotropic attractions, 2) electrostatic forces controlled by salt concentration, 3) dipolar forces generated between two particles, and 4) steric repulsion from coated particles.<sup>25</sup> For iron oxide nanoparticles, the surface contains iron atoms which act as Lewis acids and can interact with molecules that donate a lone-pair of electron. In aqueous solution, iron ions coordinate with water molecules which can be hydrolyzed resulting in hydroxyl groups on the particle surface. The hydroxyl groups allow iron oxide particles to be modified using several types of materials, including polymeric ligands, inorganic materials, and micellar coatings.

Various polymers have been utilized to coat iron oxide nanoparticles, either *in situ* or post-synthesis coatings. In the first approach, nanoparticles are coated during the synthesis, and the most common polymer used is dextran which is a polysaccharide. The possible mechanism of dextran adsorption on iron oxide might be the hydrogen bonding between hydroxyl groups on dextran and the particle surface.<sup>26</sup> The advantages of using dextran as a stabilizer are its non-toxicity and biocompatibility. For the post-synthesis coatings, ligands normally consist of two parts: the region that binds to particle surface and the hydrophilic region that is exposed to aqueous media. Polyethylene glycol (PEG) is commonly utilized for the post-synthesis coating due to its hydrophilic and biocompatible properties. PEG can be modified with thiol, dopamine, phosphate, or siloxane groups in order to provide iron oxide particles with high stability

and solubility as well as to block non-specific adsorption of unwanted molecules on the particle surface.<sup>27</sup>

Coating with silica is one of the most common strategies for modifying the surfaces of iron oxide nanoparticles. This coating not only provides high stability to particles but also facilitates further surface functionalization. Silica coated MNPs can be prepared by two general routes: the Stöber and reverse microemulsion methods. The Stöber method is based on the formation of particles by hydrolysis of a silica precursor (e.g., tetraethylorthosilicate, TEOS) in ethanol media containing water and ammonia as the basic catalyst (Figure 1-2). MNPs have been incorporated into the silica matrix, and the coating process can be completed within a few hours. It was observed that lower concentrations of iron oxide nanoparticles induce larger colloids due to the presence of fewer number of particle seeds.<sup>28,29</sup> However, this route always yields large and non-uniform particles.

The alternative method to prepare silica coated MNP is to use a microemulsion or water-in-oil (W/O) microemulsion system, which has three main components: water, oil, and surfactant (Figure 1-3).<sup>30,31</sup> Water nanodroplets formed in the bulk oil phase act as a confined medium for the formation of discrete nanoparticles. Iron oxide particles are entrapped in the water pool and the size of particles can be tuned by controlling the water-to-surfactant molar ratio ( $W_o$ ). The microemulsion method takes 24-48 hours to complete and yields monodispersed and highly uniform particles.

Another role of surface modification is to incorporate recognition elements, such as, antibodies, oligonucleotides, or peptides that specifically bind with target molecules for biological applications. Typically, biomolecules can be functionalized on particle

surfaces either by physical adsorption or covalent attachment. Physical adsorption involves electrostatic, hydrophobic, hydrophilic, or van de Waals forces to associate the desired molecules onto the particle surface. In general, covalent attachment of biorecognition elements is preferred, not only to avoid desorption from the surface, but also to control the number and orientation of the immobilized biorecognition probes.<sup>32</sup> However, covalent attachment requires chemically reactive functional groups on the particle surface, including amine, carboxyl, or thiol. These groups can be attached to the surface either during or after post-coating for particle stabilization.

After nanoparticles are functionalized, they can act as scaffolds for biological moieties as demonstrated in the scheme (Figure 1-4). For example, carboxyl-modified particles are suitable for covalent coupling of proteins and other amine-containing biomolecules via carbodiimide chemistry. Disulfide-modified nanoparticles can be immobilized onto thiol-functionalized particles by disulfide-coupling chemistry. Amine-modified nanoparticles can be coupled with a wide variety of haptens and drugs via succinimidyl esters and iso(thio)cyanates.<sup>33</sup> After the bioconjugation step, the nanoparticles can be separated from unbound biomolecules by centrifugation, dialysis, filtration or other laboratory techniques.

### **Size, Shape, Magnetic properties and Surface Characterization**

Since many properties of nanoscale materials depend on their physical characteristics, it is necessary to define the size, shape, and polydispersity of nanoparticles. Transmission electron microscopy (TEM), scanning electron microscopy (SEM), and atomic force microscopy (AFM) are the most common techniques that are utilized for size determination.<sup>34</sup> The EM techniques can provide details about size, shape, and size distribution. However, sample preparation can induce aggregation and

limited information is achieved for the dispersive nature of particles in solution. In addition, dynamic light scattering (DLS) is a common technique used to obtain information about both sizes and dispersion of particles in suspension. The hydrodynamic radius corresponding to the sphere and the polydispersity of the colloid is also obtained.<sup>35</sup> X-ray diffraction (XRD) can also be used to indicate crystalline structures of nanoparticles. The proportion of iron oxide particles can be quantified by the peak intensities of the diffraction pattern compared to the reference peak intensities. Furthermore, the crystal size can also be calculated from the broadening of the XRD pattern.<sup>36,37</sup>

Another important parameter used for particle characterization is the surface charge or zeta potential ( $\zeta$ ) which is affected by the environment including, pH and ionic strength. The magnitude of the zeta potential indicates the repulsive force between particles and can be used to predict the stability of a colloid. Particles in suspension having high negative or positive zeta potentials tend to repel each other, resulting in a low tendency to aggregate. Additionally, zeta potential measurement can be used to verify surface modification or bioconjugation of the nanoparticle surface. For example, during the synthesis and modification processes, nanoparticle surface charge will be changed according to the charge of the coordinated materials, such as polymers, DNA, or proteins.

### **Magnetic Nanoparticles for Magnetic Resonance (MR) Based Assays**

The ultimate goal of the development of biosensing platforms is to have far-reaching implication in point-of-care clinical diagnostics, pharmaceutical drug development, and proteome research. In order to achieve robust, versatile, and high throughput sensing platforms, the assay methodologies need to meet several

requirements: 1) high sensitivity and specificity, 2) minimized sample preparation, 3) capability to analyze different types of target molecules with the same format and instrument; and 4) feasibility for both single tube and high-throughput screening formats.<sup>38</sup>

Magnetic nanoparticle-based biosensors have gained considerable attention due to their unique advantages over other techniques. For example, magnetic nanoparticles can be easily and cheaply synthesized and modified. They are physically and chemically stable, as well as biocompatible. Additionally, magnetic nanoparticles have strong magnetic properties, which are not found in biological systems. With no magnetic background in biological samples, magnetic nanoparticle-based sensors can perform highly sensitive measurements in turbid or obscured sample without any further processing. In contrast, optical techniques are always affected by autofluorescence, scattering, and absorption within samples.

To date, a number of biosensors based on magnetic measurement have been developed. Several techniques, including superconducting quantum interference devices (SQUIDs),<sup>39</sup> magnetoresistive sensors,<sup>40,41</sup> and Hall sensors<sup>42</sup> directly detect magnetic particles. Another technique that has received considerable attention is nuclear magnetic resonance (NMR) spectroscopy which can be translated into an imaging technique called magnetic resonance imaging (MRI). Due to their noninvasive character, both conventional NMR and MRI have been widely used in medical applications for sample evaluation and characterization. In MRI, magnetic nanoparticles are used as contrast agents, which provide signal enhancement as a result of the interactions with neighboring water protons. Recently, another magnetic technique has

been developed to produce a new approach for *in vitro* diagnostics. This new assay, termed “magnetic relaxation switches” (MRSw), has led to a new platform for sensors with high sensitivity, selectivity, and feasibility in immuno- and molecular-diagnostics for point-of-care detection.

### **Basic Concept of Magnetic Resonance Imaging (MRI)**

When the nuclei of protons are exposed to a strong magnetic field ( $B_0$ ), their spins align either parallel or antiparallel to the external magnetic field with a small excess aligned parallel. The aligned spins precess with a net magnetic moment of  $M$  and a Larmor frequency of  $\omega_0 = \gamma B_0$  ( $\gamma$  is a gyromagnetic ratio of proton =  $2.67 \times 10^8 \text{ rad}\cdot\text{s}^{-1}\cdot\text{T}^{-1}$ ) as shown in Figure 1-5A. When a resonance radio frequency (RF) pulse is introduced perpendicular to  $B_0$ , the protons absorb energy and are excited to the antiparallel state which has high energy. Net magnetization  $M$  as a vector has the components of  $M_z$  and  $M_{xy}$ (Figure 1-5B). By removal of the RF, the excited spins gradually relax to their initial or lower-energy state. There are two different relaxation pathways: longitudinal or  $T_1$  relaxation involves the recovery of magnetization ( $M_z$ ) to the initial state by transferring energy from the excited state to its surrounding (lattice), and transverse or  $T_2$  relaxation involves the disappearances of magnetization in the perpendicular plane ( $M_{xy}$ ) from the loss of phase coherence of the nuclei spins in the  $xy$  plane due to spin-spin interactions (Figure 1-5C and D). The relaxation processes are expressed as follows:

$$M_z = M(1 - e^{-t/T_1}) \quad (\text{longitudinal}) \quad (1-3)$$

$$M_{xy} = M \sin(\omega_0 t + \phi) e^{-t/T_2} \quad (\text{transverse}) \quad (1-4)$$

where  $M$  is the net magnetization,  $\omega_0$  is the Larmor frequency of protons, and  $T_1$  and  $T_2$  are the longitudinal and transverse relaxation times, respectively.

The phase coherence in the xy-plane disappears due to the differences of magnetic fields experienced by protons. The magnetic field differences are generated by inhomogeneities in the applied field due to the system imperfections, which can be reduced by shimming coils, and the usage of spin echo sequence to reverse this effect. Furthermore, local magnetic field gradients can be induced by the differences in magnetic susceptibility between different tissues. Biological organs and tissues have a variety of aqueous environments in both density and homogeneity, and these generate contrasts and reveal anatomical information. MRI records these relaxation processes and reconstructs 3-D gray scale images. Areas with shorter  $T_1$  relaxation are imaged as brighter contrast in  $T_1$ -weighted MRI, while areas with shorter  $T_2$  relaxation are reported as darker contrast in  $T_2$ -weighted MRI. However, in some cases, the contrast between tissues is unable to provide precise imaging information, due to the small differences with tissues' environments. Therefore, contrast agents are introduced to enhance local magnetic field gradients resulting in the high-contrast MRI.

### **Magnetic nanoparticles (MNPs) and $T_2$ relaxation**

MNPs not only play a role as contrast agents to enhance contrast differences of biological targets from tissues, but they also act as carriers for ligands to provide specific targeting. In an external field  $B_0$ , MNPs are magnetized with magnetic moment  $\mu$ , establishing local dipolar fields and perturbing their surroundings. Such induced fields generate local magnetic inhomogeneities and accelerate the dephasing rate of the Larmor precession of surrounding water molecules. Consequently, the  $T_2$  relaxation time is reduced (Figure 1-6). According to the outer sphere theory, the relaxivity  $R_2$  ( $1/T_2$ ) of MNPs containing water solution is expressed as follow:<sup>43</sup>

$$R_2 = \frac{1}{T_2} = \left(\frac{32\pi}{405}\right)\gamma^2\mu^2\left(\frac{N_A[M]}{1000rD}\right)[6.5j_2(\omega_s) + 1.5j_1(\omega_i) + 2j_1(0)] \quad (1-5)$$

where M is the molarity of MNPs, r is the MNP radius, D is the diffusion coefficient of water,  $j_n(\omega)$  is the spectral density function,  $\mu$  is transverse component of magnetic moment of the MNP,  $\gamma_i$  is the gyromagnetic ratio of protons,  $N_A$  is Avogadro's number, and  $\omega_s$  and  $\omega_i$  are the Larmor angular precession frequencies of the MNPs and the water proton magnetic moments, respectively.

The spin-spin or  $T_2$  relaxation time is inversely proportional to the square of the magnetic moment ( $\mu$ ) of MNPs as demonstrated in equation 1-5. As mentioned previously, these values can be modulated by controlling characteristics of the MNPs, such as size, shape, composition, and crystallinity. Smaller particles with higher surface-to-volume ratios possess weaker magnetic moment due to the significant canting effect on the surface. Such size effects have been demonstrated by Cheon et. al. for  $Fe_3O_4$  iron oxide nanoparticles.<sup>16</sup> It was reported that the mass magnetization value ( $M_s$ ) increase from 68 to 191 emu/g(Fe) as the particle size increases from 6 to 12 nm (Figure 1-7A).

Compositional effects also have been demonstrated by doping with different transition metals including Mn, Co, and Ni (Figure 1-7B). For example, the replacement of octahedral site of  $Fe^{2+}$  in 12 nm iron oxide particles with  $Mn^{2+}$ ,  $Co^{2+}$ , or  $Ni^{2+}$  results in a change of  $M_s$  to 110, 99, to 85 emu/g, respectively. Higher magnetization of MNPs results in stronger contrast effects and larger  $R_2$  relaxivity. As shown in Figure 1-7B, doped iron oxide particles possess a variety of  $R_2$  ranging from 152 to 172, 218, and 358  $mM^{-1}s^{-1}$  for Ni, Co, Fe, and Mn, respectively.

When MNPs are in close proximity and agglomerate, their magnetic moments are coupled and generate stronger local magnetic fields (Figure 1-8). The magnetic coupling effect directly influences the MR contrast by accelerating the proton dephasing rate. The increase of  $R_2$  relaxivity is expressed as:<sup>43</sup>

$$R_2 = \frac{1}{T_2} = \left( \frac{64\pi}{135} \right) \left( \frac{L(x)\mu N_g}{4\pi} \right)^2 \frac{C_A N_A}{R_A D} \quad (1-6)$$

where  $\mu$  is magnetic moment of MNPs,  $N_g$  is number of MNPs in agglomerates,  $L(x)$  is Langevin function,  $N_A$  is Avogadro's number,  $C_A$  is the concentration of agglomerates,  $R_A$  is radius of an agglomerate, and  $D$  is the water diffusion coefficient.

According to equation 1-6,  $R_2$  is proportional to  $\mu$  and  $N_g$ . Consequently, the magnetic coupling effect significantly improves the sensitivity of magnetic resonance sensing, where the MR signal contrast changes depending on the relative concentration of the assembled states of MNPs. Based on this strategy, MNPs have been extensively used in cancer research. It is well known that nanoparticles can be accumulated spontaneously in tumor sites by the enhanced permeability and retention (EPR) effect, which enhances the accumulation of nanoparticles in tumor tissues that have abnormal blood vessels.<sup>44</sup> As a consequence, MNPs have been successfully used to image tumors without any targeting probes, called "passive targeting".<sup>45</sup> However, in order to improve imaging efficiency, surfaces of MNPs are conjugated to active targeting probes such as antibodies, proteins, and aptamers. For example, iron oxide nanoparticles are conjugated with specific antibodies to image tumors by the interactions with surface protein receptors that are overexpressed in gliomas,<sup>46</sup> breast,<sup>47</sup> and colon cancers. Moreover, multifunctional nanoplatforms fabricated by combining various materials to perform different functions, allow multimodal imaging, including simultaneous diagnosis

and therapy. For example, Fe<sub>3</sub>O<sub>4</sub>-Au dumbbell particles were applied to cancer-targeted MR and reflection imaging.<sup>48</sup>

### **Magnetic Relaxation Switches (MRSw)**

Recently, Weissleder and coworkers demonstrated MR based assays called Magnetic Relaxation Switches (MRSw), which allow detection by the change of T<sub>2</sub> induced by magnetic particles. The principle of MRSw assays is demonstrated in Figure 1-9. As illustrated, magnetic particles switch between the dispersed and aggregated states when the target molecule bind with ligands conjugated on magnetic particles' surfaces. The presence of multiple ligands on particles' surfaces induces multivalent affinity, resulting in multiple interactions between the conjugates and their corresponding targets. The change of spin-spin or T<sub>2</sub> relaxation time is associated with the degree of aggregation similar to conventional MRI. Magnetic particles used for MRSw assays are either MNPs or micrometer-sized magnetic particles (MMPs). Since the dispersed and aggregated states of magnetic particles can be reversed by external stimuli such as pH, salt concentration, and concentration of competing analytes, these assays are referred to as relaxation switches.

The MRSw provides various unique properties: (1) Because detection is not dependent on light (no fluorescence, absorbance, turbidity, or chemiluminescence), analytes interfering with light do not affect the assay, and the experiment can be carried out in turbid and heterogeneous samples. (2) The washing step is not needed to remove unbound analytes, thereby minimizing the analysis time. (3) The assay does not require surface immobilization of biomolecules on a glass slide, thus minimizing the complexity of the preparation steps. (4) The assay is flexible and can detect various

kinds of biomolecular interactions, including protein-DNA interactions, protein-small molecule interactions, and protein-protein interactions.

### **Mechanism of magnetic relaxation switches (MRSw)**

In MRSw assays, both MNPs and MMPs can be used to provide different  $T_2$  relaxation times for their respective dispersed and aggregated states. However, for Type I, MNP-based systems,  $T_2$  decreases with the aggregation, while for Type II, MMP-based systems,  $T_2$  increases with aggregation.<sup>49</sup> The basis of this can be described using the theory termed outer sphere relaxation theory.

In this theory, two main parameters,  $D_w$  and  $t_D$ , are considered.  $D_w$  is the difference in angular frequencies between the local field experienced by protons at the surface of particles and in the bulk, and  $t_D$  is the translational diffusion time of water around the sphere of an aggregate. These parameters are given by:

$$D_w = m_0 M \gamma / 3 \quad (1-7)$$

$$t_D = R_a^2 / D \quad (1-8)$$

where  $m_0$  is the vacuum magnetic permeability,  $M$  is the particle magnetization,  $\gamma$  is the proton gyromagnetic ratio,  $R_a$  is the sphere radius, and  $D$  is water diffusion coefficient.

The outer sphere theory is applied when  $D_w t_D < 1$ , referred to as the motional average condition.<sup>50</sup> When MNPs aggregate (Type I), smaller numbers of larger magnetic field inhomogeneities are produced compare to the dispersed state. The larger homogeneities are more effective in the dephasing of water protons. In this condition, the relaxation rate  $R_2$  ( $1/T_2$ ) increases as the sphere's size is increased. In contrast, when MMPs aggregate (Type II), there are fewer clusters compared to the Type I case and spaces between them are large. Consequently, many water protons fail to diffuse in and out this inhomogeneities field during the measurement time. In this

condition, the motional average is not fulfilled and the relaxation rate decreases with the formation of aggregates. Here  $D_w t_D > 1$ , referred to diffusion limited case.

MRSw based biosensors achieve the selectivity and specificity for desired molecular targets by attachment of binding moieties such as antibodies or aptamers to magnetic particles. Therefore, the basis of the transition between dispersed and aggregated states is the affinity of ligands on the particles' surfaces for specific analytes. The density of ligands can be optimized to achieve fast reaction rates and high detection sensitivities.<sup>51</sup> As in conventional MRI, other parameters such as particle types, sizes, and concentration also influence the change of  $T_2$ .

### **Instrumentation for MRSw**

MRSw based sensors can benefit a variety of applications including home and clinical diagnostics, proteome research, bio-warfare, and industrial analysis. Such applications require simple, automated, robust, and high throughput instrumentation. A key component for facilitating successful applications is tailoring the processing and detection platforms. Currently, most MRSw assays in laboratory and industrial scenarios depend on bench top relaxometers. High throughput MRSw assays also have been demonstrated using 384-well plates and an MR scanner for multiplex detections.<sup>52</sup> However, the bench top relaxometer and MR scanner are still impractical for point-of-care detection due to their high cost and bulkiness. Recently, miniaturized MR relaxometers have been fabricated by Lee and coworkers.<sup>53,54</sup> The system consists of a small palm-sized permanent magnet and on-board NMR electronics and planar microcoils with integrated microfluidic channels. Multiplexed detection of biomarkers was demonstrated for high throughput MRSw assays.

MRSw based biosensors offer unique advantages over other techniques, such as a simple assay format, feasibility in biological detection without a separation or amplification step, high throughput capacity, and broad applications to detect and profile different types of targets. Taking these advantages, this technology has potential applications in biomedicines, cancer biology and proteomic research. Through the development of the chip-based MR devices, clinic and other point of care diagnostics are possible.

### **Nucleic Acid Probes**

Nucleic acids play important roles in transferring genetic information through generations and act as key elements for proliferation. The main components of nucleic acids consist of several nucleotides sharing the same backbone structure but different bases (Figure 1-10). Various sequences generated from different assemblies of bases contribute to the specific interaction with complementary oligonucleotides forming a double helix structure. Furthermore, structural folding of single-stranded oligonucleotides provides molecular recognition abilities for a variety of biological targets. Particularly, Watson-Crick type hydrogen-bonds, electrostatic forces,  $\pi$ -stacking bonds, and hydrophobic interactions enable the design of molecular probes for signaling biomolecular interactions. Compared with traditional recognition, such as host-guest chemistry, or protein interactions, molecular recognition using nucleic acids is flexible, and can be easily modified. Consequently, various types of biosensors and medical diagnostic tools have been developed based upon the special recognition properties of nucleic acids.<sup>55-58</sup> Especially, when combined with the extraordinary properties of nanoparticles, these hybrid materials demonstrate broad application as powerful molecular recognition tools.<sup>3,59,60</sup>

In addition, nucleic acids, especially DNA, are ideal building blocks for the design and assembly of nanostructures, due to the strong and highly specific base-pairing of A-T and G-C interactions (Figure 1-11). Besides duplex formation, self-assembled structural motifs of DNA are also available, such as G-quadruplexes, i-motif, or hairpin structures.<sup>61,62</sup> The diversity of structural patterns allows use of DNA as templates for the bottom-up construction of 2D and 3D-nanostructures.<sup>63,64</sup> Beyond the use of DNA for nano-assembly, DNA can be utilized as dynamic molecules that duplicate mechanical devices, e.g., switches, tweezers, and motors.<sup>65-68</sup> Because these DNA nanomachines have the benefits of precise controllability, biocompatibility, and reproducibility, they can be utilized for the development of synthetic molecular machines.

The following sections focus mainly on the use of nucleic acids as selective biorecognition elements. In particular, specific oligonucleotides termed aptamers, and the selection process called Systematic Evolution of Ligands by Exponential enrichment (SELEX) will be discussed, as well as DNA probes which can be designed, and engineered as molecular machines.

### **Selective Biorecognition Elements**

Several diseases, especially cancer, are associated with specific biomarkers. The key to develop diagnostic and therapeutic tools is an understanding of the molecular recognition of disease-specific biomarkers. Since potential biomarkers encompass different types of molecules, ranging from glycolipids to proteins, it is necessary to identify molecular probes that are able to bind selectively with these molecules. However, long periods of time and considerable efforts are required for the identification and separation of biomarkers and their corresponding probes. The two most important

classes of biorecognition elements utilized as molecular probes are antibodies and aptamers.

Antibodies are proteins produced by the immune system when triggered by foreign proteins or microorganisms defined as antigens.<sup>69</sup> Typically, antibodies consist of two basic structural units, called the heavy and light chains. However, the antigen-binding sites of each type of antibody are very unique and allow selective binding with a particular epitope on an antigen. Generally, antibodies can be generated by injecting antigen into animals and isolating the antibodies from their blood. After isolation and purification, antibodies are commonly used to identify, locate, and separate both intracellular and extracellular proteins. They are also utilized to differentiate cell types according to the expressed proteins. However, the application of antibodies as molecular recognition elements sometimes is limited due to their lack of reproducibility, sensitivity to environmental conditions, difficulty in chemical modification, and short shelf life.

Recently, a new type of selective recognition ligands termed aptamers has been introduced to identify wide variety of targets. Aptamers are single-stranded oligonucleotides that can selectively recognize target cells, proteins, peptides, small molecules, and ions.<sup>70,71</sup> The binding affinities of aptamers to their targets are comparable to those of antibodies and range from  $10^{-12}$ M to  $10^{-8}$ M. The high specificity of aptamers, which can distinguish even homologous proteins, derives from their complex three-dimensional structures. Aptamers have shown great promise in molecular recognition for diagnostic and therapeutic applications. Moreover, aptamers

have advantages over antibodies due to their reproducibility, ease of synthesis and modification, low toxicity or immunogenicity, and long shelf life.

Aptamers can be identified by an *in vitro* selection process called SELEX (Systematic Evolution of Ligands by Exponential enrichment).<sup>72,73</sup> The potential sequences are selected from a pool of random sequences of synthetic DNA or RNA through many rounds of selective binding to the targets. Typically, aptamers have been selected using purified proteins or molecules as targets. Recently, the Tan research group has developed a novel cell-based aptamer process called cell-SELEX.<sup>58,74</sup> Instead of using a single target molecule, whole cells are used as targets. Selection of aptamers that recognize target cells but do not bind to control or non-target cells provides several advantages. First, it is not necessary to know specific targets on the cell surface. As an alternative, different cell types are used in the selection process, so aptamers obtained from cell-SELEX can be applied to differentiate different types of cells, especially cancer cells. Secondly, since the cell membrane surface is very complex and contains a large number of potential targets, aptamers can be generated for different types of molecules, which may be expressed in different types and stages of diseases. Thus, the selected aptamers may be useful for the biomarker discovery or the study of disease development. Furthermore, as live cells are used during the selection process, all target molecules are in their naturally folded structures. Therefore, the generated aptamers will recognize the actual conformations of targets, an important capability for *in vivo* applications.

The cell-SELEX process starts with the selection using a large pool of library sequences ( $10^{13}$ - $10^{16}$  single stranded DNA oligomers) against target or positive cells

(Figure 1-12). Subsequently, the negative or non-target cells are used to exclude oligomers with non-specific interactions, making the selected sequences specific to the target cells. The selected sequences are washed and purified in order to retain only the ones binding tightly to the target cells, and eliminate unbound or weakly bound sequences. Subsequently, the bound sequences are recollected and amplified by the polymerase chain reaction (PCR) for the next round of selection. After several rounds of repetitive selection, a group of aptamers will be obtained and further tested for their affinity and specificity.

### **DNA Molecular Machines**

Besides the fascinating properties in selective recognition of specific targets, DNA has also gained attention in material science and nanotechnology. Based on the structural flexibility, and specific base-pair formation, DNA is programmable and designable, and thus can be used as a structural building block. Pioneered by Seeman *et.al.* in the 1980s, 2D and 3D DNA nanostructures have been assembled.<sup>8,63,75</sup> DNA has also been converted into dynamic molecules that can perform nanoscale movements. Although, proteins are the naturally selected materials for motions in living organism, the simplicity of structure, diversity of self-assembly, and automated synthesis make DNA the most promising molecule that can duplicate machine functions. DNA-based nanomachines can be delivered into several categories, depending on their motions as switches, walkers, or motors.

### **DNA switches**

A molecular switch or actuator is one of the simplest nanodevices which can switch between two conformations. One of the original DNA switches consists of double-stranded DNA with the sequence  $(CG)_n$  and can be flipped from the normal

right-handed helix (B-DNA) to the left-handed conformation (Z-DNA). This conformational change is triggered by high salt concentration and low temperature (Figure 1-13A).<sup>76,77</sup> The transition could be tracked by Förster Resonant Energy Transfer (FRET), since a reporter fluorophore was intercalated in each tile.

Instead of environmental changes, the addition of DNA strands can also induce the switching of DNA nanostructures. A pair of DNA tweezers with two rigid double-stranded arms was constructed (Figure 1-13B).<sup>10</sup> The additional single-stranded DNA can bind with the extended tails of both arms and transform the DNA tweezers from the “open” to the “closed” state. Another “anti-fuel” strand which is complementary to a “fuel” strand was added and triggered DNA migration, returning it to the initial open state.

### **DNA walkers**

One of the most sophisticated tasks of DNA-nanomachine design and construction is the control of linear motion in a defined direction. To achieve this goal, another type of molecular device, termed a DNA walker, was created. Typically, a DNA walker is temporarily bound to a nucleic acid track. By sequential addition of DNA strands, dissociation and re-association of the walker to the next single-stranded anchor occurred (Figure 1-13C).<sup>12</sup> By appropriate design of the hybridizing nucleic acid allows stepwise translocation in unidirectional movement. Labeling of the walker’s legs and footholds with a fluorophore and quencher facilitates the real time visualization of the DNA walker’s motion, and the movement can also be further confirmed using gel electrophoresis.

## DNA motors

Biological motors that use free energy from hydrolysis of adenosine tri-phosphate (ATP) to drive the movement can move with very fast speeds (up to  $60 \mu\text{m s}^{-1}$ ) and long travelling distances (up to  $1 \mu\text{m}$ ).<sup>78</sup> Inspired by biological motors such as myosin, kinesin, and dynein that move along cytoskeleton networks, DNA nanomotors have been constructed. Previously, three different energy sources for synthetic DNA nanomotors including hydrolysis of ATP and the DNA backbone as well as DNA hybridization, have been explored. Yin and co-workers demonstrated a nanomotor that passes its cargo autonomously from one anchor to the next by enzymatic ligation and hydrolysis (Figure 1-13D).<sup>13</sup> The designed sequences were recognized by restriction enzymes to provide uni-directional movement and prevent dissociation of the cargo from the track. In the mean time, DNA nanomotors driven by the catalysis of DNA hybridization as an energy source were developed (Figure 1-13E).<sup>79</sup> Generally, their operating cycles involve a conformational change triggered by the addition of fuel DNA, which is later removed by hybridization with the complementary anti-fuel strands. The duplex between fuel and anti-fuel strands are waste products generated in every cycle of operations. The entire processes are driven by the decrease in free energy on forming additional base pairs, much like ATP hydrolysis.<sup>80</sup> Furthermore, various DNA nanomotors have been developed using alternative energy sources, such as ions, protons, light, and small molecules.<sup>81-84</sup>

In addition to the construction of stable, powerful, and simple DNA nanodevices, the most important requirement is to achieve machines that can do practical work. Currently, DNA has been proven to be a potential material for the realization of synthetic molecular machines. DNA devices have been designed to perform functions such as,

sensing molecules, directing chemical reactions, driving objects, and controlling released molecules. A future accomplishment could be the combination of a DNA computer, DNA nano-mechanics, and DNA nano-electronics, etc. The further development of this field may have great impact in nanobiotechnology and biomedical applications.

### **Fluorescence Techniques for Signal Transduction**

During the few past decades, fluorescence has played significant roles in biological sciences. Fluorescence spectroscopy is considered to be a primary research tool in biotechnology, biomedical diagnostics, and nanotechnology. Because of its high sensitivity, ease of sample handling, and multiplexing capability, fluorescence is widely used for signal transduction, as well as cellular and molecular imaging. Fluorescence results from a multi-stage process involving fluorescent substances called fluorophores.

#### **Jablonski Diagram**

The processes involved in fluorescence are illustrated by the Jablonski diagram<sup>85</sup> (Figure 1-14), which is named after Professor Alexander Jablonski. In particular, the singlet ground, first, and second electronic states are depicted by S<sub>0</sub>, S<sub>1</sub>, S<sub>2</sub>, respectively, while T<sub>1</sub> stands for the triplet state. Each of these electronic energy levels consists of discrete vibrational energy levels with vibrational quantum numbers 0, 1, 2, etc. A fluorophore is typically excited by photons to a higher vibrational level of either S<sub>1</sub> or S<sub>2</sub>, depending on the magnitude of the absorbed energy. The excitation process happens in a very short time (ca 10<sup>-15</sup>s). After light absorption, some molecules in excited state, S<sub>1</sub> for example, rapidly relax to the lowest vibrational level of S<sub>1</sub>. This process is called internal conversion which generally occurs within 10<sup>-12</sup>s. In this process, energy is transferred as heat by collisions with surrounding molecules. The

excited molecules can then relax from the lowest energy vibrational state of S1 to ground state S0 with emission of photons referred to fluorescence. The average time for a molecule to stay in an excited state is referred to as the fluorescence lifetime, typically about  $10^{-8}$ s. Due to the closely spaced vibrational energy levels of the ground state coupled with thermal motion, a wide range of photon energies is produced during emission. Consequently, fluorescence is normally observed as emission over a band of wavelengths instead of a sharp line. Most fluorophores can repeat excitation and emission up to hundreds or thousands times before the excited state molecules are destroyed. Molecules in the S1 state can also undergo a spin conversion to the first triplet state, T1, by a process called intersystem crossing. The relaxation from T1 to S0 with emission of photons is referred to as phosphorescence. Generally, the transition from the triplet excited state to the singlet ground state is forbidden. Therefore, rate constants for phosphorescence are several orders of magnitude smaller than those of fluorescence. Additionally, a small fraction of energy is always lost during vibrational relaxation, resulting in an energy difference between the absorbed and emitted energy. Thus, the emission spectrum of a fluorophore generally appears at longer wavelength or lower energy than absorption. This phenomenon, called the Stoke's shift, allows the spectral separation of the excitation and emission of photons for sensitive studies.

### **Fluorescence Quenching**

Fluorescence quenching refers to any process that decreases the fluorescence intensity of a sample, and can be caused by a variety of molecular interactions. Basically, there are two main types of quenching: collision or dynamic quenching and static quenching.<sup>85</sup> Both dynamic and static quenching requires molecular contact between fluorophore and quencher.

In the case of dynamic quenching, the quencher diffuses to the fluorophore while it is in the excited state. By the contact, the fluorophore relaxes to the ground state without emission of a photon. In general, dynamic quenching occurs without a chemical reaction. The collisional quenching of fluorescence can be described by the Stern-Volmer equation:

$$F_0/F = 1 + k_q\tau_0[Q] = 1 + K[Q] \quad (1-9)$$

where  $F_0$  and  $F$  are the fluorescence intensities in the absence and presence of quencher, respectively;  $k_q$  is the bimolecular quenching constant;  $\tau_0$  is the lifetime of the fluorophore in the absence of quencher, and  $Q$  is the concentration of quencher. The Stern-Volmer quenching constant is given by  $K = k_q\tau_0$ .

One of the best-known dynamic quenchers is molecular oxygen, which can quench most of fluorophores. Other types of collisional quenchers include hydrogen peroxide, nitric oxide, nitroxide.<sup>86,87</sup>

For static quenching, the mechanism relates to the formation of a nonfluorescent complex between the fluorophore and the quencher. When the complex absorbs light, it returns to the ground state immediately without photon emission. The effect of static quenching is related to the observed fluorescence intensities by:

$$F_0/F = 1 + K[Q] = 1 + [FQ]/[F][Q] \quad (1-10)$$

where  $K$  is the complex formation constant;  $[FQ]$ ,  $[F]$ , and  $[Q]$  are the concentrations of the complex, fluorophore, and quencher, respectively.

The most effective method to distinguish static and dynamic quenching is the measurement of fluorescence lifetime. In static quenching, the complex fluorophores are nonfluorescent, and the only observed fluorescence comes from the uncomplexed

fluorophores, which are unperturbed. Therefore, the lifetime remains the same as before quenching. In contrast, dynamic quenching involves depopulation of excited state, resulting in the equivalent ratio between lifetime and fluorescence intensity ( $F_0/F = \tau_0/\tau$ ). Another additional method to distinguish static and dynamic quenching is measurement of the absorption spectra of the fluorophores. For collisional quenching, only the excited states of fluorophores are affected, hence there is no change in adsorption spectra. While the complex formation of static quenching causes ground state perturbations, resulting in changes in absorption behavior.

Quenching plays a significant role in sensors for molecular biology. A wide variety of analytes, including oxygen, ions, and heavy metals have been sensed using the fluorescence quenching mechanism.<sup>88,89</sup> Fluorescence quenching can also be utilized to determine the fraction and conformational change of proteins.<sup>90,91</sup> Moreover, target DNA has been analyzed through fluorescence quenching using a variety of oligonucleotide probes, such as molecular beacons (MB), ribozymes, and DNAzymes. Many fluorophore/quencher pairs are intercalated in these probes to track the conformational changes due to the binding of analytes. Examples of well-known fluorophore/quencher pairs include tetramethylrhodamine(TMR)/DABCYL, fluorescein/DABCYL, EDANS/DABCYL, fluorescein/TMR.<sup>92</sup>

### **Fluorescence Resonance Energy Transfer (FRET)**

Fluorescence resonance energy transfer (FRET) is an energy transfer process between two fluorescent molecules. This phenomenon occurs between a donor (D) molecule in the excited state and an acceptor (A) molecule in the ground state.<sup>85</sup> Generally, the donor molecules emit at shorter wavelength, overlapping with the absorption spectrum of the acceptor. The energy transfer occurs through a long-range

dipole-dipole mechanism between the donors and acceptors without photon transfer. The rate of energy transfer depends upon the extent of spectral overlap of the donor emission with the absorption spectrum of the acceptor, the distance between the donor and acceptor, the relative orientation of the donor and acceptor transition dipoles, and the quantum yield of the donor. Typically, the energy transfer occurs within a distance of 100Å. The FRET efficiency is described as followed:

$$E = R_0^6 / (R_0^6 + r^6) \quad (1-11)$$

where the Förster radius  $R_0$  is the distance at which energy transfer is 50% efficient, and  $r$  is the distance between donor and acceptor.

As shown in equation 1-11, FRET is a distance-dependent process. Generally, Förster distances range from 20-60 Å, which is comparable to the size of biological macromolecules. Consequently, FRET has been widely used as a “spectroscopic ruler”<sup>93</sup> to measure the distance between two sites on a macromolecule, especially a protein. FRET has been used to measure conformational change of proteins, distance between a site on a protein and a membrane surface, association between protein subunits, and association of membrane-bound proteins.<sup>94-96</sup> Furthermore, FRET is extensively used in oligonucleotide analysis. Due to the ability to form three-dimensional structures of DNA and RNA, FRET is used to track the conformational changes. Based on this strategy, a number of molecular probes, molecular beacon for example, has been developed using a DNA labeled with a donor/acceptor pair.<sup>97-99</sup> DNA hybridization and many bioaffinity reactions are observed using FRET measurements.

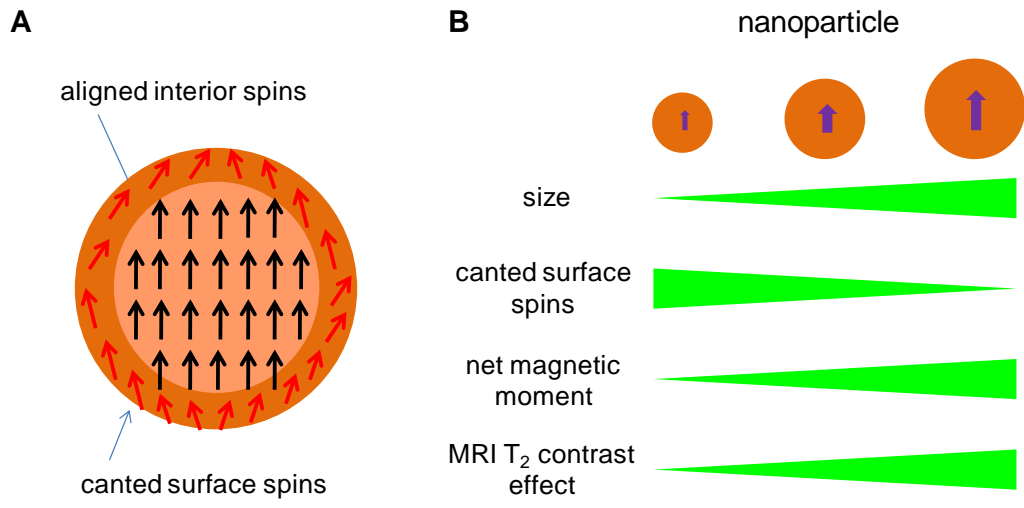


Figure 1-1. Nanoparticle size effects on magnetism. (A) Canted spins appear on the surface surrounding core magnetic atoms. (B) Relationship between surface to volume ratio and size, canted surface spins, net magnetic moment, and  $T_2$  contrast effect.

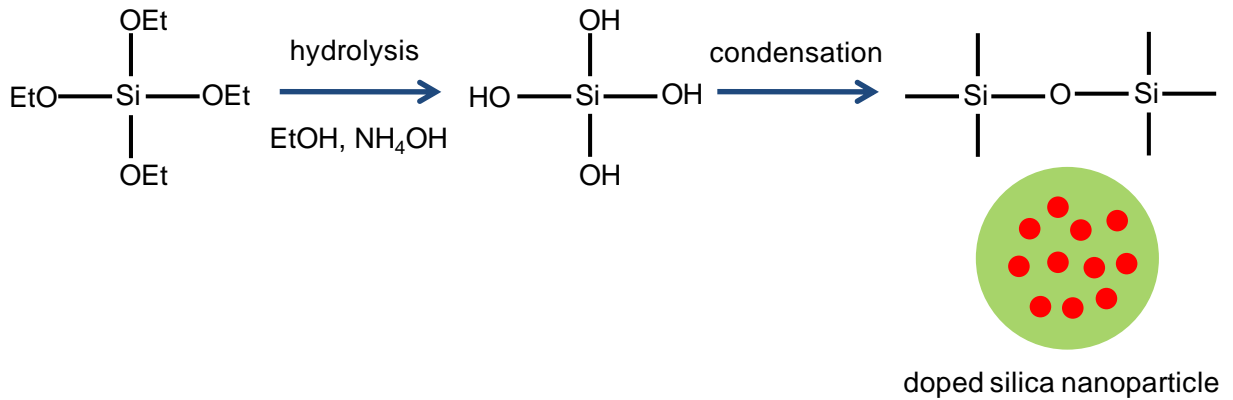


Figure 1-2. Scheme representing the Stober process.

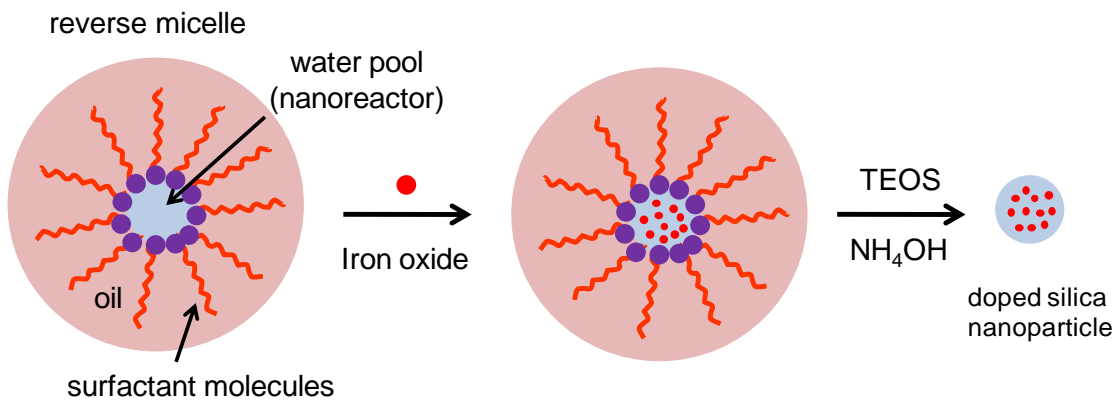


Figure 1-3. Scheme representing a water-in-oil (W/O) microemulsion system.

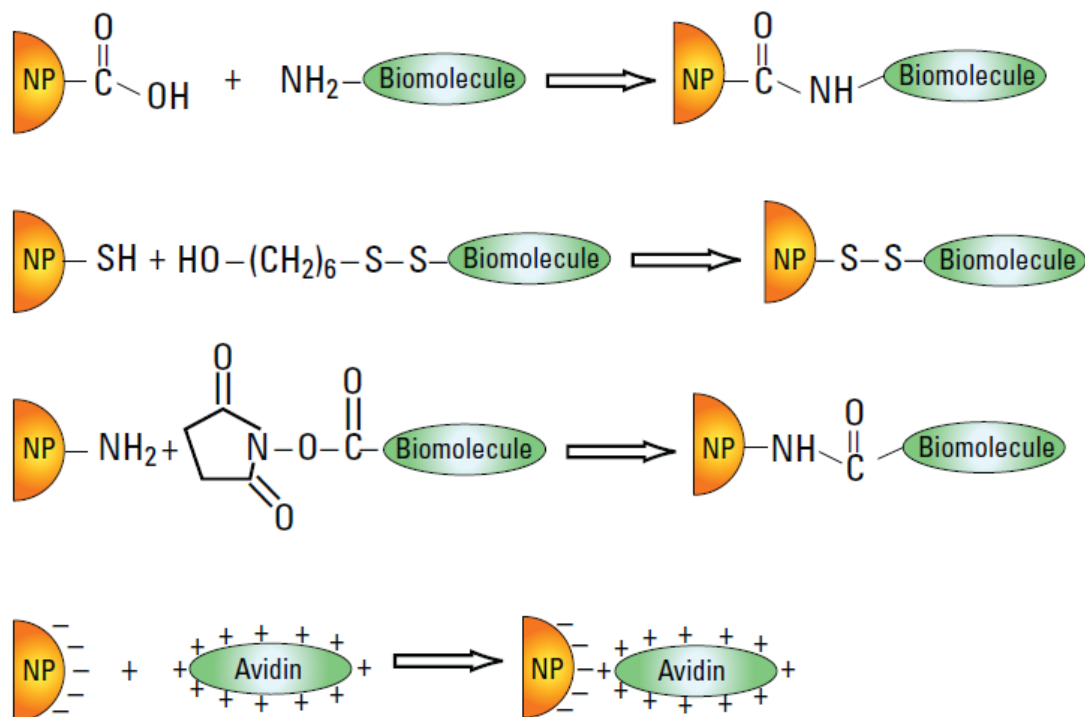


Figure 1-4. Representative bioconjugation schemes for attaching biomolecules to NPs for bioanalysis.<sup>33</sup>

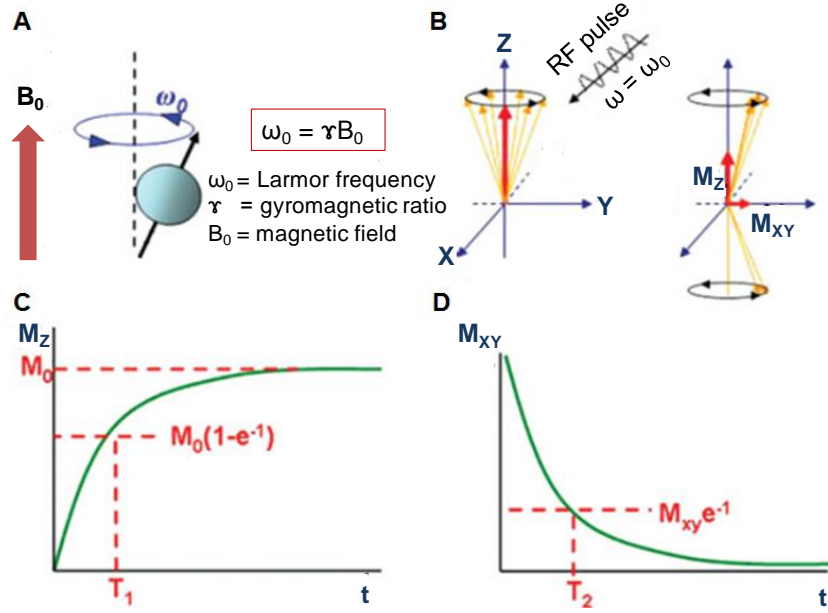


Figure 1-5. Principal of magnetic resonance imaging (MRI).<sup>100</sup> A) Spins align parallel or antiparallel to the magnetic field; small excess parallel to  $B_0$  produces net magnetization in the Z direction. B) After the RF pulse, magnetization of spins changes. C)  $T_1$  relaxation and D)  $T_2$  relaxation.

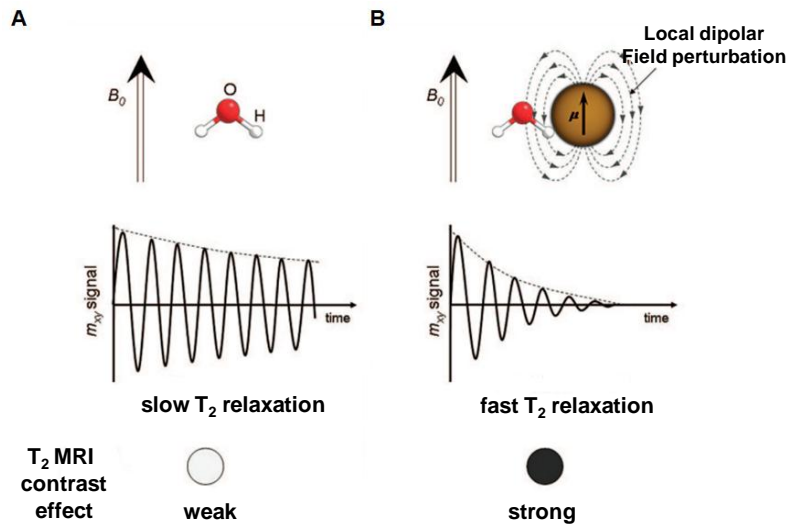


Figure 1-6. The role of magnetic nanoparticles as contrast agents.<sup>4</sup> A)  $T_2$  relaxation mode without MNPs. B)  $T_2$  relaxation in the presence of MNPs.

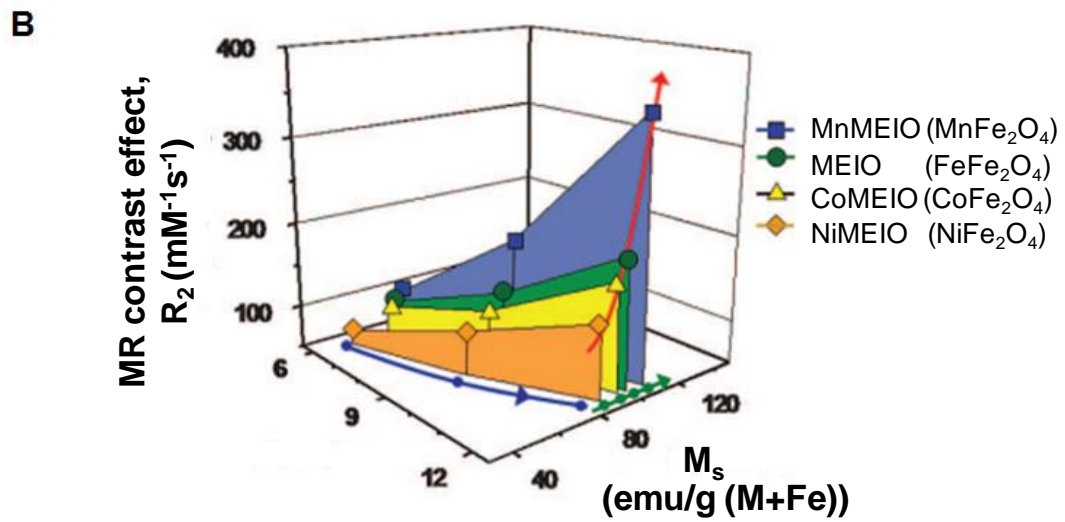
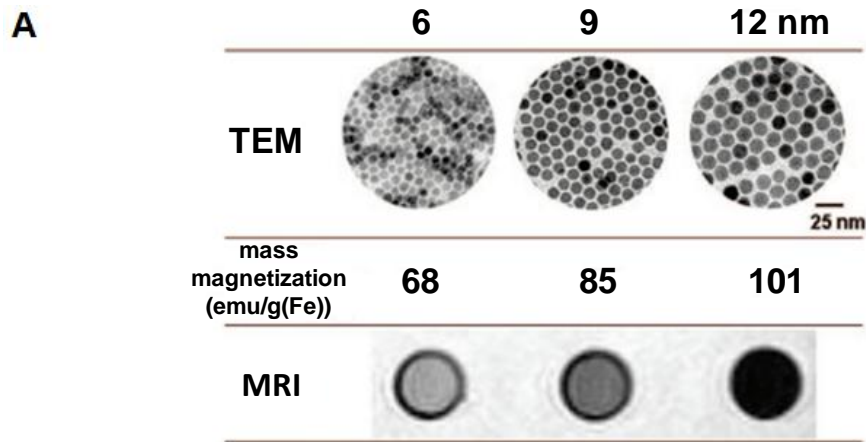


Figure 1-7. Magnetic nanoparticle size and dopant effects on mass magnetization ( $M_s$ ) and MRI contrast enhancement.<sup>4</sup>

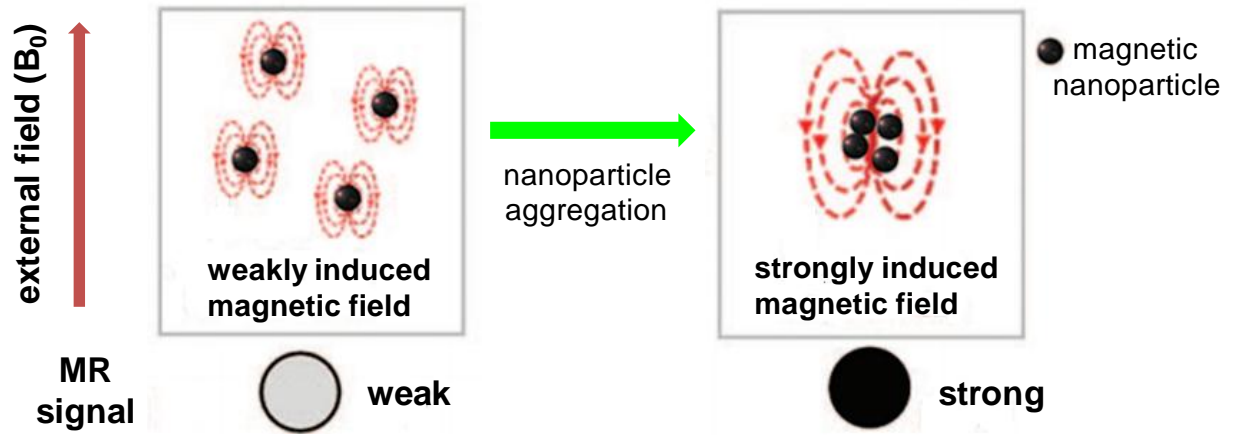


Figure 1-8. Magnetic nanoparticle aggregation effects on MRI.<sup>4</sup>

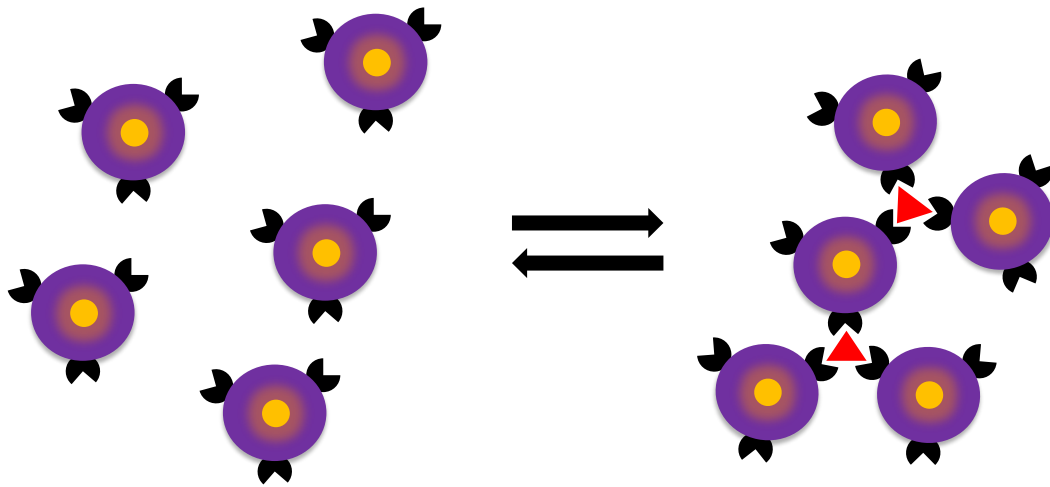


Figure 1-9. Principle of magnetic relaxation switches (MRSw).

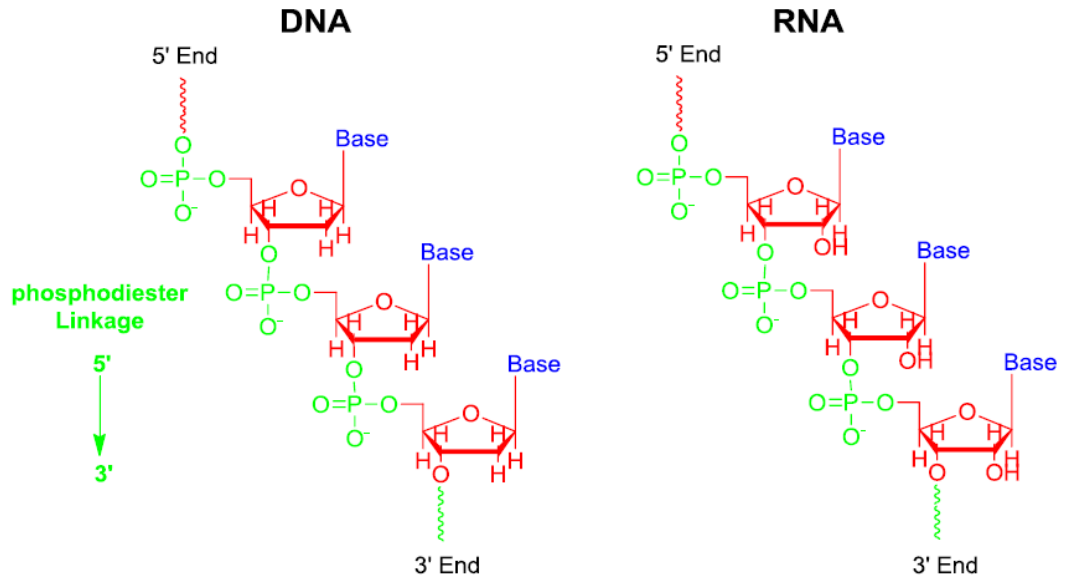


Figure1-10. DNA and RNA structures formed by phosphodiester linkages.

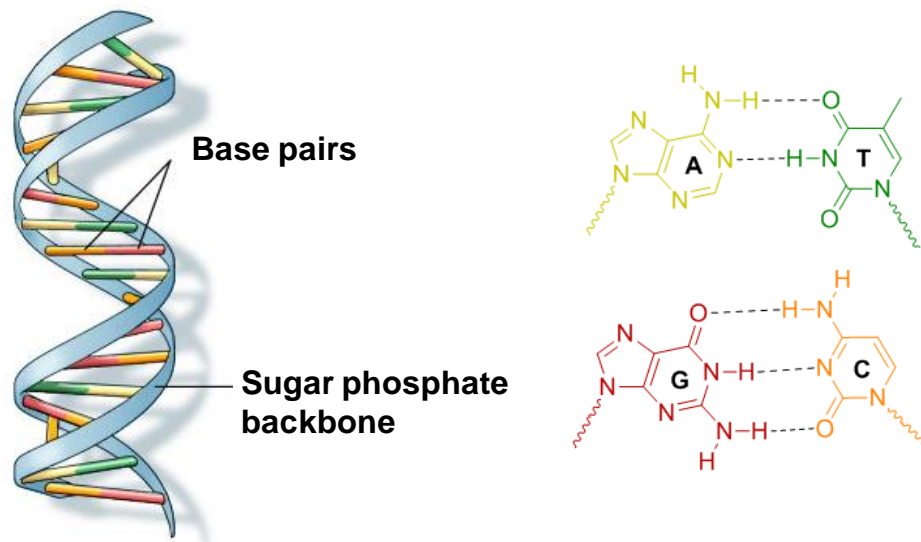


Figure 1-11. Structure of DNA double helix and base pairing.

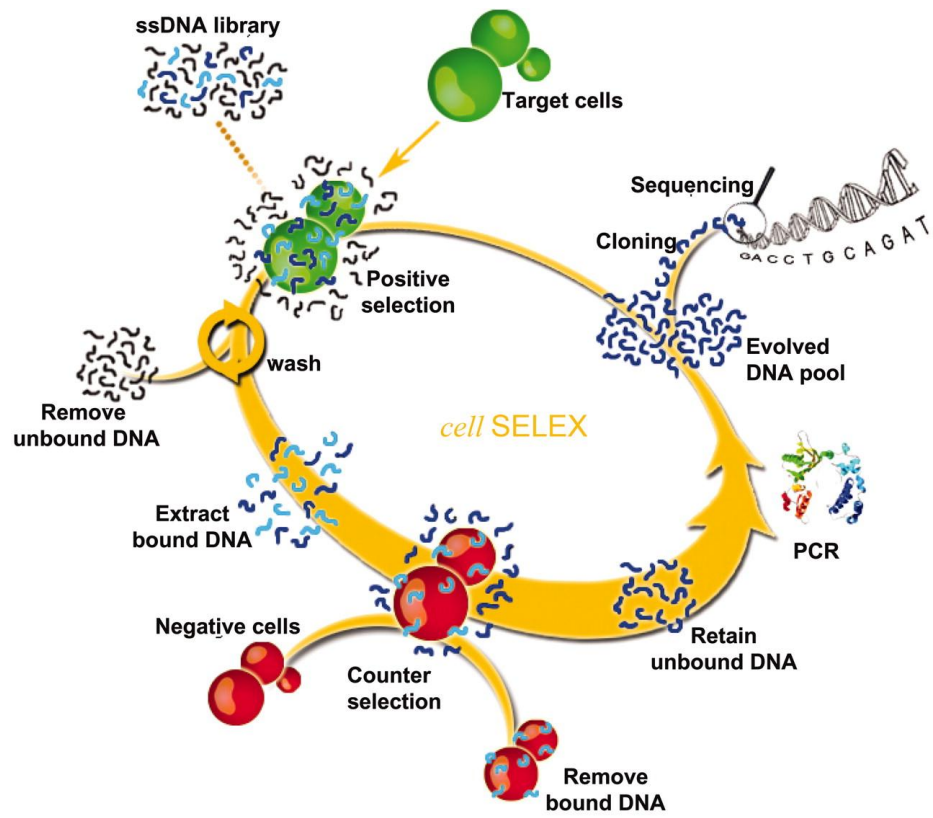


Figure 1-12. Schematic representation of DNA aptamer selection using the cell-SELEX strategy.<sup>74</sup>

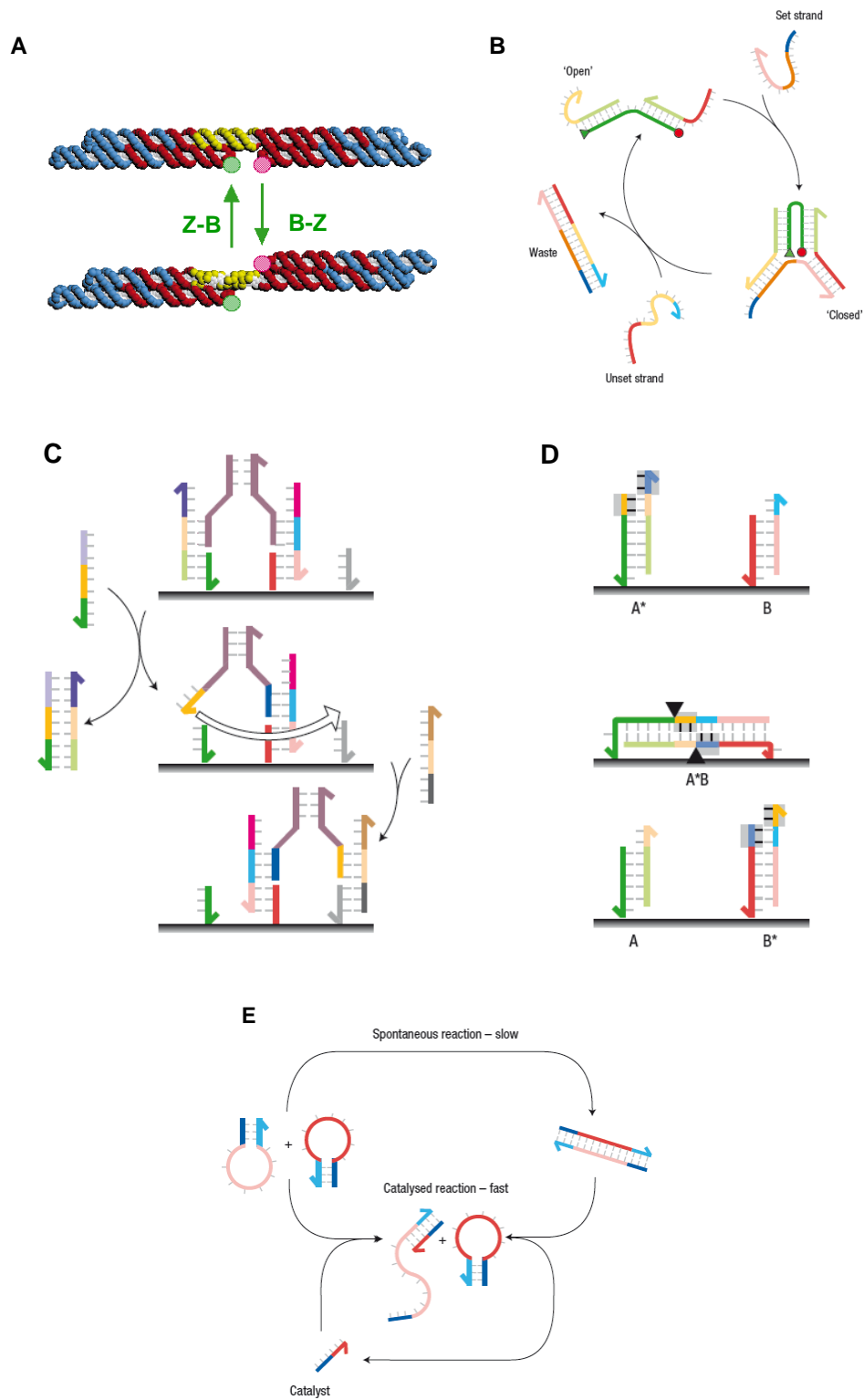


Figure 1-13. DNA nanomachines. (A) DNA Switch.<sup>77</sup> (B) DNA Tweezers.<sup>10</sup> (C) DNA Walker.<sup>12</sup> (D-E) DNA Motors.<sup>13,79</sup>

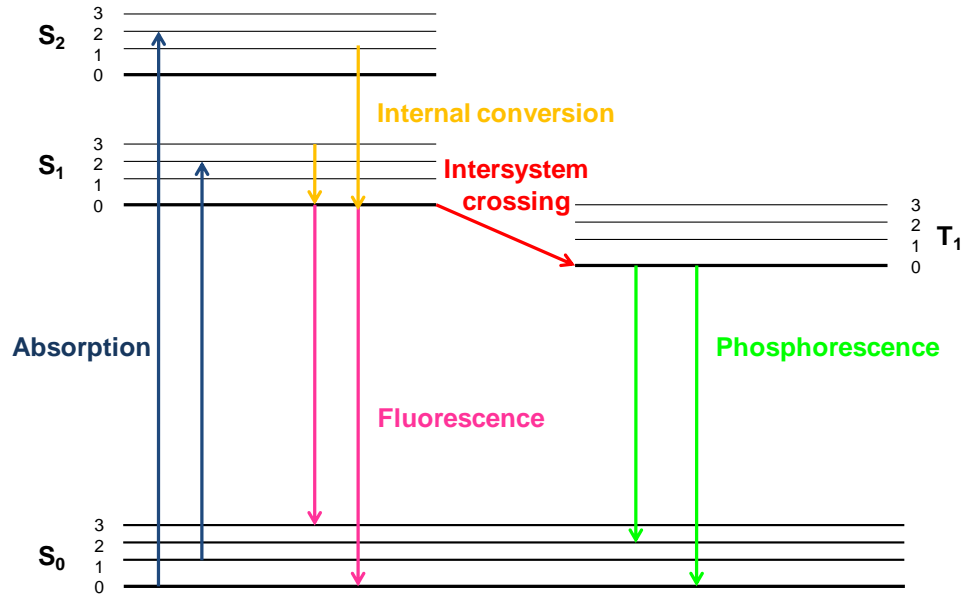


Figure 1-14. Jablonski diagram.

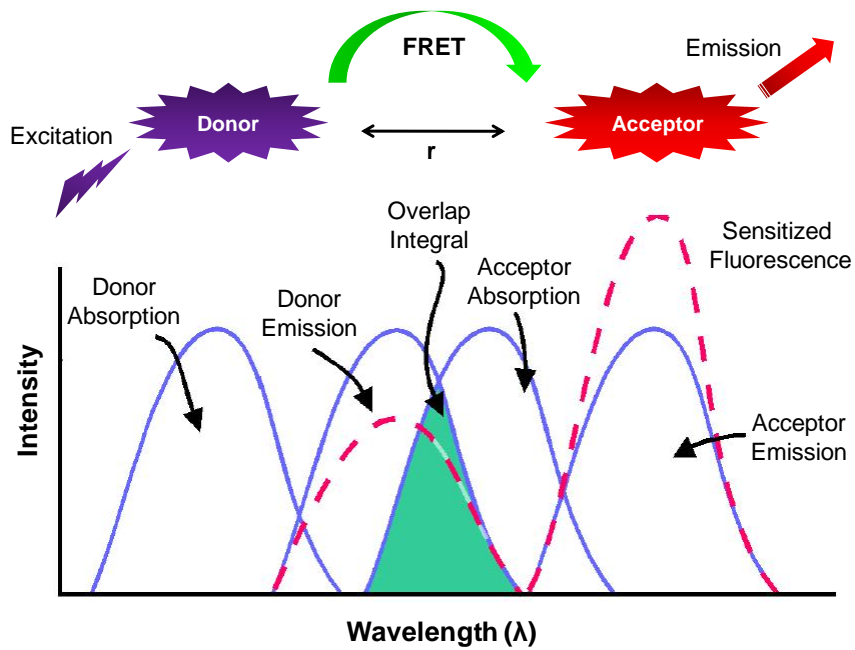


Figure 1-15. Schematic representation of FRET donor and acceptor spectra.

## CHAPTER 2 MOLECULAR PROFILING OF CANCER CELLS USING APTAMER-CONJUGATED MAGNETIC NANOPARTICLES

### Introduction

Because each type of cancer cell has specific intracellular or extracellular biomarkers which distinguish it from non-cancerous cells, a detection method must be able to recognize the given biomarker and bind to it with high sensitivity and specificity. Recently, a new class of ligands, known as aptamers, has been isolated and identified for such specific tumor cell recognition. Aptamers are single-stranded polynucleotides, which recognize specific molecular targets with high affinity and selectivity.<sup>101</sup> They are obtained through an *in vitro* selection process, systematic evolution of ligands by exponential enrichment (SELEX), against a variety of targets, including ions, proteins, and cells.<sup>102,103</sup> Typically, antibodies are used to detect protein targets, but aptamers have several demonstrated advantages over antibodies, such as ease of manipulation, reproducible synthesis, good stability and non-toxicity. Moreover, these properties make aptamers excellent candidates for biochemical sensors, signal transduction, and targeted therapeutic applications.<sup>56,104,105</sup>

To date, several types of nanoparticles have been developed for point-of-care applications using optical signals. However, many of these nanoscale materials, such as quantum dots and dye-doped or gold nanoparticles, are subject to significant background interference by scattering, absorption or autofluorescence within samples, which limits high-sensitivity detection. In contrast, the signals from magnetic nanoparticles (MNPs), are not present in biological samples, resulting in the absence of background noise and, hence, high detection sensitivity. Specifically, the conjugation between aptamers and MNPs, or aptamer-conjugated magnetic nanoparticles

(ACMNPs), constitutes a novel kind of magnetic nanosensor, combining the specific binding ability of aptamers and their easy bioconjugation to solid surfaces, and the large surface areas of MNPs for multivalent interactions.

The detection mechanism of ACMNPs in solution is based on the change of spin-spin relaxation time, or  $\Delta T_2$ , of protons in water. The assembly of ACMNPs upon specific binding with their target cells leads to cluster formation, thereby inducing coupling of magnetic spin moments generating strong local magnetic fields (Figure 2-1A).<sup>38,49,106</sup> At the same time, such local magnetic fields generate inhomogeneities that accelerate the spin-dephasing of surrounding water protons, which results in a decrease in the proton spin-spin relaxation time ( $T_2$ ). Moreover, MNPs are known to enhance the magnetic resonance (MR) signal of protons from surrounding water molecules.<sup>107-109</sup> Under these circumstances, aggregation can be detected by a change in proton relaxation time ( $\Delta T_2$ ), corresponding to the binding event between ligand-conjugated MNPs and target molecules. This phenomenon has led to the development of magnetic relaxation switches (MRSw) for the detection of molecular targets, such as DNA, RNA, proteins, bacteria, viruses, small molecules, and enzymatic activity.<sup>110-114</sup>

Based on previous studies, some cancer biomarkers are not restricted to a single cell type; rather, they are expressed in different cell types or at different developmental states of cancer cells.<sup>115</sup> Thus, multiple cell types at different physiological stages of cancer may show binding towards the same ligand, but with different affinities, depending on the level of biomarker expression. A methodology able to analyze various cancer cells, both qualitatively and quantitatively, can lead to the development of a cancer cell profile and thus greater understanding of cancer pathogenesis and the

potential efficacy of new therapeutic modalities. By using an array of ACMNPs, various cell types can be differentiated through pattern recognition (Figure 2-1B). A distinct pattern of responses generated from a set of ACMNPs would provide a cellular profile allowing clinicians to accurately classify and identify cancer cells at the molecular level. In the following discussion, we will demonstrate the specificity of ACMNPs to their target, explain and demonstrate the viability of MRSw, particularly in complex media, and show that ACMNPs arrays can recognize and differentiate various cell types and, by so doing, can create a distinct pattern recognition profile for various cancer cells.

## **Experimental Section**

### **Synthesis of DNA Aptamers**

The aptamers with strong affinities toward their intact tumor cells were selected by cell-SELEX and were chosen as demonstrated in Table 2-1. All aptamers were synthesized using standard phosphoramidite chemistry with an ABI3400 DNA/RNA synthesizer (Applied Biosystems, CA). Biotin core pore glass (CPG) from Glen Research was used for the synthesis. After the synthesis, the aptamers were deprotected in concentrated AMA (1:1 mixture of ammonium hydroxide and aqueous methylamine) solution at 65°C for 30 min prior to further purification with reversed phase high-pressure liquid chromatography (RP-HPLC). RP-HPLC was performed on a ProStar HPLC Station (Varian, CA) equipped with a fluorescent and a photodiode array detector using a C-18 column (Econosil, C18, 5 µM, 250 x 4.6 mm) from Alltech (Deerfield, IL). The eluent was 100mM triethylamine-acetic acid buffer (TEAA, pH 7.5) and acetonitrile (0-30min, 10-100%). The collected DNA products were dried and detritylated with acetic acid. The detritylated aptamers were precipitated with ethanol and dried with a vacuum drier. The purified aptamers were then dissolved in DNA-grade

water and quantified by determining the UV absorption at 260 nm using a UV-Vis spectrometer (Cary Bio-300, Varian, CA).

### **Aptamer-Nanoparticle Conjugation**

In order to prepare aptamer-conjugated magnetic nanoparticles (ACMNPs), 30 nm streptavidin-coated iron oxide nanoparticles (Ocean Nanotech) were dispersed at 0.1 mg/mL in 100mM phosphate-buffered saline (PBS), pH 7.4. An excess amount of biotin-labeled aptamer was then added to the streptavidin-coated MNPs solution. The mixture was vortexed at room temperature for 1 h followed by three washings with PBS buffer using centrifugation at 14000 rpm to remove any aptamers that did not conjugate to the MNPs. Zeta potential measurements were performed using Brookhaven ZetaPlus at 25°C to determine the successful conjugation of aptamers on the MNPs' surface. The ACMNPs were dispersed in PBS and stored at 4°C at a concentration of 0.1 mg/mL.

### **Cells and Culture Conditions**

The cell lines listed in Table 2-1 were obtained from the American Type Culture Collection (ATCC). CEM, Ramos, and DLD1 cells were cultured in RPMI 1640 medium (ATCC). K562 cells were maintained in culture with IMDM (ATCC). HCT116 cells were grown with McCoy's 5A (ATCC), and LH86 cells were maintained in culture with DMEM (ATCC). All media for cancer cells were supplemented with 10% heat-inactivated FBS and 100U/mL penicillin–streptomycin. HBE135-E6E7, Normal Bronchial lung cell line, was maintained in Keratin Serum Free Medium supplemented with 5 ng/mL human recombinant Epidermal Growth Factor (EGF), 0.05mg/ml bovine pituitary extract (Invitrogen), 0.005 mg/ml insulin and 500ng/mL hydrocortisone. All cultured cells were grown in a humidified incubator at 37°C under a 5% CO<sub>2</sub> atmosphere. In order to obtain single-cell suspensions for the binding studies of adherent cells, cells were cultured

overnight in low density and treated with non-enzymatic cell dissociation solution (MP Biomedicals) for 5min. Cells were aspirated several times, and the single cells were pelleted and washed twice before use in the binding assays. Cell suspensions were centrifuged at 1000 rpm for 5 min, and the pellet was resuspended in 2mL of washing buffer. Ten microliter aliquots of the cell suspension were mixed with 10  $\mu$ L trypan blue solution. Cell quantification was performed using a hemacytometer (Hausser Scientific) and a microscope (Olympus). After determining the cell concentration, serial dilution of cells was prepared in PBS, FBS, plasma, or whole blood and used immediately after preparation.

### **Determination of Conjugated Nanoparticle-Cell Specific Targeting**

To demonstrate specific targeting, CEM cells with their corresponding aptamer, fluorescein (FAM)-labeled sgc8c, were used, and FAM-labeled TDO5 was selected as a negative control. The sgc8c-ACMNPs were incubated with approximately one million CEM cells with the final concentration of 30 $\mu$ g Fe/mL at 4°C for 20 min in PBS. Similarly, TDO5-ACMNPs were also incubated with CEM cells as a negative control. After incubation, the cells were washed twice to remove unbound ACMNPs and resuspended in PBS. The binding of aptamer-conjugated nanoparticles with target cells was investigated using a laser scanning confocal microscope setup consisting of an Olympus IX-81 inverted microscope with an Olympus Fluoview 500 confocal scanning system and a HeNe laser with a photomultiplier tube (PMT) for the detection. The cellular images were taken with a 20x objective. The ACMNPs were excited at 488 nm ( $\lambda_{\text{ex}}$  for FAM), and the emission was detected with a 505-525 nm band-pass filter.

## **Sample Assays using Spin-Spin Relaxation Time Measurement**

To determine the specificity and sensitivity of the detection, 50 $\mu$ L aliquots of CEM cell suspensions with different numbers of cells (1 to 10<sup>6</sup> cells) were incubated with 200  $\mu$ L of sgc8c-ACMNPs solution in PBS ([Fe] = 10 $\mu$ g/mL) at 4°C for 40 min at the final volume of 250  $\mu$ L. Similarly, as a negative control, TDO5-ACMNPs were also incubated with the cells. The spin-spin relaxation times ( $T_2$ ) were measured at 1.5 T by an mq60 NMR analyzer (Minispec, Bruker, Germany), operating at 37°C without a washing step. In order to mimic real clinical samples, which normally contain thousands of different species, similar experiments were also performed in FBS, plasma and whole blood from Innovative Research. To generate the profiling of cancer cells, all cell types listed in Table 1 were dispersed in PBS such that each sample would contain only one cell type and approximately 1000 cells. Each type of ACMNPs was incubated with each cell sample individually using the same conditions mentioned above, followed by the spin-spin relaxation time measurement.

## **Results and Discussion**

### **Magnetic Nanosensor Preparation**

The magnetic nanosensor was prepared by conjugating streptavidin-coated iron oxide nanoparticles with biotin-labeled aptamers. The streptavidin-coated MNPs have an average hydrodynamic diameter of about 30 nm and a zeta potential ( $\zeta$ ) of  $-32.4 \pm 3.7$  mV. The conjugation of aptamers to the MNPs results in an increase of negative charge on the particles' surface (a zeta potential ( $\zeta$ ) of  $-41.8 \pm 2.6$  mV for sgc8c-ACMNPs) arising from the large negative charge of the DNA aptamers. The large surface area of MNPs allows the attachment of multiple aptamers, which result in multiple interactions between ACMNPs and receptors on the cell's surface. The

ACMNPs were stable and well dispersed without precipitation after storage at 4°C for several months.

### **Specificity of ACMNPs**

Although ACMNPs have been previously used for cancer cell separation,<sup>116,117</sup> it is necessary to confirm that the aptamers remain viable in terms of their ability to specifically recognize their targets after conjugation. Therefore, CEM cells and their corresponding aptamer, FAM-labeled sgc8c-ACMNPs, were selected for the demonstration, and FAM-labeled TDO5-ACMNPs were used as a negative control. Since our aptamers were labeled with fluorescent molecules, a fluorescence confocal microscope was used to validate the target specificity of the aptamer conjugate. The binding between the sgc8c-ACMNPs and CEM cells was demonstrated by bright fluorescence, while the control, TDO5-ACMNPs, showed only minimal fluorescence signal (Figure 2-2A and Figure 2-2B). To further validate the specificity, the binding of TDO5-ACMNPs to their corresponding target, Ramos cells, was also investigated. There was also a significant difference in the amount of fluorescence signal seen between the images of the target and control (Figure 2-2C and Figure 2-2D). This observation demonstrated that the ACMNPs maintain the same biological recognition to their targets as the free aptamers.

### **Cancer Cells Detection using Spin-spin Relaxation Time Measurement**

After using the fluorescence technique to demonstrate the specificity of ACMNPs to their targets, the use of MRSw to detect cancer cells was investigated. The first assay was performed to detect CEM cells in PBS. The results showed that 10µg Fe/mL was the optimal concentration for the detection of target cells, since lower concentrations generated significant errors in measurement, while higher concentrations limited the

detection threshold (Figure 2-3). When sgc8c-ACMNPs were mixed with CEM cells, a decrease of  $T_2$  was observed as the number of target cells increased. To verify whether the change of  $T_2$  resulted from specific aptamer-mediated interaction and not nonspecific aggregation of MNPs, TDO5-ACMNPs were also incubated with CEM cells as a control, followed by the relaxation time measurements. To determine the binding,  $\Delta T_2$  was defined as follows:

$$\Delta T_2 = T_{2\text{sample}} - T_{2\text{nonspiked}} \quad (2-1)$$

where  $T_{2\text{sample}}$  is the average  $T_2$  relaxation time of ACMNPs in the presence of target cells and  $T_{2\text{nonspiked}}$  is the average  $T_2$  relaxation time of ACMNPs in the absence of target cells. Figure 2-4 shows a wide dynamic range of detection and excellent correlation between the number of target cells and  $\Delta T_2$  using sgc8c-ACMNPs, whereas the  $\Delta T_2$  of the control had no significant change. In addition, fewer than 10 target cells in 250  $\mu\text{L}$  of PBS could be detected without any amplification method. The detection of Ramos cells was also demonstrated using their corresponding aptamer, TDO5-ACMNPs. The incubation of Ramos cells with TDO5-ACMNPs led to proportional changes of  $\Delta T_2$  with increasing number of cells, while the mixture of Ramos cells and sgc8c-ACMNPs as a control produced only small  $\Delta T_2$  changes (Figure 2-5). These results agreed with our fluorescence assays, as described above, and confirmed the specific recognition of ACMNPs, making this a viable and practical technique for the sensitive detection of cancer cells.

### **Detection in Complex Biological Media**

To further assess the potential of this technique, detection in FBS, plasma, and whole blood samples was also performed. These assays were meant to mimic real clinical samples, which normally contain thousands of different species. The detection

and quantification of CEM cells in FBS was demonstrated by incubating CEM-spiked FBS with sgc8c-ACMNPs. The change of  $\Delta T_2$  was also proportional to the number of target cells, while the control showed only negligible changes (Figure 2-6). It is important to note that this nanosensor can detect as few as 10 cells in 250  $\mu\text{L}$  of serum, which is much lower than the detection limits of conventional fluorescence- or colorimetric-based methods.<sup>118,119</sup> Although the detection of a few target cells has been demonstrated by the chip-based Diagnostic Magnetic Resonance (DMR) system,<sup>53</sup> our nanosensor requires no microfabrication, and the washing step is eliminated. Similarly, CEM-spiked plasma or whole blood was incubated with sgc8c-ACMNPs, followed by  $T_2$  measurement. The results revealed that the detection and quantification of target cells can also be achieved in both plasma and whole blood (Figure 2-7). Nonspecific interactions in complex media containing thousands of proteins caused unwanted aggregates of ACMNPs on the cells' surfaces producing lower relaxation times in both  $T_{2\text{sample}}$  and  $T_{2\text{nonspiked}}$ . The low  $T_{2\text{nonspiked}}$  value generated a higher background, resulting in a smaller  $\Delta T_2$  for detection in complex media compared to detection in buffer with the same concentration of target cells. Nonetheless, we were able to detect as few as 100 target cells in all biological complex media (Figure 2-8).

### **Detection in Mixture of Cells**

The detection of mixtures of targets and non-targets (CEM and Ramos cells, respectively) with different ratios was also demonstrated. One hundred CEM cells were mixed with non-target Ramos cells at different ratios: 1:1, 1:2, 1:5, 1:10, 1:50, and 1:100, respectively. sgc8c-ACMNPs were used to detect the target cells, and random sequenced-DNA conjugated with MNPs was also used as a negative control. The results showed that the target CEM cells can be detected in mixtures of CEM and

Ramos cells with  $\Delta T_2$  similar to those observed in the presence of target CEM cells only (Figure 2-9). For a large number of non-target cells, which may hinder the binding between the ACMNPs and their targets, a slight decrease of  $\Delta T_2$  was observed. However, the detection in mixtures in which the ratio between target and non-target cells was as small as 1:100 was achieved. This result shows promise for detection in complex biological matrices. Successful detection of target cells in FBS, plasma, whole blood, and mixtures of cells indicates that this method can be used for cellular detection in real clinical applications.

### **Cancer Cells Profiling**

With the successful detection of target cancer cells with high specificity and sensitivity, the use of ACMNPs to monitor the interactions between different ACMNPs and multiple cell lines was investigated. The use of aptamers as specific recognition elements provides both qualitative and quantitative information about cell surface receptors. For example, sgc8c aptamer was used to recognize PTK7 receptors on leukemia cancer cells with precise quantitation.<sup>120,121</sup> However, by using an array of ACMNPs combined with the use of the MRSw technique, as described above, recognition patterns were generated resulting in the differentiation of various cell types and, in turn, a cancer cell profile that could be utilized to identify and classify cancer cells more precisely than might otherwise be achieved by a single specific probe.

The target cells were chosen to represent a variety of cancer cell types: a normal lung cell line and six types of representative cancer cells, as listed in Table 1. One thousand cells of each cell line were spiked in PBS, incubated with each ACMNP individually, followed by a  $T_2$  relaxation time measurement similar to that of the previous assays. The six cancer cell lines showed a large variation in  $T_2$  reductions upon mixing

with different ACMNPs (Figure 2-10). The variation of  $\Delta T_2$  upon the incubation of multiple cell types with different ACMNPs can be explained by the different affinities of the aptamers to their target and non-target cells. The aptamers, which have high affinity to their targets, induced ACMNPs to agglomerate on the cells' surface producing large  $\Delta T_2$ , while the non-target cells showed no significant difference in  $T_2$ . Based on the MR response, sgc8c-ACMNPs not only showed strong binding with their target, CEM, but also with the DLD1 and HCT116 cell lines. It was previously described that the target of sgc8c, PTK7, is also expressed in colorectal cancers.<sup>115</sup> As expected, the binding of sgc8c to both colorectal cancer cell lines was observed. Similarly, KCHA10 aptamer was found to interact with most colorectal cell lines,<sup>58</sup> resulting in the recognition of KCHA10-ACMNPs to both HCT116 and DLD1. The other aptamers, KDED2-3, TD05, T2-KK1B10, and TSL11a, which have recognition to only single cell types, demonstrated strong specificity to their targets. Significantly, none of ACMNPs had any interaction with the normal cell line, indicating that targets of these aptamers are related only to cancer. This result also confirmed that the binding based on the interaction of aptamer-cell surface receptors involved and excluded nonspecific interactions. With the low background observed, the detection and profiling can be potentially used for analysis of clinical specimens, which normally contain both diseased and normal cells. Compared to other methods, for example, flow cytometry or cell morphology analysis, MRSw also offers the advantages of simplicity, minimal detection time, and low detection limits.

### **Conclusion**

In summary, we have developed a rapid and sensitive nanosensor for the detection of cancer cells, as well as a method of profiling cancer cells based on MRSw.

The ACMNPs were found to maintain their biological recognition and provide a multivalent effect, resulting in strong interaction with their target cells. Significantly, high sensitivity and specificity could be achieved by this nanosensor for the sample assays in complex biological systems, including serum, plasma, and whole blood. An array of ACMNPs was utilized qualitatively and quantitatively to generate a profile for multiple types of cancer cells. The nanosensor allowed not only the identification of cancer cells but also the differentiation between cancerous and normal cells. Combined with the ease of operating magnetic relaxation instrumentation, the ACMNPs-based nanosensor could become a useful tool for reliable and sensitive detection, as well as cancer screening for clinical use. Furthermore, this demonstration provides strong evidence that the ACMNPs nanosensor has the potential to help identify the protein receptors on the surfaces of various cancer cell types for more informed cancer studies and biomarker discovery.



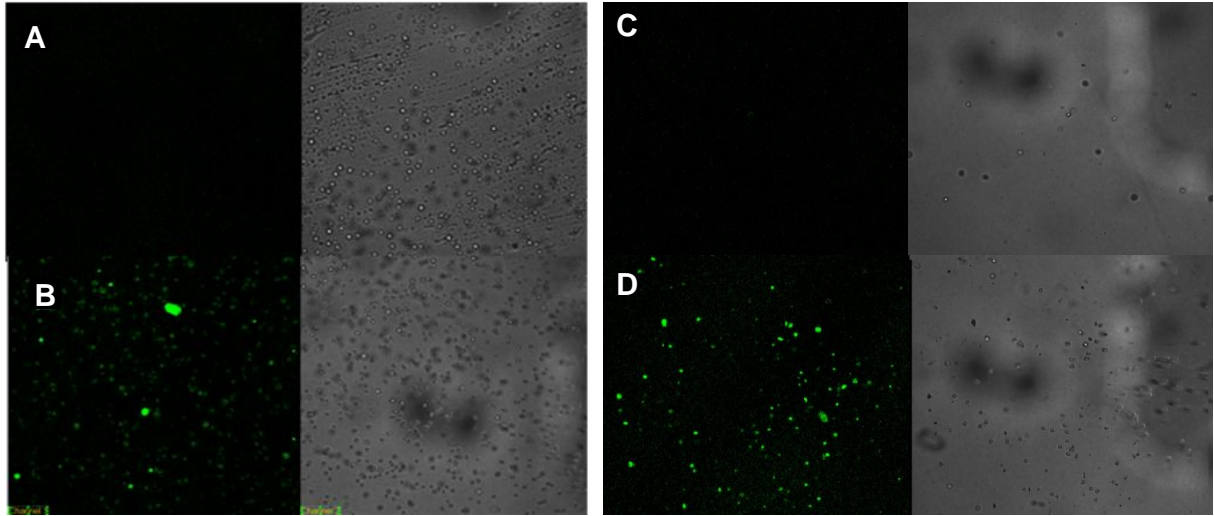


Figure 2-2. The specific recognition of ACMNPs to their target cells. Confocal images (left: fluorescence image, right: transmission image) of CEM cells labeled by (A) FAM-labeled TDO5-ACMNPs and (B) FAM-labeled sgc8c-ACMNPs; Ramos cells labeled by (C) FAM-labeled sgc8c-ACMNPs and (D) FAM-labeled TDO5-ACMNPs. The binding between ACMNPs and their target cells was demonstrated by the bright fluorescence, while the control showed minimal fluorescence signal.

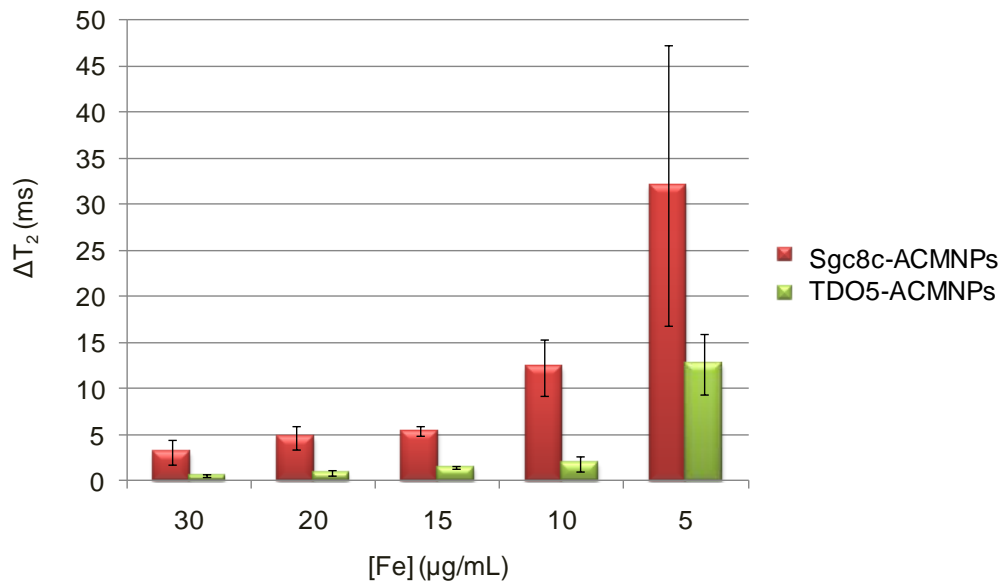


Figure 2-3. The optimization of magnetic nanosensor concentration in PBS. The optimal concentration of ACMNPs for the detection of target cells was determined by using ~100 CEM cells as a target. The result showed that 10 μg Fe/mL is the optimal concentration. The higher concentrations of ACMNPs limited the detection threshold, while the lower concentrations generated significant error for the measurement.

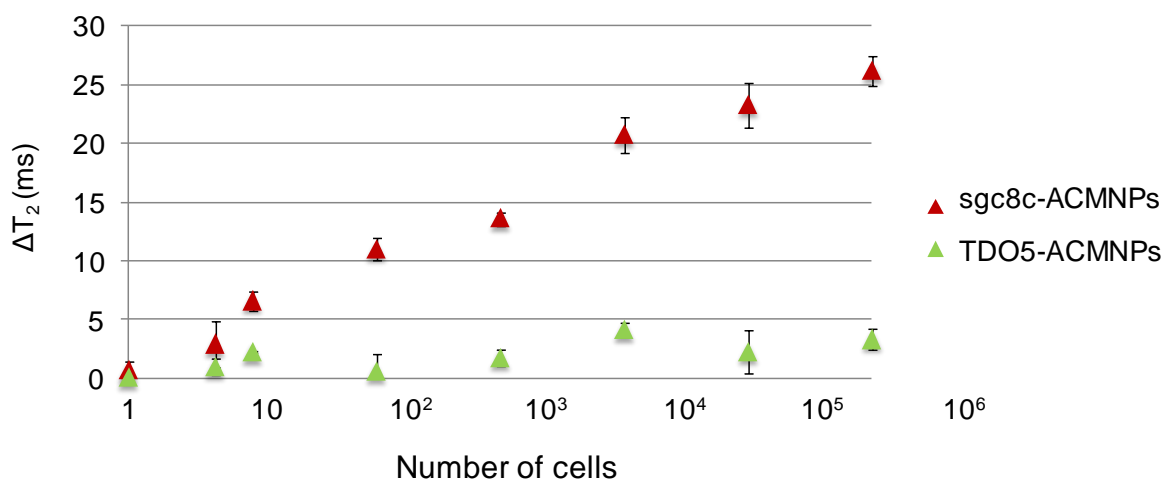


Figure 2-4. sgc8c-ACMNPs as a nanosensor for the detection of CEM cells in PBS. The detection was demonstrated after 40-min incubation at 4°C. TDO5-ACMNPs were used as a negative control. The result showed a wide dynamic range, with a limit of detection as low as 10 cells in 250  $\mu$ L of sample volume

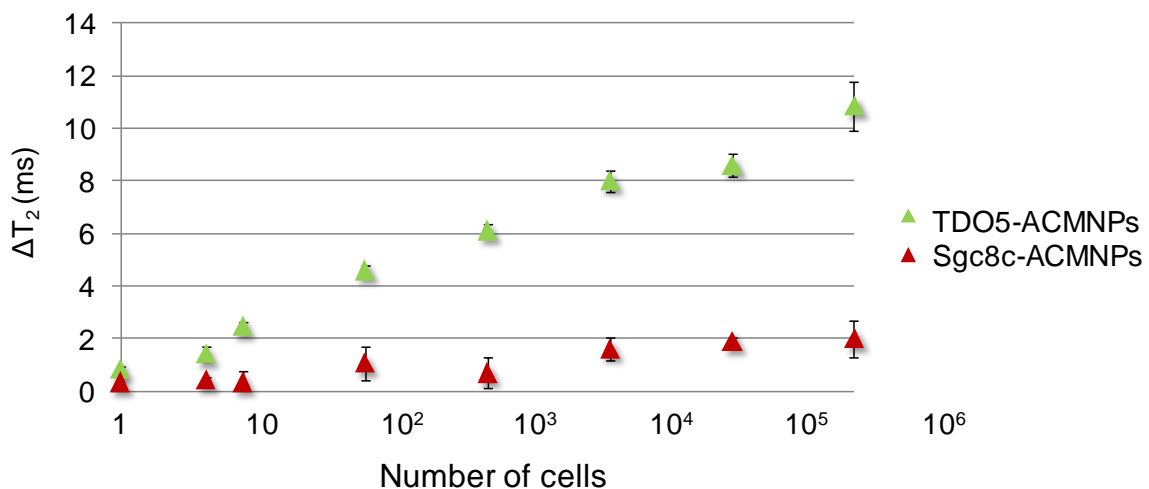


Figure 2-5. The dynamic detection range of Ramos cells using magnetic nanosensor in PBS. The detection of Ramos cells was demonstrated by using TDO5-ACMNPs after 40-min incubation at 4°C. Sgc8c-ACMNPs were used as a negative control. The result showed a wide dynamic range, with a limit of detection as low as 10 cells in 250  $\mu$ L of sample volume, similar to the detection of CEM cells.

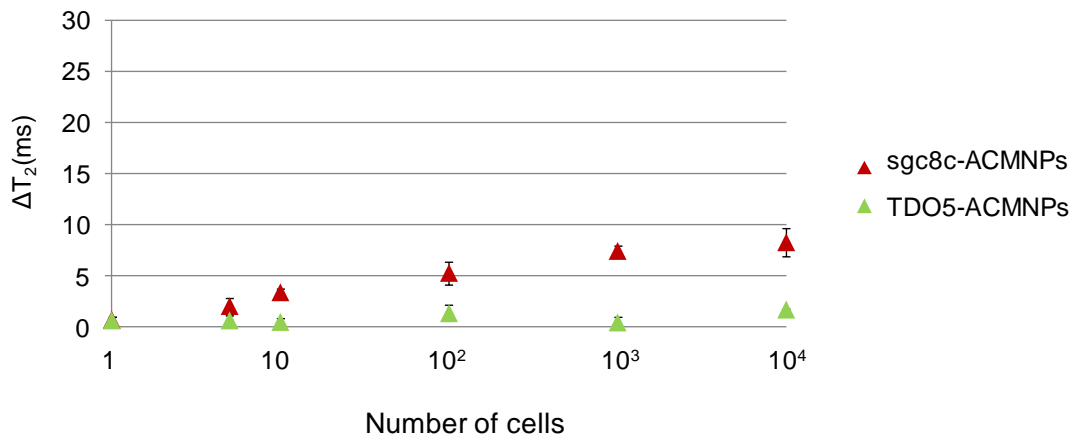


Figure 2-6. sgc8c-ACMNPs as a nanosensor for the detection of CEM cells in Fetal Bovine Serum (FBS). The detection was demonstrated after 40-min incubation at 4°C in 250  $\mu$ L of sample volume. TDO5-ACMNPs were used as a negative control.

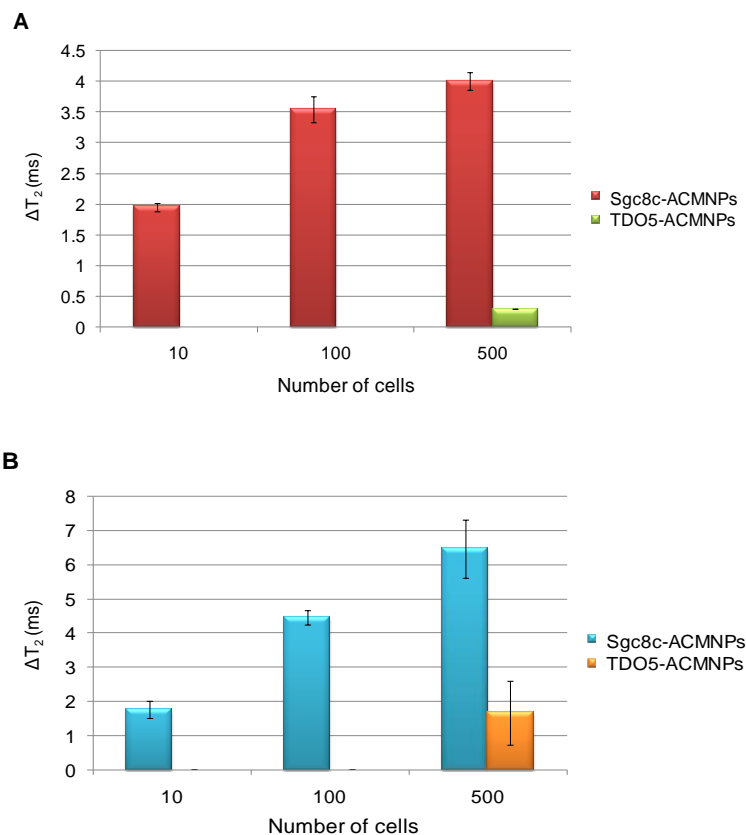


Figure 2-7. The detection of target CEM cells in Human plasma (A) and whole blood (B). The results demonstrated that as few as 100 cells can be detected in CEM-spiked plasma or whole blood with low background.

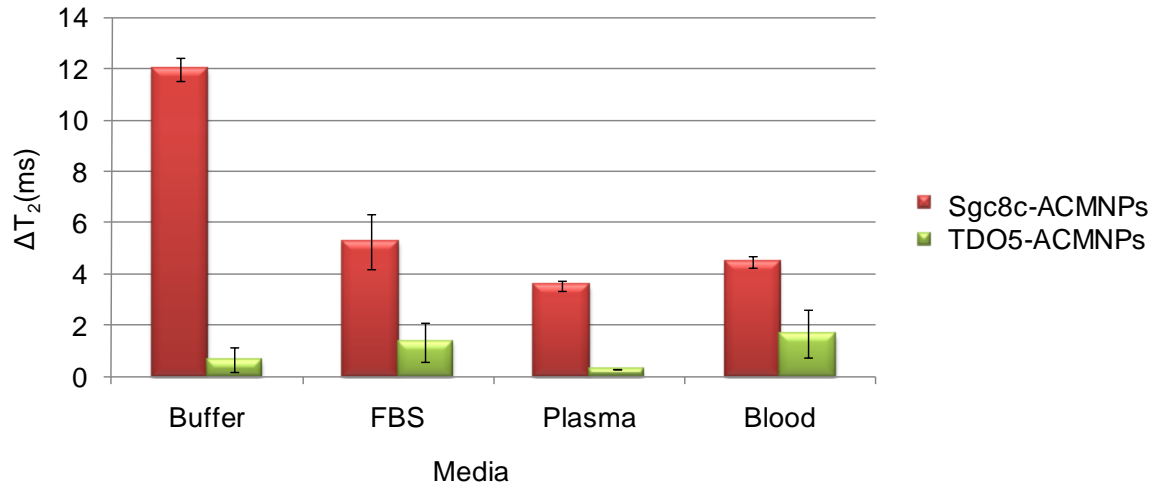


Figure 2-8. The detection of target cells in complex biological media mimics detection in real clinical samples. All the measurements in complex media were performed using ~100 cells in a 250  $\mu$ L sample volume.

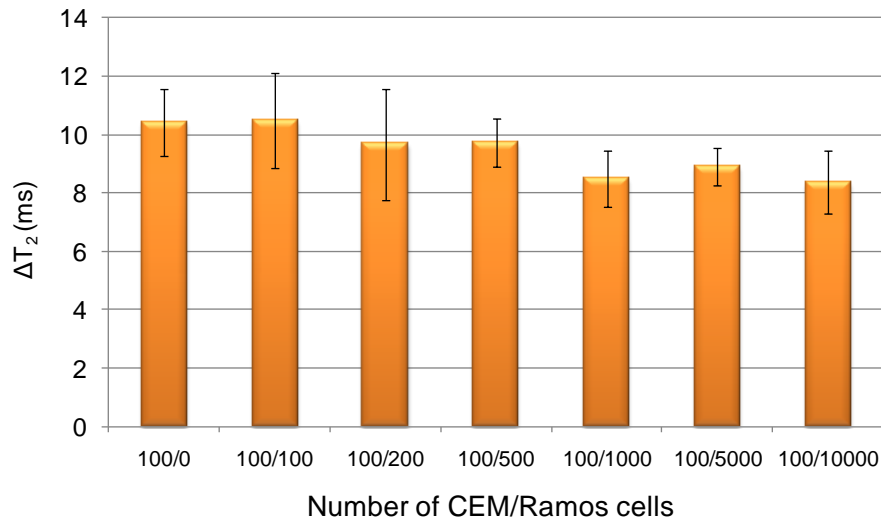


Figure 2-9. The detection of mixed cell samples for the development of rare tumor cells detection. sgc8c-ACMNP were incubated in a mixture of cells, including CEM, target cells, Ramos, and non-target cells, at different ratios.

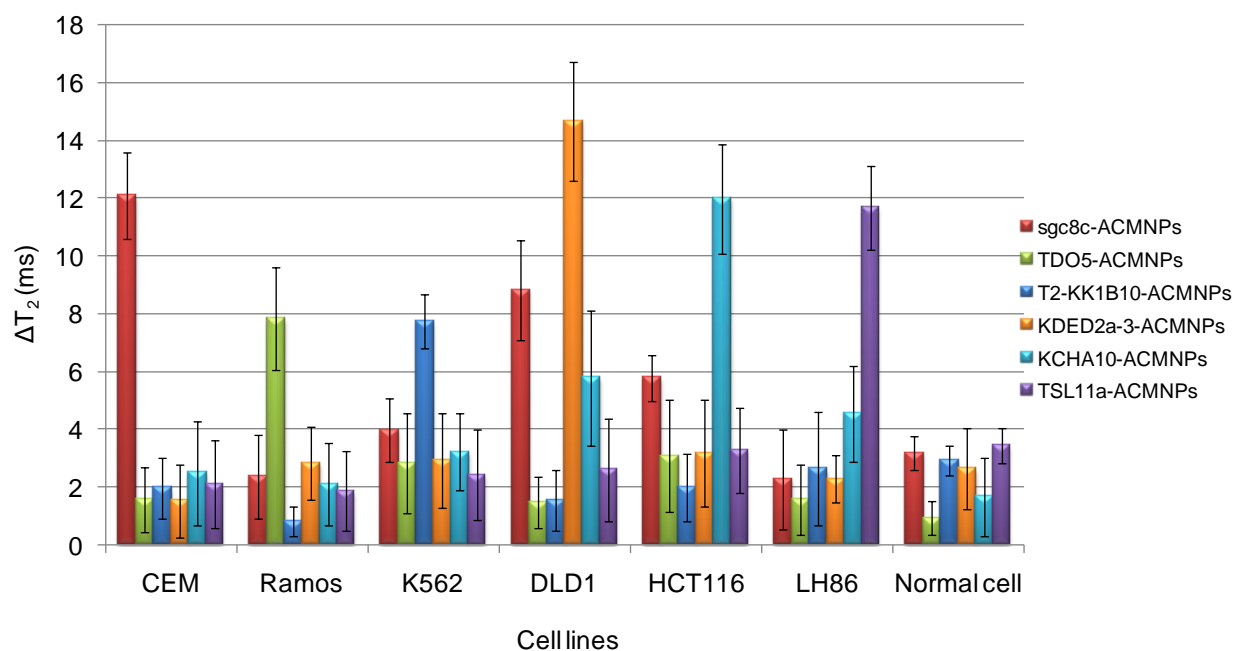


Figure 2-10. Profiling of cancer cells. The changes of  $T_2$  relaxation times obtained by incubating different ACMNPs with multiple cancer cell types or control normal cells. The measurement was performed on ~1000 cells in a 250 $\mu$ L sample volume.

Table 2-1. Representative cell lines and binding affinities of their selected aptamers.

Cell lines	Type of cell	Aptamer	Kd(nM)
CEM	Leukemia	sgc8c <sup>58,a</sup>	0.8
Ramos	Leukemia	TDO5 <sup>122</sup>	75.0
K562	Leukemia	T2-KK1B10 <sup>123,b</sup>	30.0
DLD1	Colon	KDED2a-3 <sup>124</sup>	29.2
HCT116	Colon	KCHA10 <sup>124</sup>	21.3
LH86	Liver	TLS11a <sup>125,c</sup>	7.0
HBE135-E6E7 <sup>d</sup>	Lung	N/A	N/A

<sup>a</sup>sgc8c is a truncated DNA of sgc8.

<sup>b</sup>T2-KK1B10 is a truncated DNA of KK1B10.

<sup>c</sup>TLS11a was originally developed for liver cancer.

<sup>d</sup>Normal cell line.

## CHAPTER 3 DETECTION OF LYSOZYME USING MAGNETIC RELAXATION SWITCHES BASED ON APTAMER-FUNCTIONALIZED SUPERPARAMAGNETIC NANOPARTICLES

### Introduction

Over the past few decades, nanoparticles (NPs) have received considerable attention in advanced biomedical science. The unique characteristics of NPs, such as large surface-to-volume ratio and size-dependent optical and magnetic properties, hold promise for the development of highly sensitive and selective diagnostic tools for clinical use. Specific ligands can be conjugated to a variety of nanoparticles to provide specificity and multivalent affinity. The interaction of NP-ligand conjugates with their target molecules can be transduced into a reporting signal which can be detected by fluorescence, colorimetric, and Raman spectroscopy.<sup>33,126,127</sup> However, many of these NPs, such as quantum dots (QDs) and dye-doped or gold NPs, cause high background interference in biological media by scattering, absorption or autofluorescence, thus limiting highly sensitive detection.

It has been observed that magnetic NPs (MNPs) have the ability to enhance the magnetic resonance (MR) signal of protons from surrounding water molecules.<sup>107,108,111</sup> Aggregation of MNPs induces the coupling of magnetic spin moments and generates strong local magnetic fields. Such local magnetic field inhomogeneities accelerate the dephasing of adjacent water protons, resulting in a decrease of transverse or spin-spin relaxation times ( $T_2$ ). Thus, both aggregation and dissociation of MNP clusters can be detected by a change in proton relaxation times ( $\Delta T_2$ ) by using NMR, magnetic resonance imaging (MRI), or relaxometry. This phenomenon has led to the development of magnetic relaxation switches (MRSw), in which the self-assembly of MNPs, or disassembly of pre-existing magnetic clusters, corresponds to the presence or

absence of specific targets, respectively. Such reversible systems can be designed to detect a variety of targets, such as DNA, RNA, bacteria, viruses, and small molecules, with the MNPs going either from the dispersed to aggregated state or vice-versa.<sup>111-114</sup> Additionally, these magnetic properties are not exhibited in biological samples in the absence of MNPs, resulting in a reduction of background noise, thereby increasing detection sensitivity.

Protein dysfunction in the context of cell regulation and signal transduction is always associated with the development of diseases, especially cancer.<sup>128-130</sup> Advances in protein detection and quantification are essential for pharmaceutical and biomedical research. Recently, aptamers, which comprise a new class of ligands, have been isolated and identified to recognize a variety of chemical and biological molecules with high affinity and selectivity.<sup>101</sup> Aptamers are obtained through an in vitro selection process, which is known as systematic evolution of ligands by exponential enrichment (SELEX), against a variety of targets, such as ions, proteins, and cells.<sup>102,103</sup> Aptamers have several advantages over antibodies, such as ease of manipulation, reproducible synthesis, good stability against biodegradation, and non-toxicity.

In the following discussion, we will demonstrate an aptamer-based sensor for protein detection based on MRSw, using lysozyme (Lys) and anti-Lys aptamers as models. Lys is a highly isoelectric point enzyme (pI~11) that contains 129 amino acids. Generally, a low concentration of Lys is distributed in body tissues and secretions. However, it was reported that elevated levels of Lys in serum, urine, and cells are related to many diseases, such as leukemia,<sup>131</sup> renal diseases,<sup>132</sup> and meningitis.<sup>133</sup> Therefore, the detection and quantification of Lys is very important. In order to

demonstrate the feasibility of our magnetic nanosensors for real clinical analysis, the detection of Lys in serum and cell lysates was also investigated.

## **Experimental Section**

### **Synthesis of DNA**

All DNA samples as demonstrated in Table 3-1 were synthesized using standard phosphoramidite chemistry with an ABI3400 DNA/RNA synthesizer (Applied Biosystems, CA). Biotin core pore glass (CPG) from Glen Research was used for the synthesis. After the synthesis, the aptamers were deprotected in concentrated AMA (1:1 mixture of ammonium hydroxide and aqueous methylamine) solution at 65°C for 30 min, prior to further purification with reversed phase high-pressure liquid chromatography (RP-HPLC) using a ProStar HPLC Station (Varian, CA) equipped with a fluorescent and a photodiode array detector and a C-18 reversed phase column (Econosil, C18, 5 µM, 250 x 4.6 mm) from Alltech (Deerfield, IL). The eluent was 100mM triethylamine-acetic acid buffer (TEAA, pH 7.5) and acetonitrile (0-30min, 10-100%). The collected DNA products were dried and detritylated with acetic acid. The detritylated aptamers were precipitated with ethanol and dried using a vacuum drier. The purified aptamers were then dissolved with DNA grade water and quantified by determining the UV absorption at 260 nm using a UV-Vis spectrometer (Cary Bio-300, Varian).

### **Lys Nanosensor Preparation**

In order to prepare Lys nanosensors, 30 nm streptavidin-coated iron oxide nanoparticles (Ocean Nanotech) were dispersed at 0.1 mg/mL in 100 mM phosphate-buffered saline (PBS), pH 7.4. An excess amount of biotin-labeled Lys aptamer or linker DNA was then added to separate samples of the streptavidin-coated MNPs. The mixtures were vortexed at room temperature for 1 h followed by washing 3x with PBS

buffer using centrifugation at 14000 rpm to remove any DNA that did not conjugate to the MNPs. The conjugates were dispersed in PBS and stored at 4°C at a concentration of 0.1 mg/mL. Equimolar amounts of MNP-Lys aptamer and MNP-Linker were mixed together and dispersed in PBS buffer at a final concentration of 12 µg Fe/mL, leading to cluster formation within 20 min. The spin-spin relaxation times ( $T_2$ ) were measured at 1.5 T by mq60 NMR analyzer (Minispec, Bruker, Germany), operating at 37°C to confirm the aggregation of nanosensors.

### **Magnetic Relaxation Measurement**

The Lys nanosensor was prepared as mentioned in the previous section. A stock solution of protein (0.1mM) was prepared in deionized water and diluted in PBS as necessary. Fifty µL aliquots of Lys with different concentrations were incubated with 200 µL nanosensor mixture in PBS at room temperature at a final volume of 250 µL and [Fe] = 12 µg/mL. The spin-spin relaxation times ( $T_2$ ) were measured after 40 min of incubation without a washing step. The samples with human serum (Innovative Research) were prepared by adding protein and nanosensors to 100% human serum using the same concentration of nanosensors.  $T_2$ -weighted MR images were obtained by using a 11 T NMR instrument with a spin echo pulse sequence, variable echo time (TE) of 50-100 ms and repetition time (TR) of 3000 ms.

### **Cell Samples Preparation**

All cancer cell lines were obtained from the American Type Culture Collection (ATCC). CEM and Ramos cells were cultured in RPMI 1640 medium (ATCC). K562 cells were maintained in culture with IMDM (ATCC). All media for cancer cells were supplemented with 10% heat-inactivated FBS and 100U/mL penicillin–streptomycin. All cultured cells were grown in a humidified incubator at 37°C under a 5% CO<sub>2</sub>

atmosphere. The normal white blood cells (WBC) were separated from whole blood samples (Innovative Research) and transferred into 15 mL tubes. To isolate the WBC, blood was centrifuged at 2000 rpm for 10 min at room temperature. This procedure separated the blood specimen into three layers: an upper plasma layer, a lower red blood cell (RBC) layer, and a thin interface buffy coat containing the WBC. With a transfer pipette, the plasma was first removed, and then the buffy coat was carefully aspirated into a separated tube. Cell suspensions were centrifuged at 1000 rpm for 5 min, and the pellet was resuspended in 2mL of washing buffer. After washing 2x, ten microliter aliquots of the cell suspension were mixed with 10  $\mu$ L trypan blue solution. Cell quantification was performed using a hemocytometer (Hausser Scientific) and a microscope (Olympus). Ten million cells of each cell type were resuspended in 250  $\mu$ L of 1% ice cold CHAPS (3-[(3-Cholamidopropyl) dimethylammonio]-1-propanesulfonate) lysis buffer. The lysates were incubated for 30 min on ice and centrifuged 20 min at 12000 rpm at 4°C. The lysates were transferred to clean centrifuge tubes for Lys assay or frozen at -80 °C. Fifty  $\mu$ L aliquots, which contained lysate from  $1 \times 10^6$  cells, were incubated with nanosensor solution in PBS using the same conditions mentioned above, followed by the spin-spin relaxation time measurement.

## **Results and Discussion**

The MRSw mechanism for the Lys sensor is based on analyte-induced disassembly of MNPs, an event which results in an increase in  $T_2$ , as explained above. As shown in Figure 3-1, iron oxide nanoparticles are conjugated with either Lys aptamer or linker DNA. In the absence of Lys, the linker can hybridize with part of the aptamer (7 bases of the aptamer plus a 5-base extension) to form clusters (short  $T_2$ ). However, in the presence of Lys, the aptamer undergoes a structural change in order to bind with

the target, resulting in base pair disruption. The five remaining base pairs between MNP-Lys aptamer and MNP-Linker are not strong enough to hold the cluster together at room temperature, leading to the disassembly of the clusters (longer  $T_2$ ). Therefore, the Lys-induced disassembly of the clusters can be monitored by this increase in  $T_2$ .

### **Clusters Formation of Lys Nanosensor**

Streptavidin-coated iron oxide nanoparticles were conjugated with either biotin-labeled aptamers or biotin-labeled linker. To prepare Lys nanosensor, equimolar of MNP-Lys aptamer was incubated with MNP-Linker ( $[Fe] = 12 \mu\text{g/mL}$ ) followed by  $T_2$  measurement. Within 5 minutes, the nanosensor showed a decrease in  $T_2$ , indicating the formation of clusters upon the hybridization between the complementary strands (Table 3-2). In contrast, the  $T_2$  of either the individual MNP-Lys aptamer or MNP-Linker showed no significant change. The  $T_2$  of the nanosensor remained constant after 10 min of incubation, indicating that the formation of nanosensors could be completed in a short time. The aggregation was confirmed again by mixing a high concentration of MNP-Lys aptamer and MNP-Linker at  $[Fe] = 100 \mu\text{g/mL}$  and incubating overnight at  $4^\circ\text{C}$ . Precipitation of the nanosensor was observed as a consequence of the formation of large clusters (Figure 3-2). However, the same effect was not observed for individual MNP-Lys or MNP-Linker.

### **Lys-Induced Disassembly of Nanosensors**

To avoid precipitation, the Lys assay was performed with the nanosensor at a low concentration ( $[Fe] = 12 \mu\text{g/mL}$ ). Two hundred fifty nM of Lys was added into the prepared nanosensor, followed by  $T_2$  measurements at 5-minute intervals after adding the target. For each time interval, the change in  $T_2$  ( $\Delta T_2$ ) was calculated by the following equation:

$$\Delta T_2 = T_{2\text{sample}} - T_{2\text{blank}} \quad (3-1)$$

where  $T_{2\text{sample}}$  is the average  $T_2$  relaxation time of three replicates of the nanosensor after protein addition and  $T_{2\text{blank}}$  is the average  $T_2$  relaxation time of three replicates of the nanosensor without target protein. A gradual increase in  $\Delta T_2$  was observed from 5 to 20 min after Lys addition (Figure 3-3), due to disassembly of the magnetic clusters after aptamer binding to the Lys. The signal reached a maximum within 20 min, demonstrating the rapid detection of Lys by the nanosensor.

### **Selectivity and Specificity of Lys Nanosensors**

To assess the selectivity of detection, the change in  $T_2$  was measured within 40 min after adding 50 nM of Lys or 50 nM of some possible interfering proteins, such as insulin, avidin, trypsin, thrombin, BSA, and streptavidin. As shown in Figure 3-4, a significant increase in  $T_2$  upon adding Lys was observed, while the other proteins showed no significant change in  $T_2$  values. The result showed high lysozyme selectivity against other proteins, which may have otherwise have interfered with detection in biological samples.

To confirm that the detection resulted from specific binding between the target protein Lys and nanosensors rather than nonspecific effects, a random DNA sequence conjugated with MNPs was used for nanosensor preparation instead of MNP-Lys aptamer. To demonstrate that Lys cannot induce disassembly of pre-existing clusters prepared between MNP-random sequences and MNP-Linker, seven bases at the end of Lys aptamer and the extended part were preserved in random sequences in order to form the clusters. As expected, the nanosensor prepared by random sequences did not bind with the Lys target, resulting in only minimal change in  $T_2$  (Figure 3-5). This result

confirmed that the disassembly of nanosensors occurs because of interaction of the aptamer-conjugated MNPs with target Lys to the exclusion of nonspecific interactions.

### **Quantitative Analysis of Lysozyme**

The range of detection was determined by measuring the change of  $T_2$  for samples with different concentrations of Lys. The result showed a continuous increase in  $\Delta T_2$  as the Lys concentration was raised from 0 to 500 nM (Figure 3-6). The change of  $T_2$  reached maximum when the Lys concentration increased to more than 500 nM, indicating that binding saturation had occurred between Lys aptamers and their targets. A linear relationship between Lys concentration and  $\Delta T_2$  was observed in the concentration range of 0.5-80 nM with a correlation coefficient ( $R^2$ ) of 0.9914, as shown in the inset of Figure 3-6. Using this nanosensor, Lys could be detected at concentrations as low as 0.5nM without any separation or amplification step. The low detection limit of this nanosensor can be attributed to the high affinity of the aptamer to Lys with a dissociation constant ( $K_d$ ) of 30 nM,<sup>134</sup> as well as the low background noise inherent in MRSw detection.

Detection in complex biological media was also demonstrated by spiking Lys into 100% human serum. The result demonstrated that this nanosensor was able to detect Lys in the nanomolar range in serum, and a linear relationship between  $\Delta T_2$  and Lys concentration from 1 to 80 nM was achieved (Figure 3-7). It is interesting to note that magnetic nanosensors based on MRSw may not offer a very low detection limit compared to fluorescent techniques in buffer systems.<sup>135</sup> Nevertheless, because of the light-independent property of MRSw, and the inherent low background, Lys was detectable in the nanomolar range in complex biological medium without any separation

or amplification step. This result revealed the feasibility of using this magnetic nanosensor in clinical analysis.

The detection of Lys in human serum was also confirmed using  $T_2$ -weighted MR imaging. An increase of Lys concentration led to more disassembly of nanosensor clusters, resulting in an increase in  $T_2$  and an increase in brightness of the  $T_2$  images, as shown in Figure 3-8. The change in contrast was also observed in the nanomolar range of Lys protein which corresponds to detection using a benchtop relaxometer.

### **Analysis of Lysozyme in Cell Lysates**

To validate the use of this Lys nanosensor for real clinical samples, an analysis of Lys in lysates from leukemia cells was performed. CEM, Ramos, and K562 cells were chosen to represent a variety of leukemia cell types. Within this set, normal white blood cells were used as a control. Lysates from one million cells of each cell type were incubated with the Lys nanosensor followed by  $T_2$  relaxation time measurements similar to those in previous assays. The cell lines containing a large amount of Lys could induce a high degree of cluster disassembly, resulting in significant change in  $\Delta T_2$ . Based on the MR response, the three cancer cell lines showed a variation of  $\Delta T_2$ , indicating that different amounts of Lys were contained in each cell type (Figure 3-9). Normal white blood cells showed only a small change in  $T_2$ , indicating a low concentration of Lys. It was previously reported that a high concentration of Lys was detected in myeloid leukemia cells.<sup>136</sup> As expected, a significant increase in  $T_2$  was observed in K562 cells, which belong to a myeloid leukemia cell line, based on their high Lys expression. In contrast, CEM and Ramos, which are T and B lymphoid leukemia cells, showed small  $\Delta T_2$ , similar to that of normal cells, indicating a low Lys expression, a result which agrees with the literature.<sup>136,137</sup> The result suggested that this

magnetic nanosensor could be potentially used for differentiation of Lys levels in specimens between healthy individuals and patients with leukemia.

### **Conclusion**

In conclusion, we successfully demonstrated an aptamer-based biosensor for protein detection using MRSw and Lys as the model target protein. Good selectivity for Lys compared to other proteins was demonstrated by minimal disassembly of pre-existing clusters prepared by random DNA sequences conjugated with MNPs. A detection limit in the nanomolar range was achieved for Lys detection in both buffer and human serum. Detection was confirmed by the  $T_2$ -weighted MR image of Lys-induced disassembly. An assay to determine the level of Lys in cell lysates also demonstrated the potential of this Lys nanosensor for real clinical sample analysis. Overall, this MRSw-based nanosensor offers the advantages of high sensitivity and simplicity for the detection in turbid media and biological samples without protein purification or separation; consequently, the system is feasible for point-of-care diagnostics.

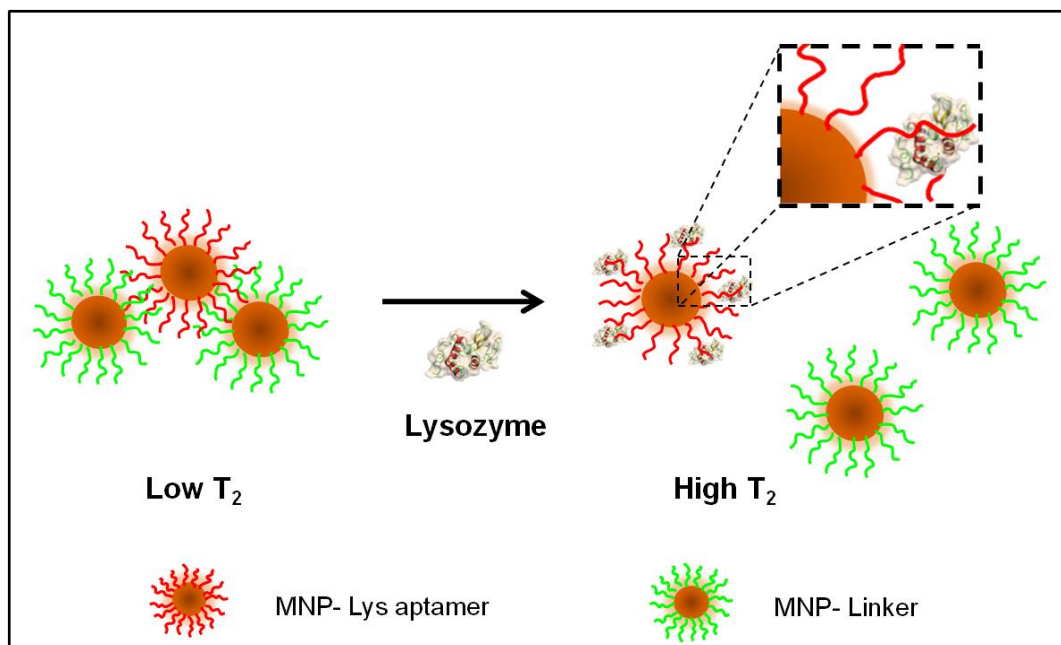
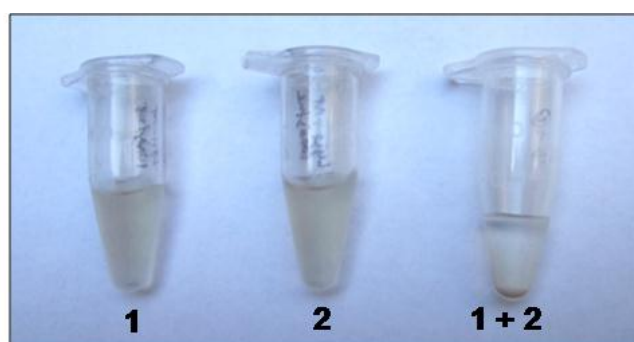


Figure 3-1. Schematic representation of the magnetic nanosensor for Lys detection based on MRSw. The iron oxide nanoparticles are conjugated with either Lys aptamer or linker DNA which can hybridize with the extended part of the aptamer to form clusters. Upon the addition of Lys, the aptamers bind with their targets, leading to disassembly of clusters and increased  $T_2$  relaxation time of the adjacent protons.



1 :  MNP-Lys aptamer    2 :  MNP-Linker

Figure 3-2. Effect of incubating MNP-Lys aptamer with MNP-Linker at high concentration overnight. The individual conjugates showed good dispersion, corresponding to long  $T_2$ . However, the mixture of MNP-Lys and MNP-Linker showed precipitation at the bottom due to the hybridization between complementary strands, resulting in the formation of large clusters.

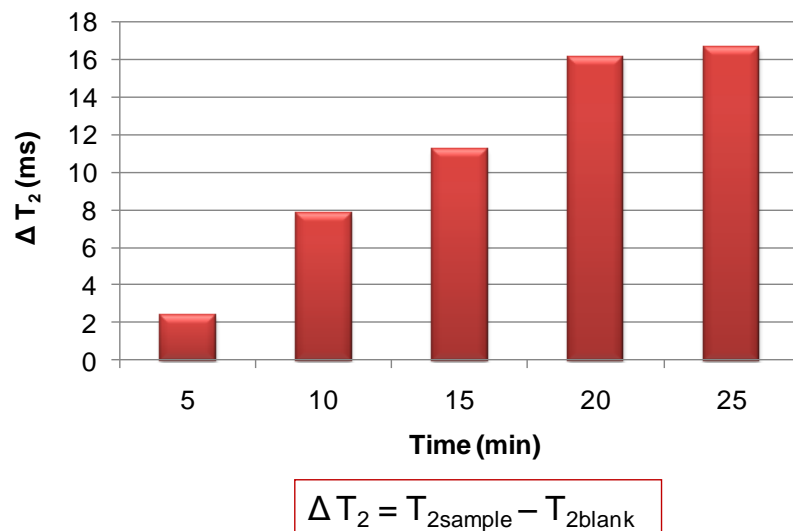


Figure 3-3. A gradual change of  $\Delta T_2$  upon the addition of Lys. The signal reached the maximum within 20 min, indicating the rapid disassembly of magnetic nanosensors.

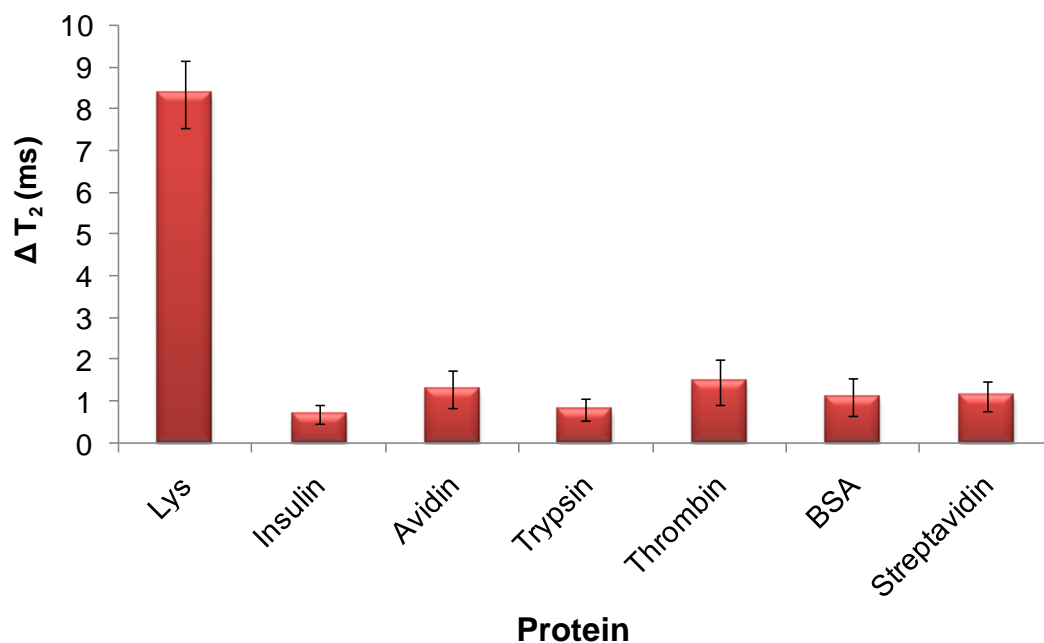


Figure 3-4. Selectivity of the Lys nanosensor. Disassembly of magnetic clusters upon the addition of 50 nM of Lys target was detected by significant change in  $T_2$  relaxation time. At the same time, other proteins, as noted, showed only negligible changes, indicating no interaction with the nanosensor.

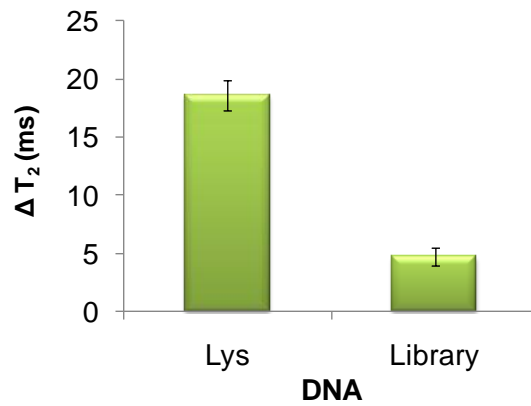


Figure 3-5. Specificity of the Lys nanosensor. Random sequences were employed to test specificity; results showed no binding to target and only minimal change in T2 at a Lys concentration of 250 nM.

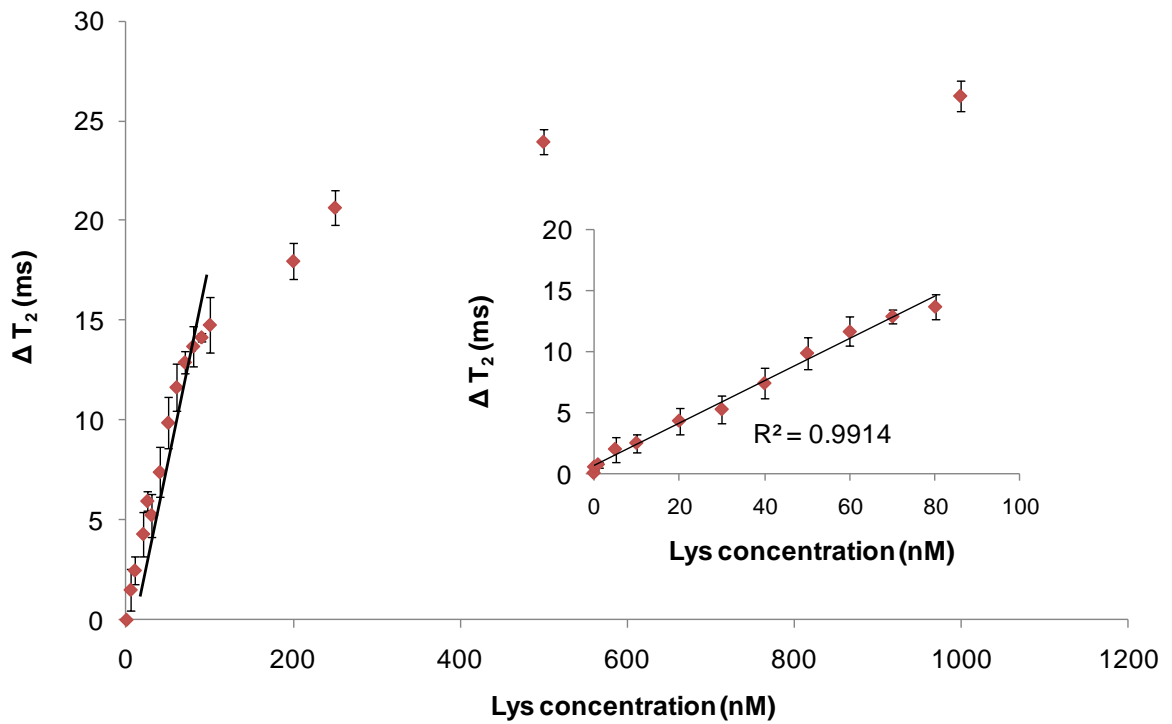


Figure 3-6. Changes in T2 relaxation time with increasing concentrations of Lys. The detection range was determined in PBS; inset: expanded linear region of the curve.

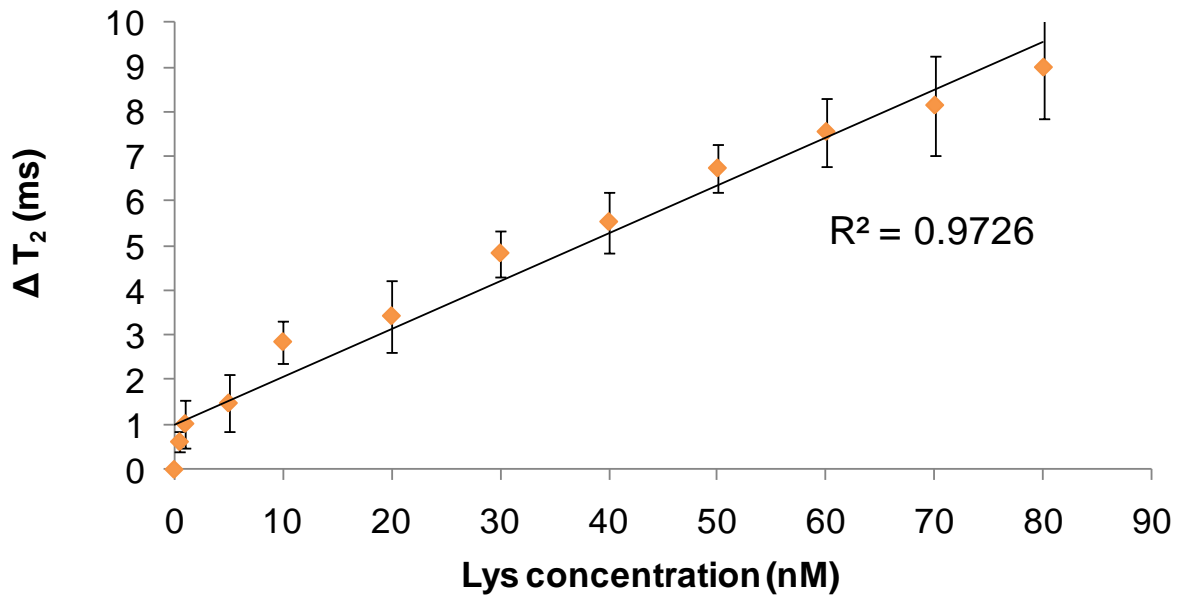


Figure 3-7. The detection of Lys-spiked human serum using relaxometry measurements.

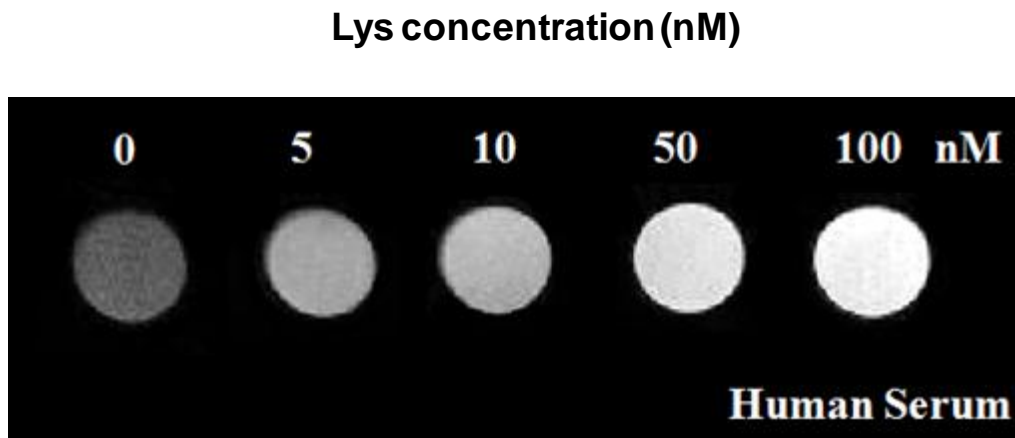


Figure 3-8. The detection of Lys-spiked human serum using  $T_2$ -weighted MR images.

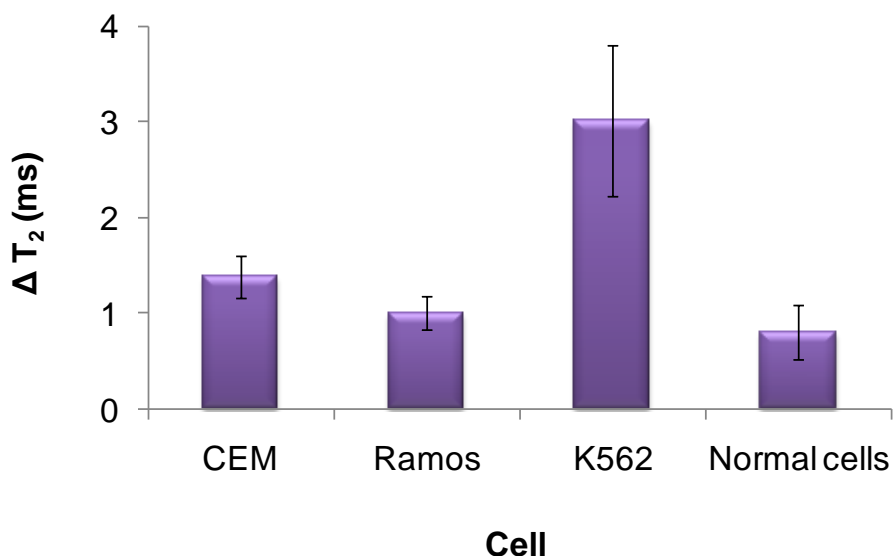


Figure 3-9. Determination of Lys in cell lysates. Normal white blood cells were used as a standard to represent the normal Lys level. A significantly elevated amount of Lys was observed in K562 cells, while CEM and Ramos only showed small differences in Lys levels compared to normal white blood cells.

Table 3-1. List of DNA sequences.

DNA sequences	
Lys Aptamer	5'- <u>AGA GAG ATT CAT</u> TGA GAC GTG AGA AAT CGG GAC TAT <u>TTT TT</u> -Biotin-3'
Library	5'- <u>AGA GAG ATT CAT</u> NNN NNN NNN NNN NNN NNN NNN NNT <u>TTT TT</u> -Biotin-3'
Linker	5'- <u>ATG AAT CTC TCT</u> TTT TTT-Biotin-3'

The underlined bases demonstrate the complementary part, and the blue highlight demonstrates the extended part of Lysozyme aptamer.

Table 3-2. The formation of magnetic clusters upon hybridization between complementary strands. The clusters were detected by changes in  $T_2$  at 5-minute intervals after mixing.

Time (min)	$T_2$ (ms)		
	MNP-Lys	MNP-Linker	MNP-Lys+MNP-Linker
5	93.7±2.1	97.0±1.7	78.0±2.4
10	93.3±1.9	96.8±3.1	76.6±1.8
20	91.6 ±3.7	95.8±2.6	76.2±2.2

## CHAPTER 4 MAGNETICALLY DRIVEN SINGLE DNA NANOMOTOR

### Introduction

In biological systems, nanoscale molecular motors can generate forces from spontaneous reactions of energy-rich molecules, mostly adenosine triphosphate (ATP), to convert chemical energy to mechanical movement. These motors are roughly 10 nm in size, take steps of a few nanometers, and can exert forces in the piconewton range.<sup>138,139</sup> However, to efficiently design and construct nanoscale motors in the laboratory, two key requirements must be satisfied: 1) the generation of forces sufficient to power nanomachines or nanodevices and 2) the exertion of precise control over the motion produced.

Accomplishing these objectives begins with DNA, which is the ideal building block for nanostructures. In addition, DNA can also be used to create dynamic molecules that replicate machine functions including tweezers,<sup>10,79,140</sup> gears,<sup>11</sup> walkers,<sup>13,141,142</sup> and motors.<sup>84,143,144</sup> The DNA nanomotors, which can be operated with high efficiency for several cycles, require exergonic reactions, such as hydrolysis of the DNA backbone,<sup>141,142,144</sup> hydrolysis of ATP,<sup>13</sup> and DNA hybridization.<sup>14,79</sup> However, operating such DNA nanomotors requires the addition and removal of fuels and waste strands for motor function. This mode of operation, however, is accompanied by the accumulation of waste products, which results in decreased motor efficiency. Therefore, coupling the nanomotors to clean alternative energy sources would both eliminate the accumulation of waste products and produce a practical high-efficiency device.

Single molecules can be manipulated through magnetic force by attaching them on magnetic particles and applying an external magnetic field. Using a magnetic field to

control the movement of molecules can also avoid molecular damage from photonic flux. Therefore, the application of a magnetic field could be of great interest as an alternative energy source for DNA nanomotors and could also satisfy the design requirements, as enumerated above.

We have designed a DNA nanomotor which is fueled by an oscillating magnetic field gradient. The nanomotor consists of DNA hairpins that are immobilized on a glass surface inside of a micro-channel and subsequently conjugated to magnetic particles. An external magnetic field gradient is then used to apply a force on the magnetic particles perpendicular to the glass surface, thereby opening the DNA hairpins. We interpret the separation of the 5' and 3' ends of the DNA hairpin during opening as the power stroke of our nanomotor and the hybridization of the hairpin as the recovery stroke. The movement of the hairpin molecule can be monitored by fluorescence resonance energy transfer (FRET) between a fluorophore and a quencher on the stem ends.<sup>99,145,146</sup> Compared with other DNA nanomotor systems, in which the cycles involve the addition of several DNA strands, the magnetic hairpin DNA nanomotor can be operated by the simple application of an external magnetic field gradient. As such, this magnetically driven hairpin DNA nanomotor adds no DNA fuels and generates no DNA waste products after each cycle, in addition to which it can be operated at room temperature with low salt concentration.

## **Experimental Section**

### **DNA Molecular Probes Synthesis**

All sequences as demonstrated in Table 4-1 were synthesized using standard phosphoramidite chemistry. The DNA reagents for the synthesis of DNA hairpins and biotinylated linker were purchased from Glen Research. All DNA hairpins were

synthesized with an ABI3400 DNA/RNA synthesizer (Applied Biosystems, CA). Biotin core pore glass (CPG) was used for all DNA hairpins and DNA linker synthesis. Deprotection of the DNA was performed using overnight incubation with ammonium hydroxide at room temperature. The solution resulting from deprotection was precipitated in cold ethanol. Subsequently, the precipitates were dissolved in 0.5 mL of 0.1 M triethylammonium acetate (TEAA, pH 7.0) for further purification with reverse phase high-pressure liquid chromatography (RP-HPLC). RP-HPLC was performed on a ProStar HPLC Station (Varian, CA) equipped with a fluorescent and a photodiode array detector using a C-18 reverse phase column (Econosil, C18, 5  $\mu$ M, 250 x 4.6 mm) from Altech (Dearfield, IL). The product collected from the HPLC was vacuum dried and then added with TEAA for a second round of HPLC. The final product was collected, vacuum dried and dissolved in 200  $\mu$ L of acetic acid (80%) for 30 min, follow by 200  $\mu$ L of cold ethanol and then vacuum-dried once more. Quantification of all DNA was performed using a UV-Vis Spectrometer (Cary Bio-300, Varian, CA).

### **Molecular Probes Assays**

The maximum fluorescence signal enhancement of each DNA hairpin was observed in solution before and after incubation with excess DNase I in order to determine its extension (or “opening”) efficiency. A mixture of 100 nM of DNA hairpins in 20 mM of Tris-HCl with  $MgCl_2$  and NaCl, pH 7.4 was loaded into a quartz cell for fluorescent spectra. After excitation at 488 nm ( $\lambda_{ex}$  for FAM), the emission spectra were collected at 520 nm ( $\lambda_{em}$  for FAM). After scanning the emission of DNA hairpins for 5 min, 2000 Units/mL of DNase I (Deoxyribonuclease I) enzyme (New England BioLabs, Inc) was added to the solution of DNA hairpins. DNase I catalyzes cleavage of the phosphodiester linkages in the DNA backbone separating the fluorophore from the

quencher to generate the maximum fluorescence signal. It has been reported that the ionic strength, especially the concentration of divalent cations, affects the stability and reactivity of hairpin-structured DNA. To optimize the buffer system, the DNA cleavage by DNase I was performed at pH 7.4 in 20 mM Tris-HCl solution with different concentrations of MgCl<sub>2</sub> (5 and 10 mM) and NaCl (50, 100, and 200 mM). The fluorescence enhancement was calculated using the following equation:

$$\text{Fluorescence Enhancement} = (S_{\text{cleaved}} - B_{\text{buffer}})/(S_{\text{close}} - B_{\text{buffer}}) \quad (4-1)$$

where  $S_{\text{cleaved}}$  is the signal of DNA hairpins after cleavage by DNase I,  $S_{\text{close}}$  is the signal of DNA hairpins prior to cleavage, and  $B_{\text{buffer}}$  is the background fluorescence intensity of buffer.

### **Immobilization of DNA Molecular Probes on Glass Surface**

The surface experiments were performed using microscope slides and glass slips from Fisher (optical borosilicate glass with a size of 45 x 50 mm and 0.13 to 0.17 mm in thickness). The surfaces were cleaned with piranha solution (3:1 ratio of conc. H<sub>2</sub>SO<sub>4</sub>:30% H<sub>2</sub>O<sub>2</sub>), washed thoroughly with deionized water, and dried with nitrogen. Strips of double-sided tape (3M) were placed on the cleaned microscope slide and a cover glass was placed on top to generate micro-channels. The channels were filled with Tris-HCl buffer with optimum concentrations of MgCl<sub>2</sub> and NaCl by capillary action, and the solution was withdrawn with filter paper (Fisher). After washing channels with buffer 3 times, 7 μL of 1 mg/mL avidin was incubated in the channel for 5 min. The excess avidin was removed by washing 3 times with buffer. Next, 7 μL of 5 μM biotinylated linker was incubated in the avidin treated channels for 10 min. After washing to remove excess linker, a solution of 5 μM DNA hairpins was incubated in the channels to hybridize with the immobilized linker for 15 min, and the excess DNA

hairpins were removed by buffer washes. The fluorescence of the DNA hairpins in the closed form was observed by a confocal fluorescence microscope setup consisting of an Olympus IX-81 inverted microscope with an Olympus Fluoview 500 confocal scanning system and an Argon laser with a photomultiplier tube (PMT) for detection, at the wavelength given above using 20x objective. To find the glass-liquid interface, the microscope was first focused on the glass surface of the micro-channel, and a z-section was recorded after each step in the experiment. Each z-section was then analyzed to find the position where the highest signal had been recorded. After immobilization of DNA hairpin on the surface of the channel, DNase I was incubated with the immobilized DNA hairpins for 45 min. Then, the average fluorescence intensities of the image from avidin, immobilized DNA hairpins, and DNase I addition were taken at the same position for that particular channel, and the average fluorescence was monitored to determine the signal enhancement.

### **Construction of DNA Nanomotor**

The DNA hairpins were immobilized on the glass surface and a z-section was recorded following each step as described above. After immobilization of the DNA hairpins, the surface was passivated against nonspecific interactions between magnetic beads and the surface by incubating unreacted avidin with 2 mg/mL of biotinylated-PEG solution for 15 min. The streptavidin-coated iron oxide beads (either 1  $\mu\text{m}$ , 2.8  $\mu\text{m}$  from Dynabeads, Invitrogen, or 0.2  $\mu\text{m}$  from Chemicell, GmbH) were sonicated for 1 min to break up the bead clumps. A 2 mg/mL suspension of the beads was then incubated for 20 min in the DNA hairpins-coated channel. After washing, a z-section was recorded and the average fluorescence signal of the image (closed form) was observed by confocal microscope. A rare earth magnet, NdFeB from Applied Magnets, was attached

to an adjustable stage and positioned directly above the channel for 1 min and the average fluorescence intensity was measured at the same position to observe the open state of the DNA hairpins. Three minutes after removal of the magnet, the closed state of DNA hairpins was observed by fluorescence. The magnet was positioned and removed for several cycles to measure the change between shrinkage and extension of the DNA nanomotor.

## **Results and Discussion**

The DNA hairpins and biotinylated linker are summarized in Table 4-1. Specifically, DNA hairpin structures were selected because they can be switched from the “closed” (contraction) state to the “open” (extension) state. Each DNA hairpin has 20 thymidine (T) bases in the loop and 6, 9, or 12 base pairs (6ds, 9ds, or 12ds) in the stem part. In order to visualize movement between the two states, a fluorophore (FAM) is attached to one arm of the stem and a quencher (Dabcyl) on the other arm of the stem. Poly T (20 bases) was used as the spacer between DNA hairpins and magnetic beads at the 3' end, and 15 bases were incorporated at the 5' end to hybridize with a DNA linker which was immobilized on a glass surface. It is necessary to point out that the fluorescence resonance energy transfer (FRET) pair is not needed for motor function but gives a convenient way to monitor the motion of the motor. The fluorescence intensity is related to the distance between the FRET pair in the stem ends, which indicates the closed or open state of the DNA nanomotor movement.<sup>99,145,146</sup> As shown in Figure 4-1, an external magnetic field attracts the magnetic beads, which are conjugated to the 5' end of the DNA molecular probes, to trigger the opening and closing of DNA hairpins. In order to control the movement, the 3' end is tethered to a glass surface. In the absence of the magnetic field, the DNA

hairpins are in the contracted state and the fluorophore is quenched by FRET. When the external magnetic field is applied, the magnetic beads are attracted to the magnet and cause the DNA hairpins to extend, restoring the fluorescence signal.

### **Signal Enhancement of the DNA Molecular Probes by Dnase I Cleavage**

The signal enhancement of three DNA hairpins in solution was tested and the results are shown in Figure 4-2. The DNA hairpins with longer stems exhibit lower background fluorescence, however, the DNA hairpins with fewer base pairs in the stem yielded higher signal enhancement after DNase I addition by the higher enzymatic cleavage efficiency.

We further tested the signal enhancement of the DNA hairpins immobilized on glass surface by DNase I. Since the DNA nanomotor will be immobilized and operated on a glass surface, the fluorescence signal enhancement of each DNA hairpin on the micro-channel surface was also determined. Equation 4-1 was also used to calculate the signal enhancement for DNA hairpins immobilized on the glass slide, and the results are shown in Figure 4-3. On the glass surface, the signal enhancement of DNA hairpins decreases significantly compared to that of DNA hairpins in solution. Whereas DNA hairpins can typically achieve fluorescence enhancements above 25-fold in solution, these values can drop to 2 to 5-fold once immobilized. This behavior mainly results from the interaction between the DNA hairpins and the surface, which disrupts the loop and destabilizes the DNA hairpins' structures. This can cause inefficient quenching, which is reflected in higher background signal, thus results in lower signal enhancement.

## DNA Nanomotor Driven by Magnetic Field

Generally, the mechanical response of a single DNA molecule to an applied force can be divided into entropic and elastic responses.<sup>147</sup> Entropic responses are driven by thermal energy, and elastic responses are generated by base-pair interaction. Thermal energy corresponds to Brownian motion, which is proportional to small fluctuation of flexible DNA molecules tethered to magnetic beads. Typically, the thermal fluctuation of a single DNA molecule is less than 5 pN.<sup>148</sup> Our system involves DNA base-pair interaction, i.e., the unzipping of the DNA hairpins. By using atomic force microscopy (AFM), it was reported that the DNA unzipping force of 10 base pairs is about 10 pN depending on the local G-C content.<sup>149</sup>

As expressed in equation 4-2, the force acting on a magnetic particle is proportional to the external field strength and the magnetic moment of the particle.<sup>150,151</sup>

$$F_m = \nabla(m \cdot B) \quad (4-2)$$

where  $m$  and  $B$  are magnetization of the particle and magnetic induction, respectively.

Magnetic field gradient has been successfully used to manipulate tethered-bead DNA molecules with generated force up to 20 pN where the maximum value of the force depends on the size of a particle.<sup>150,151</sup> When the magnet position is fixed, the force acting on the magnetic particle can be kept constant because the spatial region occupied by the particle is small enough for the magnetic field gradient to be considered uniform.

In order to demonstrate a DNA nanomotor driven by magnetic field gradient, DNA hairpin and magnetic beads were immobilized on a glass surface followed by the

investigation of magnetically controlled process. To optimize the motor system, two design factors were investigated: the number of base pairs in the stem part of the DNA hairpins and the size of magnetic beads. In normal condition, the DNA hairpins were in the contracted (closed) conformation, and the hairpin structure was maintained. When the external field was applied to drive the movement of the DNA nanomotor, the magnetic particles experienced sufficient force to unzip and extend the DNA hairpins as the power stroke of the motor. After removal of the external field, the DNA molecular probes reformed to the hairpin structure as the recovery stroke. By repeated application and removal of the external magnetic field, the DNA hairpins can be regarded as a reversible DNA nanomotor as demonstrated by the fluorescence signal changes shown in Figure 4-4A. It is important to point out that the extension of DNA molecular probes as the power stroke occurred within 1 minute and a few minutes were used to reform the hairpins as the recovery stroke.

Based on the assumption that the diameter of the DNA duplex is 2.2 nm and the distance between two bases is 0.34 nm, we estimated the distance variation between closed and open states to be 2.2 nm and 10.8 nm, respectively, for the DNA hairpin with 6 base pairs in the stem part.<sup>67,150</sup> Accordingly, molecular motors moving with larger steps generate more forces. Therefore, to change distance and create a larger working stroke, the number of base pairs in the stem part of the DNA hairpins was varied. As such, longer distance in the open state, i.e., from 10.8 nm to 12.9 and 14.9 nm, was achieved by changing from 6 to 9 and 12 base pairs in the stem part of the DNA hairpin, respectively. However, increasing the number of base pairs requires more force to unzip the DNA hybridization resulting in slightly less fluorescence intensity change for each

cycle of the motors as shown in Figure 4-4B and 4-4C. All DNA hairpins with 6, 9, and 12 base pairs show consistent recovery and the signal enhancement shows no tendency to decrease after 5 cycles using 1  $\mu\text{m}$  magnetic beads. This result confirms consistent efficiency and no influence of fluorescence bleaching after several cycles of operation. Excess amount of DNase I enzyme was added at the end for each nanomotor to compare the fluorescence signal of each DNA hairpin with the maximum fluorescence signal. In this way, we can calibrate the system to achieve consistency. By setting the fluorescence intensity when DNA hairpins were in the closed state as a baseline (0%) and the intensity after addition of excess DNase I as 100%, we can estimate the number of DNA hairpins in the open state for the magnetically controlled process. We use a fluorescence recovery parameter, recovery (%), to evaluate the opening efficiency of DNA molecular probes as follows:

$$\text{Recovery (\%)} = (I_{\text{open}} - I_{\text{closed}})/(I_{\text{cleaved}} - I_{\text{closed}}) \quad (4-3)$$

Where  $I_{\text{open}}$  is the average fluorescence intensity of DNA hairpins after external magnetic field application,  $I_{\text{closed}}$  is the average fluorescence intensity after removal of the external field, and  $I_{\text{cleaved}}$  is the average fluorescence intensity after adding DNase I enzyme. The higher recovery value demonstrates the higher amount of DNA hairpins in the open state by external magnetic field application. When we used recovery (%) to compare the opening efficiency of all DNA hairpins under the same conditions, we found approximately 37.6% of recovery for DNA hairpins with 6 base pairs, 36.4 % for 9 base pairs, and 35.6% for 12 base pairs, respectively. This result supports our assumption that more force is needed to unzip the hybridization of hairpin structure,

when more base pairs are added. However, the recovery of each DNA molecular probe is slightly different.

Since the external magnetic field gradient is kept constant, the maximum force reacts to DNA nanomotor depends on the size of the magnetic particle. In order to generate different forces for the power stroke to drive the DNA nanomotor, the effect of different sizes of magnetic beads was also observed using 2.8  $\mu\text{m}$  and 0.2  $\mu\text{m}$  magnetic particles, as shown in Figure 4-5, Figure 4-6 and Figure 4-7, respectively. Interestingly, all DNA hairpins show slightly lower signal enhancement for each cycle when the larger particles were used. This behavior of the 2.8  $\mu\text{m}$  system is mainly attributed to a lower signal in the opened state compared to the 1  $\mu\text{m}$  system. The larger particles have a larger radius of curvature and this allows more hairpins to form the link between the surface and the bead, thus increasing the force needed to pull the bead away from the surface. This increase in force to open more hairpins is balanced by the increase in force created by using a larger particle. However, when 0.2  $\mu\text{m}$  of magnetic particles were attached to the DNA hairpins, there was no change in fluorescence intensity after applying the magnetic field (Figure 4-7A). The smaller magnetic particles experienced smaller magnetic force because of the saturation of their magnetic susceptibility, which was insufficient to unzip the hairpin structure. The average signal enhancement of different DNA hairpins and magnetic particles is summarized in Table 4-2.

In addition, a control experiment was performed by using 6ds hairpins attached to 5  $\mu\text{m}$  silica particles. The results demonstrated that the fluorescence signal did not change after cycling the external magnetic field (Figure 4-7D), confirming that the

fluorescence intensity change from the previous system was not an artificial signal and hairpins tethered to magnetic beads can be manipulated by the applied magnetic field.

### **Conclusion**

In conclusion, a magnetically driven DNA nanomotor using DNA hairpins conjugated to magnetic particles has been successfully demonstrated. Specifically, DNA hairpins with different numbers of base pairs in the stem were synthesized. One end of the DNA hairpin was immobilized on the glass surface of a micro-channel and the other end was attached to iron oxide particles. An external magnetic field was then applied to pull the iron oxide particles away from the glass surface. This pulling force opens the hairpin, as observed by an increased fluorescence signal, and is interpreted as the power stroke. Removal of the magnetic field reforms the closed state of DNA hairpins, as observed by decreased fluorescence signal, and represents the recovery stroke. Motorization of the nanodevice results from the cyclical shrinking and extending movements. This DNA nanomotor holds promise for a new class of nanomachines that can be operated by magnetic field without any additional DNA strands as fuels. In addition, using magnetic field to control the movement of molecules can also avoid molecular damage from photonic fluxes, which in contrast to previous photoregulated DNA nanomotors.

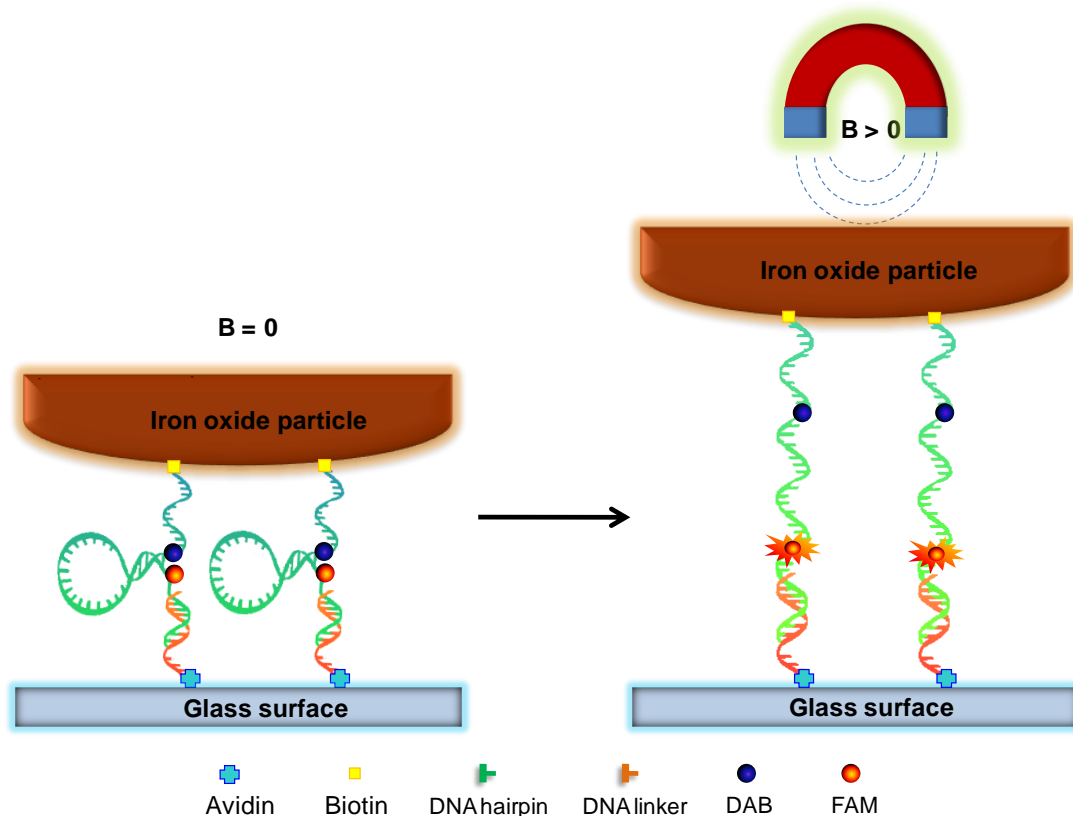


Figure 4-1. Concept of magnetically driven DNA nanomotor.<sup>152</sup> One end of DNA hairpins were immobilized on a glass surface and the other conjugated to magnetic particles. DNA hairpins molecules were opened by an external magnetic field gradient and subsequently closed through DNA hybridization after the removal of the magnetic field. We interpret the separation of the 5' and 3' ends of the DNA hairpin during opening as the power stroke of our nanomotor and the hybridization of the hairpin as the recovery stroke.

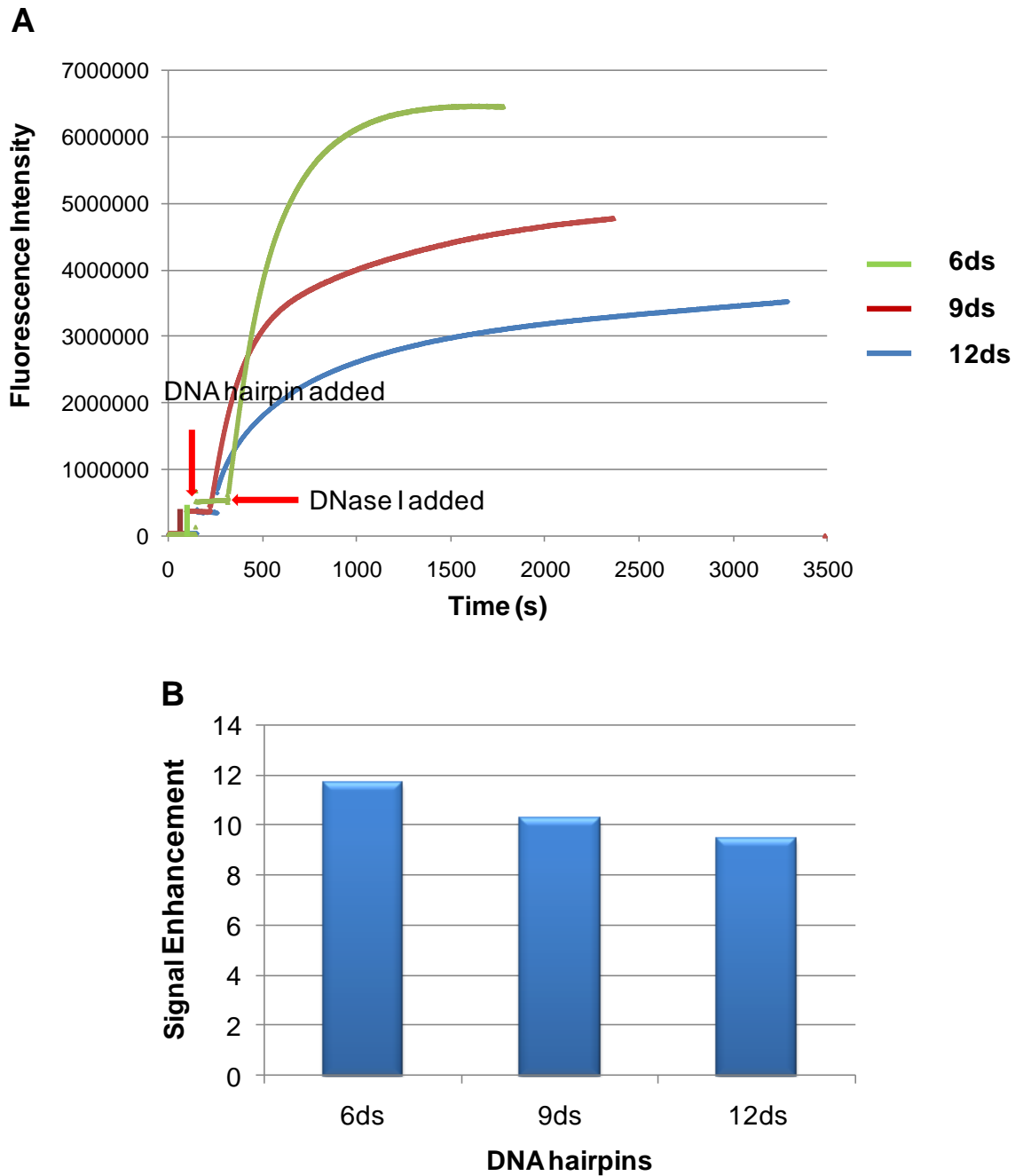


Figure 4-2. Signal enhancement of DNA hairpins in solution after the addition of DNase I.<sup>152</sup> Fluorescence emission at 520 nm was measured for the DNA hairpins after DNase I addition: [DNA hairpin] = 100nM, DNase I = 2000 U/mL, and buffer is 20 mM Tris-HCl buffer pH 7.4, Na<sup>+</sup> = 100 nM, Mg<sup>2+</sup> = 10 mM

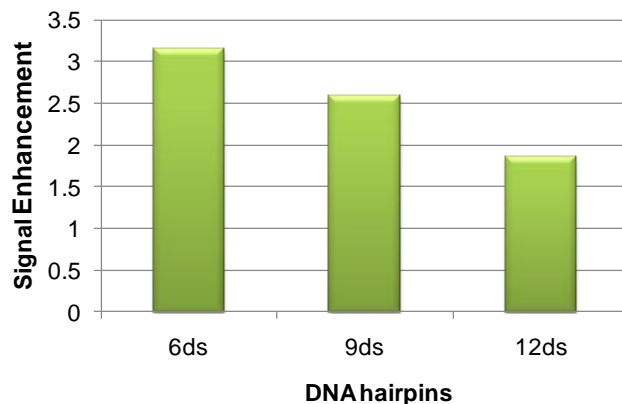


Figure 4-3. Signal enhancement of DNA hairpins on the glass surface of micro-channel after DNase I addition.<sup>152</sup> Fluorescence emission at 520 nm was measured for the DNA hairpins after DNase I addition: [DNA hairpin] = 5 $\mu$ M, DNase I = 2000 U/mL, and buffer is 20 mM Tris-HCl buffer pH 7.4, Na<sup>+</sup> = 100 nM, Mg<sup>2+</sup> = 10 mM

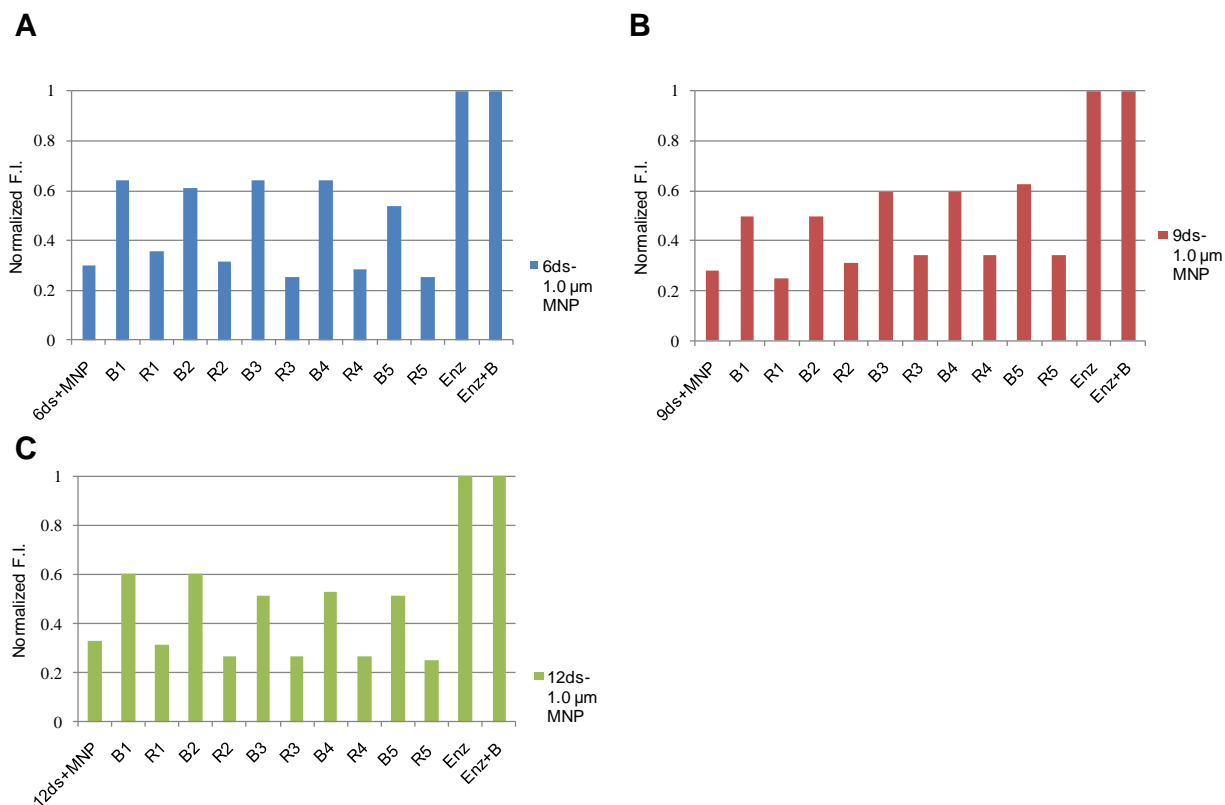


Figure 4-4. Cycles of closed-open state from DNA hairpins with 6 (A), 9 (B), and 12 (C) base pairs, respectively, conjugated with 1.0  $\mu$ m magnetic beads.<sup>152</sup> The cycles were demonstrated by repeated application (Bn) and removal (Rn) of the magnetic field.

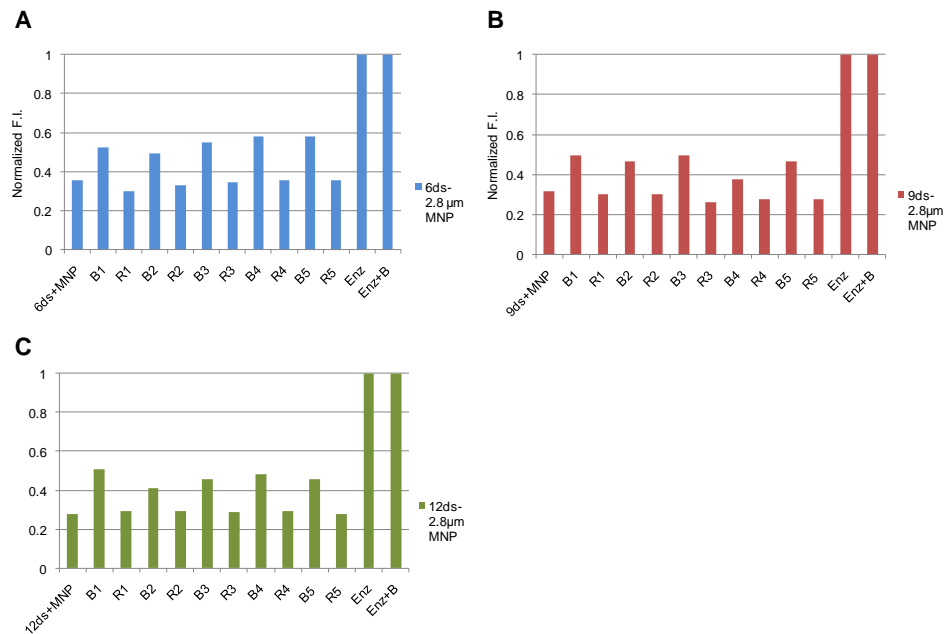


Figure 4-5. Cycles of closed-open state from DNA hairpins with 6 (A), 9 (B), and 12 (C) base pairs, respectively, conjugated with 2.8 μm magnetic beads.<sup>152</sup> The cycles were represented by repeated application (Bn) and removal (Rn) of the magnetic field.

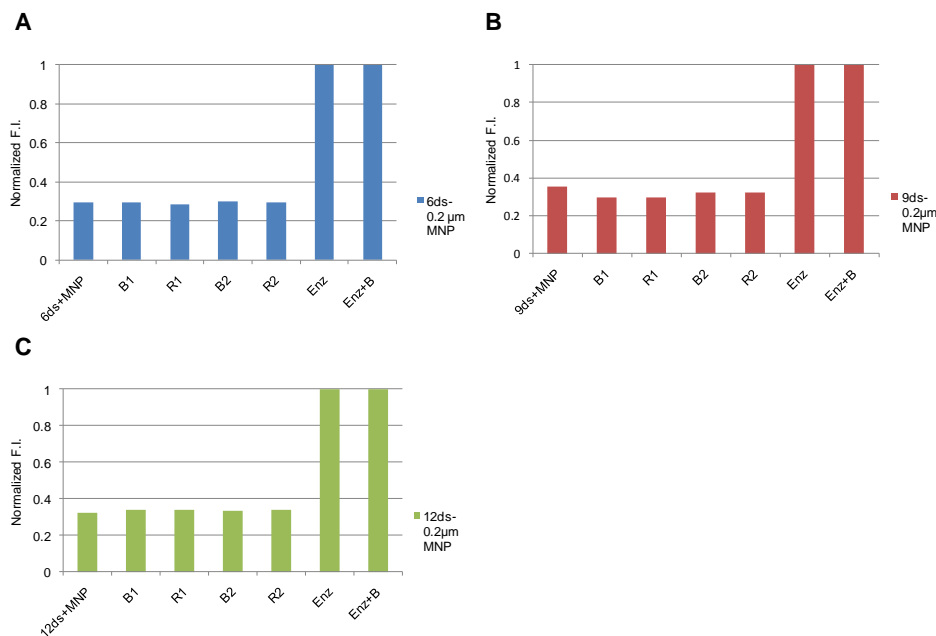


Figure 4-6. Cycles of closed-open state from DNA hairpins with 6 (A), 9 (B), and 12 (C) base pairs, respectively, conjugated with 0.2 μm magnetic beads.<sup>152</sup> The cycles were demonstrated by repeated application (Bn) and removal (Rn) of the magnetic field.

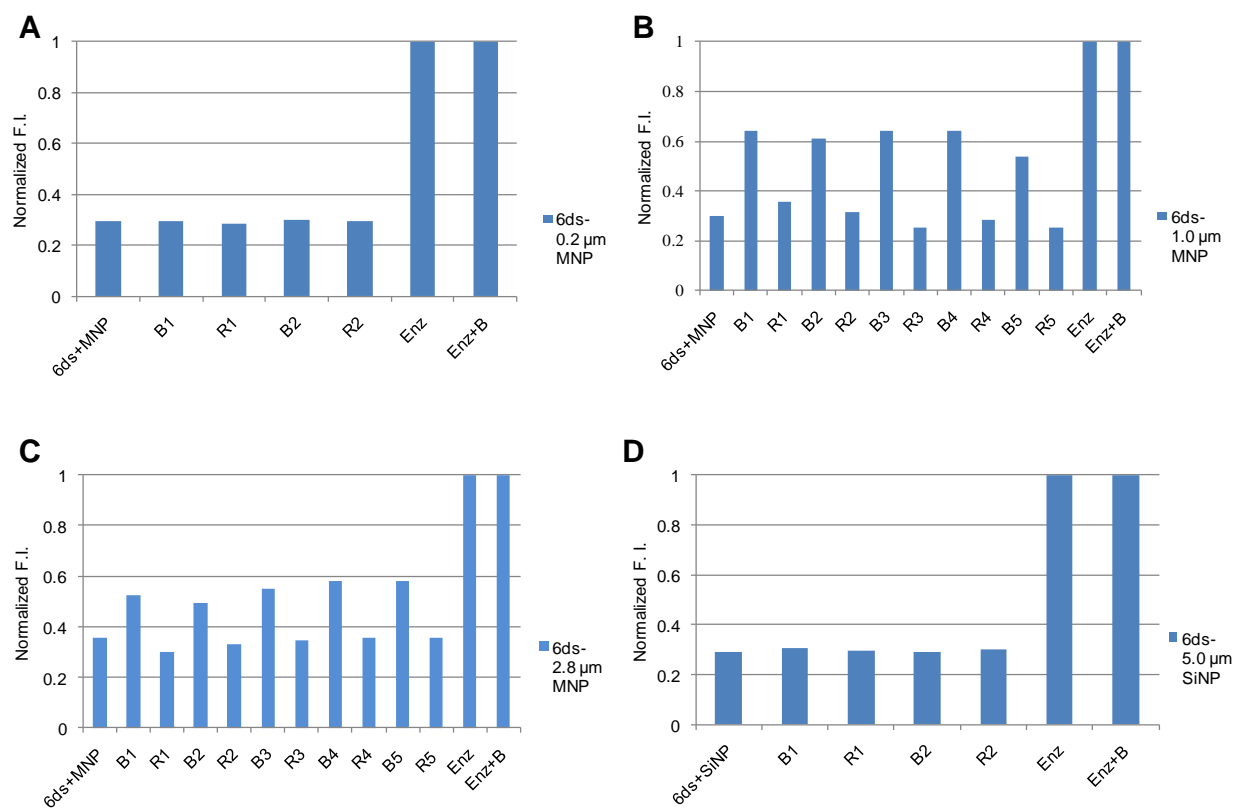


Figure 4-7. Magnetic beads effect on the DNA nanomotor.<sup>152</sup> Cycles of closed-open state from 6 base pair DNA hairpins; (a) 0.2  $\mu$ m, (b) 1.0  $\mu$ m, and (c) 2.8  $\mu$ m magnetic particle; (d) a control experiment using 5.0  $\mu$ m silica particle.

Table 4-1. DNA hairpins and biotinylated linker. Stem bases are underlined.

DNA hairpins	Melting <sup>a</sup> Temperature (C°)
6ds 5'- TGG TGT GGT TGG TGG TTT -FAM- <u>CCA</u> <u>TCG</u> TTT TTT TTT TTT TTT TTT TTC <u>GAT</u> <u>GG</u> - DAB-T TTT TTT TTT TTT TTT TTT T-T-Biotin-3'	66.5
9ds 5'- TGG TGT GGT TGG TGG TTT -FAM- <u>CCG</u> <u>CCA</u> <u>TCG</u> TTT TTT TTT TTT TTT TTT TTC <u>GAT</u> <u>GGC</u> <u>GG</u> -DAB-T TTT TTT TTT TTT TTT TTT T- Biotin-3'	68.9
12ds 5'- TGG TGT GGT TGG TGG TTT -FAM- <u>CCG</u> <u>CCG</u> <u>CCA</u> <u>TCG</u> TTT TTT TTT TTT TTT TTT TTC <u>GAT</u> <u>GGC</u> <u>GGC</u> <u>GG</u> -DAB-T TTT TTT TTT TTT TTT TTT T- Biotin-3'	70.8
Linker 5'- CCA CCA ACC ACA CCA TTT TTT TTT T- Biotin-3'	

a Calculated melting temperature from IDT website

Table 4-2. The average signal enhancement of nanomotor after repeating several cycles.

MNP	Signal Enhancement		
	6ds	9ds	12ds
2.8µm	1.7	1.6	1.4
1.0µm	2.1	2.0	1.8
0.2µm	No change	No change	No change

## CHAPTER 5 SUMMARY AND FUTURE DIRECTIONS

### **The Development of DNA-Conjugated Magnetic Nanoparticles for Bio-Analytical and Biomedical Applications**

Great efforts have been made toward the improvement of highly sensitive and selective medical diagnostic tools to meet the demand for rapid and accurate disease screening, especially for cancer. Nanomaterials, whose properties can be tuned by size and shape, are used not only in material science but also in the translation of nanotechnology to medical practice. Specifically, magnetic nanoparticles (MNPs) have attracted the attention of scientists as multimodal nanoplatforms with both diagnostic and therapeutic functionalities. Owing to their large surface-to-volume ratios and magnetic properties, selective recognition elements, including oligonucleotides, can be loaded onto MNPs' surfaces for targeting, separating, and imaging. Besides carrying genetic information, DNA is renowned for the specificity of Watson-Crick base pairing, which provides highly specific molecular recognition and enables programmed sequences and structures.

Integration of MNPs and DNA to construct hybrid materials has led to the development of advanced bioanalysis tools and fabrication of novel DNA-based nanomachines. In this research, three key projects have been demonstrated: 1) molecular profiling of cancer cells using aptamer-conjugated magnetic nanoparticles; 2) detection of lysozyme using magnetic relaxation switches based on aptamer-functionalized superparamagnetic nanoparticles; 3) magnetically driven single DNA nanomotor.

We first applied DNA aptamers conjugated to MNPs as magnetic nanosensors based on the magnetic relaxation switch (MRSw) mechanism. Aptamer conjugated

MNPs (ACMNPs) switched from their original dispersed to aggregated states upon binding with target cells. The aggregation induced the formation of magnetic clusters generating the coupling of magnetic moments and resulting in a decrease in the spin-spin relaxation times ( $T_2$ ) of the surrounding water protons. The change in  $T_2$  ( $\Delta T_2$ ) indicated the binding of ACMNPs to their target cells. The synergism between the large surface area of MNPs and the high specificity of aptamers played a key role in high selectivity and sensitivity. The magnetic nanosensors were able to detect as few as 10 target cancer cells in both buffer and biological media, as well as in a mixture of cells. Additionally, a molecular profiling of cancer cells was designed by using an array of ACMNPs. Due to different affinity of aptamers to each cell type, distinct recognition patterns were generated allowing the accurate identification of cancer cells.

The expansion of MRSw-based nanosensors was demonstrated for protein detection. Lysozyme which has high affinity for its aptamer was selected as a model protein. In this system, MNPs were conjugated with either aptamers or linker DNA that could hybridize to the extended part of aptamers leading to magnetic cluster formation. The presence of targets induced the base-pair disruption of aptamers resulting in the disassembly of pre-existing clusters and an increase in  $T_2$ . The high selectivity and sensitivity of detection was achieved in both buffer and serum. The successful identification of lysozyme in cancer cell lysates was also demonstrated.

These studies validated the potential of using DNA-conjugated MNPs as magnetic nanosensors for a wide range of molecular targets. With low magnetic background, high sensitivity was achieved in biological samples without separation, purification, amplification and washing steps. Furthermore, the detection could be performed using a

bench top relaxometer, which provides rapid results, and easy to operate. Considering these advantages, this method is feasible for clinical diagnostics.

Besides using DNA-conjugated MNPs as bioanalysis tools, a DNA-based nanomachine driven by magnetic fields was also demonstrated. DNA hairpins were selected to serve as a dynamic part of the molecular motor due to their ability to shrink and extend by external stimuli. DNA hairpins were immobilized onto a glass surface and then conjugated to magnetic particles. The application of an external magnetic field triggered the switch of molecular conformation between closed and open states. The movement of a nanomotor could be tracked by the change of fluorescence from the intercalated fluorophore and quencher in DNA hairpin structures. By repetitive shrinking and extending movements, DNA hairpins were considered as a nanometer-scale motor.

Overall, this research mainly focused on the development of DNA-conjugated MNPs for cancer detection and the fabrication of DNA-based nanomotor. A successful outcome from these studies will lead to advanced hybrid nanomaterials for bioanalysis, biomedical applications, and bionanomaterial research.

### **Future Directions**

Although magnetic nanosensors have shown advantages in simple and sensitive detection, they still have some limitations. In chapter 3, we demonstrated that the presence of targets triggered the disassembly of magnetic nanoclusters and the  $T_2$  increase was observed. However, a small numbers of targets may not be sufficient to induce the disassembly of pre-existing clusters. Typically, a certain number of analyte molecules is always needed to disrupt magnetic clusters and generate significant changes in  $T_2$ , thus limiting sensitivity of detection. In order to improve the efficiency of

magnetic nanosensors for rare target detection, an enzymatic reaction could be incorporated into magnetic nanosensors for signal amplification.

It has been found that DNA also has catalytic activity and can catalyze a number of biochemical reactions, including RNA or DNA cleavage, ligation, and DNA-self modification.<sup>126,153</sup> Catalytically active DNA molecules are known as deoxyribozymes or DNAzymes and can be obtained by the SELEX process.<sup>154,155</sup> Typically, catalytic activities of DNAzymes are dependent on metal-ions, especially transition-metal ions. DNAzymes that are specific for  $\text{Pb}^{2+}$ ,<sup>156</sup>  $\text{Cu}^{2+}$ ,<sup>157</sup>  $\text{Zn}^{2+}$ ,<sup>158</sup> and  $\text{Co}^{2+}$ <sup>159</sup> have been reported. Compared to RNA molecules or proteins, DNAzymes are much more stable, and the synthesis, as well as modification, is relatively easy. Consequently, DNAzymes are used as analytical tools for metal ion detections.<sup>160</sup>

By taking advantage of DNAzymes' catalytic activity and their ease of synthesis and modification, we are attempting to apply DNAzymes into magnetic nanosensors system. The  $\text{Pb}^{2+}$ -dependent DNAzyme is selected due to its relatively high catalytic efficiency and structural stability,<sup>156</sup> and is designed to have 7 extended bases in order to hybridize with a part of the lysozyme aptamer (as shown in Figure 7-1). The twelve base-pairs between DNAzyme and aptamer can maintain stable duplex at room temperature. To assemble magnetic nanoclusters, the DNAzyme substrate containing a single RNA linkage (rA) as the cleavage site is extended on both ends by 12 bases to be complementary to the linker DNA attached to MNPs. In the presence of lysozyme targets, aptamers undergo structural change and DNAzymes are released. By the addition of pre-existing magnetic nanoclusters having substrates as linkers, the released DNAzymes recognize and cleave the substrates inducing cluster disassembly.

After cleavage, DNazymes can leave the cleaved substrates and catalyze the cleavage of other nearby substrates. In this way, the catalytic reaction can cycle several times with only a few target molecules. Consequently, disassembly of magnetic nanoclusters can be triggered, resulting in an increase in  $T_2$ . With DNazyme's catalytic activity, ease of synthesis, and sequence modification, combined with the flexibility of the MRSw to sense various types of targets, it is very likely that DNazyme-based magnetic nanosensors will become highly efficient bioanalysis tools for clinical applications.

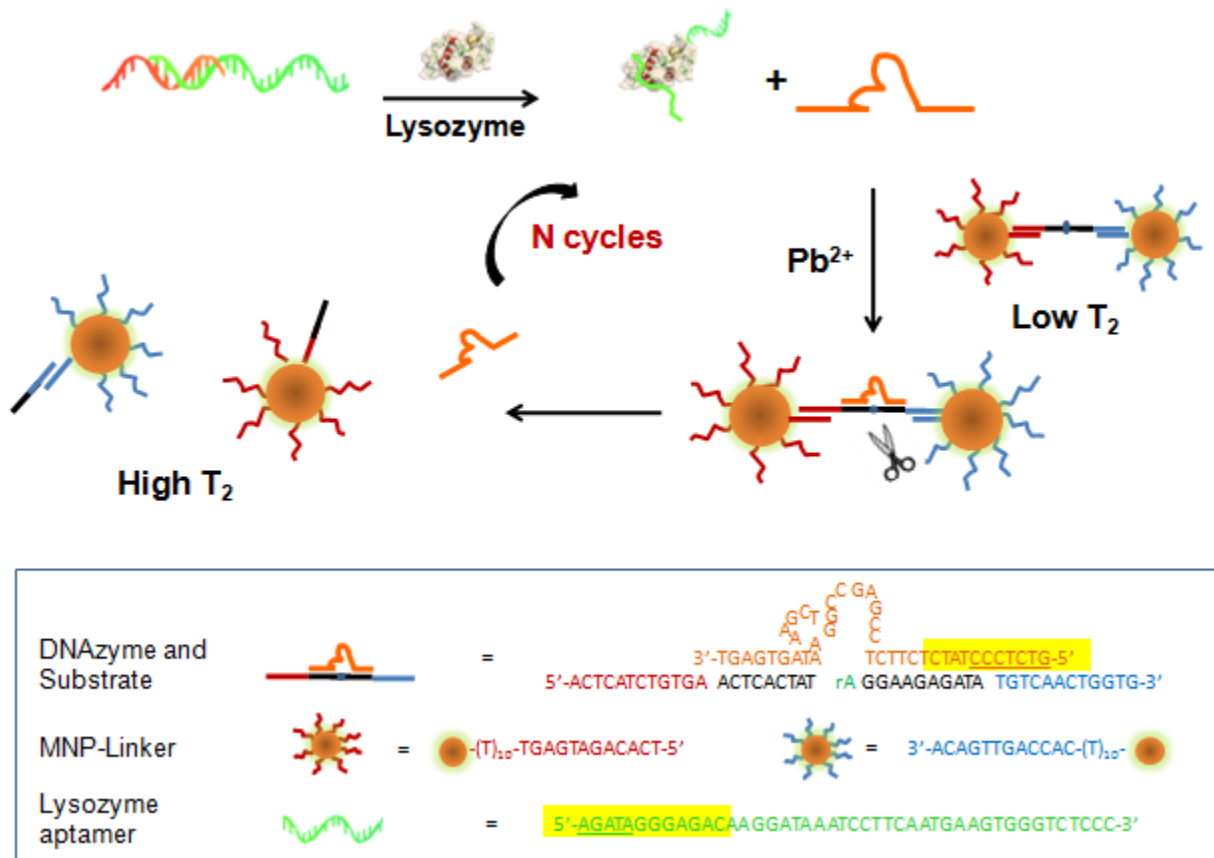


Figure 7-1. Schematic representation of DNAzyme-based magnetic nanosensor for Lys detection. The sequences of DNAzyme, substrate, linker, and Lys aptamer are shown. The underlined based are the extended parts of either DNAzyme or aptamer. The highlight demonstrates the complementary parts between DNAzyme and aptamer.

## LIST OF REFERENCES

- (1) Alivisatos, A. P. *Science* **1996**, *271*, 933.
- (2) Daniel, M. C.; Astruc, D. *Chem. Rev.* **2004**, *104*, 293.
- (3) Wang, H.; Yang, R.; Yang, L.; Tan, W. *ACS nano* **2009**, *3*, 2451.
- (4) Cheon, J.; Lee, J. H. *Acc. Chem. Res.* **2008**, *41*, 1630.
- (5) Hirschfeld, T.; Callis, J. B.; Kowalski, B. R. *Science* **1984**, *226*, 312.
- (6) Elghanian, R.; Storhoff, J. J.; Mucic, R. C.; Letsinger, R. L.; Mirkin, C. A. *Science* **1997**, *277*, 1078.
- (7) Cao, Y. C.; Jin, R.; Nam, J. M.; Thaxton, C. S.; Mirkin, C. A. *J. Am. Chem. Soc.* **2003**, *125*, 14676.
- (8) Seeman, N. C. *Nature* **2003**, *421*, 427.
- (9) Yang, D.; Campolongo, M. J.; Nhi Tran, T. N.; Ruiz, R. C.; Kahn, J. S.; Luo, D. *Wiley Interdiscip. Rev. Nanomed. Nanobiotechnol.* **2010**, *2*, 648.
- (10) Yurke, B.; Turberfield, A. J.; Mills, A. P., Jr.; Simmel, F. C.; Neumann, J. L. *Nature* **2000**, *406*, 605.
- (11) Tian, Y.; Mao, C. *J. Am. Chem. Soc.* **2004**, *126*, 11410.
- (12) Shin, J. S.; Pierce, N. A. *J. Am. Chem. Soc.* **2004**, *126*, 10834.
- (13) Yin, P.; Yan, H.; Daniell, X. G.; Turberfield, A. J.; Reif, J. H. *Angew. Chem. Int. Ed.* **2004**, *43*, 4906.
- (14) Green, S. J.; Lubrich, D.; Turberfield, A. J. *Biophys. J.* **2006**, *91*, 2966.
- (15) Jun, Y. W.; Seo, J. W.; Cheon, J. *Acc. Chem. Res.* **2008**, *41*, 179.
- (16) Jun, Y. W.; Lee, J. H.; Cheon, J. *Angew. Chem. Int. Ed.* **2008**, *47*, 5122.
- (17) Morales, M. P.; Veintemillas-Verdaguer, S.; Montero, M. I.; Serna, C. J.; Roig, A.; Casas, L.; Martinez, B.; Sandiumenge, F. *Chem. Mater.* **1999**, *11*, 3058.
- (18) Laurent, S.; Forge, D.; Port, M.; Roch, A.; Robic, C.; Vander Elst, L.; Muller, R. N. *Chem. Rev.* **2008**, *108*, 2064.
- (19) Minelli, C.; Lowe, S. B.; Stevens, M. M. *Small* **2010**, *6*, 2336.

- (20) Gupta, A. K.; Gupta, M. *Biomaterials* **2005**, *26*, 3995.
- (21) Jolivet, J. P.; Chaneac, C.; Tronc, E. *Chem. Commun.* **2004**, 481.
- (22) Babes, L.; Denizot, B.; Tanguy, G.; Le Jeune, J. J.; Jallet, P. *J. Colloid Interface Sci.* **1999**, *212*, 474.
- (23) Griбанov, N. M.; Bibik, E. E.; Buzunov, O. V.; Naumov, V. N. *J. Magn. Magn. Mater.* **1990**, *85*, 7.
- (24) Hyeon, T.; Lee, S. S.; Park, J.; Chung, Y.; Na, H. B. *J. Am. Chem. Soc.* **2001**, *123*, 12798.
- (25) Vincent, B.; Edwards, J.; Emmett, S.; Jones, A. *Colloids Surf.* **1986**, *18*, 261.
- (26) Molday, R. S.; MacKenzie, D. *J. Immunol. Methods* **1982**, *52*, 353.
- (27) Kohler, N.; Fryxell, G. E.; Zhang, M. *J. Am. Chem. Soc.* **2004**, *126*, 7206.
- (28) Stober, W.; Fink, A.; Bohn, E. *J. Colloid Interface Sci.* **1968**, *26*, 62.
- (29) Turney, K.; Drake, T. J.; Smith, J. E.; Tan, W.; Harrison, W. W. *Rapid Commun. Mass Spectrom.* **2004**, *18*, 2367.
- (30) Lindberg, R.; Sjoblom, J.; Sundholm, G. *Colloids and Surfaces a-Physicochemical and Engineering Aspects* **1995**, *99*, 79.
- (31) Yamauchi, H.; Ishikawa, T.; Kondo, S. *Colloids Surf.* **1989**, *37*, 71.
- (32) Sun, E. Y.; Josephson, L.; Kelly, K. A.; Weissleder, R. *Bioconjugate Chem.* **2006**, *17*, 109.
- (33) Wang, L., Wang, K., Santra, S., Zhao, X., Hilliard, L. R., Smith, J. E., Wu, Y., Tan, W. *Anal. Chem.* **2006**, *78*, 646.
- (34) Vanbladeren, A.; Imhof, A.; Hage, W.; Vrij, A. *Langmuir : the ACS journal of surfaces and colloids* **1992**, *8*, 1514.
- (35) Vanbladeren, A.; Vrij, A. *J. Colloid Interface Sci.* **1993**, *156*, 1.
- (36) Inouye, K.; Endo, R.; Otsuka, Y.; Miyashiro, K.; Kaneko, K.; Ishikawa, T. *J. Phys. Chem.* **1982**, *86*, 1465.
- (37) Calvin, S.; Carpenter, E. E.; Harris, V. G. *Phys. Rev. B* **2003**, *68*.

- (38) Haun, J. B.; Yoon, T. J.; Lee, H.; Weissleder, R. *Wiley Interdiscip. Rev. Nanomed. Nanobiotechnol.* **2010**, *2*, 291.
- (39) Kotitz, R.; Matz, H.; Trahms, L.; Koch, H.; Weitschies, W.; Rheinlander, T.; Semmler, W.; Bunte, T. *IEEE T Appl Supercon* **1997**, *7*, 3678.
- (40) Baselt, D. R.; Lee, G. U.; Natesan, M.; Metzger, S. W.; Sheehan, P. E.; Colton, R. J. *Biosens. Bioelectron.* **1998**, *13*, 731.
- (41) Graham, D. L.; Ferreira, H. A.; Freitas, P. P.; Cabral, J. M. *Biosens. Bioelectron.* **2003**, *18*, 483.
- (42) Aytur, T.; Foley, J.; Anwar, M.; Boser, B.; Harris, E.; Beatty, P. R. *J. Immunol. Methods* **2006**, *314*, 21.
- (43) Koenig, S. H.; Kellar, K. E. *Magnetic resonance in medicine : official journal of the Society of Magnetic Resonance in Medicine / Society of Magnetic Resonance in Medicine* **1995**, *34*, 227.
- (44) Maeda, H.; Fang, J.; Inutsuka, T.; Kitamoto, Y. *Int. Immunopharmacol.* **2003**, *3*, 319.
- (45) Lee, H.; Lee, E.; Kim do, K.; Jang, N. K.; Jeong, Y. Y.; Jon, S. *J. Am. Chem. Soc.* **2006**, *128*, 7383.
- (46) Sun, C.; Veisoh, O.; Gunn, J.; Fang, C.; Hansen, S.; Lee, D.; Sze, R.; Ellenbogen, R. G.; Olson, J.; Zhang, M. *Small* **2008**, *4*, 372.
- (47) Lee, J. H.; Huh, Y. M.; Jun, Y. W.; Seo, J. W.; Jang, J. T.; Song, H. T.; Kim, S.; Cho, E. J.; Yoon, H. G.; Suh, J. S.; Cheon, J. *Nat. Med.* **2007**, *13*, 95.
- (48) Xu, C.; Xie, J.; Ho, D.; Wang, C.; Kohler, N.; Walsh, E. G.; Morgan, J. R.; Chin, Y. E.; Sun, S. *Angew. Chem. Int. Ed.* **2008**, *47*, 173.
- (49) Koh, I.; Josephson, L. *Sensors* **2009**, *9*, 8130.
- (50) Demas, V.; Lowery, T. J. *New J Phys* **2011**, *13*.
- (51) Kaittanis, C.; Santra, S.; Santiesteban, O. J.; Henderson, T. J.; Perez, J. M. *J. Am. Chem. Soc.* **2011**, *133*, 3668.
- (52) Grimm, J.; Perez, J. M.; Josephson, L.; Weissleder, R. *Cancer Res.* **2004**, *64*, 639.
- (53) Lee, H.; Sun, E.; Ham, D.; Weissleder, R. *Nat. Med.* **2008**, *14*, 869.

- (54) Lee, H.; Yoon, T. J.; Weissleder, R. *Angew. Chem. Int. Ed.* **2009**, *48*, 5657.
- (55) Tan, W.; Wang, K.; Drake, T. J. *Curr. Opin. Chem. Biol.* **2004**, *8*, 547.
- (56) Yang, C. J.; Jockusch, S.; Vicens, M.; Turro, N. J.; Tan, W. *Proc. Natl. Acad. Sci. U. S. A.* **2005**, *102*, 17278.
- (57) Tan, L.; Li, Y.; Drake, T. J.; Moroz, L.; Wang, K.; Li, J.; Munteanu, A.; Chaoyong, J. Y.; Martinez, K.; Tan, W. *The Analyst* **2005**, *130*, 1002.
- (58) Shangguan, D.; Li, Y.; Tang, Z.; Cao, Z. C.; Chen, H. W.; Mallikaratchy, P.; Sefah, K.; Yang, C. J.; Tan, W. *Proc. Natl. Acad. Sci. U. S. A.* **2006**, *103*, 11838.
- (59) Baron, R.; Willner, B.; Willner, I. *Chem. Commun.* **2007**, 323.
- (60) Willner, I.; Baron, R.; Willner, B. *Biosens. Bioelectron.* **2007**, *22*, 1841.
- (61) Gellert, M.; Lipsett, M. N.; Davies, D. R. *Proc. Natl. Acad. Sci. U. S. A.* **1962**, *48*, 2013.
- (62) Leroy, J. L.; Gueron, M.; Mergny, J. L.; Helene, C. *Nucleic Acids Res.* **1994**, *22*, 1600.
- (63) Winfree, E.; Liu, F.; Wenzler, L. A.; Seeman, N. C. *Nature* **1998**, *394*, 539.
- (64) Liu, D.; Wang, M.; Deng, Z.; Walulu, R.; Mao, C. *J. Am. Chem. Soc.* **2004**, *126*, 2324.
- (65) Bath, J.; Turberfield, A. J. *Nature nanotechnology* **2007**, *2*, 275.
- (66) Beissenhertz, M. K.; Willner, I. *Org. Biomol. Chem.* **2006**, *4*, 3392.
- (67) Simmel, F. C.; Dittmer, W. U. *Small* **2005**, *1*, 284.
- (68) Liu, H.; Liu, D. *Chem. Commun.* **2009**, 2625.
- (69) Litman, G. W.; Rast, J. P.; Shablott, M. J.; Haire, R. N.; Hulst, M.; Roess, W.; Litman, R. T.; Hinds-Frey, K. R.; Zilch, A.; Amemiya, C. T. *Mol. Biol. Evol.* **1993**, *10*, 60.
- (70) Conrad, R.; Keranen, L. M.; Ellington, A. D.; Newton, A. C. *J. Biol. Chem.* **1994**, *269*, 32051.
- (71) Macaya, R. F.; Schultze, P.; Smith, F. W.; Roe, J. A.; Feigon, J. *Proc. Natl. Acad. Sci. U. S. A.* **1993**, *90*, 3745.

- (72) Famulok, M.; Mayer, G. *Curr. Top. Microbiol. Immunol.* **1999**, *243*, 123.
- (73) Hicke, B. J.; Marion, C.; Chang, Y. F.; Gould, T.; Lynott, C. K.; Parma, D.; Schmidt, P. G.; Warren, S. *J. Biol. Chem.* **2001**, *276*, 48644.
- (74) Sefah, K.; Shangguan, D.; Xiong, X.; O'Donoghue, M. B.; Tan, W. *Nature protocols* **2010**, *5*, 1169.
- (75) Seeman, N. C. *J. Theor. Biol.* **1982**, *99*, 237.
- (76) Pohl, F. M.; Jovin, T. M. *J. Mol. Biol.* **1972**, *67*, 375.
- (77) Mao, C.; Sun, W.; Shen, Z.; Seeman, N. C. *Nature* **1999**, *397*, 144.
- (78) Howard, J.; Hudspeth, A. J.; Vale, R. D. *Nature* **1989**, *342*, 154.
- (79) Turberfield, A. J.; Mitchell, J. C.; Yurke, B.; Mills, A. P., Jr.; Blakey, M. I.; Simmel, F. C. *Phys. Rev. Lett.* **2003**, *90*, 118102.
- (80) SantaLucia, J., Jr. *Proc. Natl. Acad. Sci. U. S. A.* **1998**, *95*, 1460.
- (81) Liu, H.; Xu, Y.; Li, F.; Yang, Y.; Wang, W.; Song, Y.; Liu, D. *Angew. Chem. Int. Ed.* **2007**, *46*, 2515.
- (82) Liu, D.; Bruckbauer, A.; Abell, C.; Balasubramanian, S.; Kang, D. J.; Klenerman, D.; Zhou, D. *J. Am. Chem. Soc.* **2006**, *128*, 2067.
- (83) Liedl, T.; Olapinski, M.; Simmel, F. C. *Angew. Chem. Int. Ed.* **2006**, *45*, 5007.
- (84) Kang, H.; Liu, H.; Phillips, J. A.; Cao, Z.; Kim, Y.; Chen, Y.; Yang, Z.; Li, J.; Tan, W. *Nano Lett.* **2009**, *9*, 2690.
- (85) Lakowicz, J. R. *Principles of fluorescence spectroscopy*, 3rd ed.; Springer, 2006.
- (86) Okamoto, M.; Wada, O.; Tanaka, F.; Hirayama, S. *J. Phys. Chem. A* **2001**, *105*, 566.
- (87) Denicola, A.; Souza, J. M.; Radi, R.; Lissi, E. *Arch. Biochem. Biophys.* **1996**, *328*, 208.
- (88) Lakowicz, J. R. *J. Biochem. Biophys. Methods* **1980**, *2*, 91.
- (89) Jayaraman, S.; Verkman, A. S. *Biophys. Chem.* **2000**, *85*, 49.

- (90) Sontag, B.; Reboud, A. M.; Divita, G.; Di Pietro, A.; Guillot, D.; Reboud, J. P. *Biochemistry (Mosc)*. **1993**, *32*, 1976.
- (91) Wasylewski, M.; Malecki, J.; Wasylewski, Z. *J. Protein Chem.* **1995**, *14*, 299.
- (92) Tyagi, S.; Bratu, D. P.; Kramer, F. R. *Nat. Biotechnol.* **1998**, *16*, 49.
- (93) Stryer, L. *Annu. Rev. Biochem* **1978**, *47*, 819.
- (94) Gordon, G. W.; Berry, G.; Liang, X. H.; Levine, B.; Herman, B. *Biophys. J.* **1998**, *74*, 2702.
- (95) Awais, M.; Sato, M.; Sasaki, K.; Umezawa, Y. *Anal. Chem.* **2004**, *76*, 2181.
- (96) Lei, G.; MacDonald, R. C. *Biophys. J.* **2003**, *85*, 1585.
- (97) Morrison, L. E.; Stols, L. M. *Biochemistry (Mosc)*. **1993**, *32*, 3095.
- (98) Walter, N. G.; Hampel, K. J.; Brown, K. M.; Burke, J. M. *The EMBO journal* **1998**, *17*, 2378.
- (99) Tyagi, S.; Kramer, F. R. *Nat. Biotechnol.* **1996**, *14*, 303.
- (100) Na, H. B.; Song, I. C.; Hyeon, T. *Adv. Mater.* **2009**, *21*, 2133.
- (101) Brody, E. N.; Gold, L. *J. Biotechnol.* **2000**, *74*, 5.
- (102) Ellington, A. D.; Szostak, J. W. *Nature* **1990**, *346*, 818.
- (103) Tuerk, C.; Gold, L. *Science* **1990**, *249*, 505.
- (104) Osborne, S. E.; Matsumura, I.; Ellington, A. D. *Curr. Opin. Chem. Biol.* **1997**, *1*, 5.
- (105) Nutiu, R.; Li, Y. *Angew. Chem. Int. Ed.* **2005**, *44*, 1061.
- (106) Gossuin, Y.; Gillis, P.; Hocq, A.; Vuong, Q. L.; Roch, A. *Wiley Interdiscip. Rev. Nanomed. Nanobiotechnol.* **2009**, *1*, 299.
- (107) Weissleder, R.; Moore, A.; Mahmood, U.; Bhorade, R.; Benveniste, H.; Chiocca, E. A.; Basilion, J. P. *Nat. Med.* **2000**, *6*, 351.
- (108) Zhao, M.; Beauregard, D. A.; Loizou, L.; Davletov, B.; Brindle, K. M. *Nat. Med.* **2001**, *7*, 1241.

- (109) Liu, W.; Dahnke, H.; Jordan, E. K.; Schaeffter, T.; Frank, J. A. *NMR Biomed.* **2008**, *21*, 242.
- (110) Perez, J. M.; Josephson, L.; O'Loughlin, T.; Hogemann, D.; Weissleder, R. *Nat. Biotechnol.* **2002**, *20*, 816.
- (111) Yigit, M. V.; Mazumdar, D.; Lu, Y. *Bioconjugate Chem.* **2008**, *19*, 412.
- (112) Kaittanis, C.; Naser, S. A.; Perez, J. M. *Nano Lett.* **2007**, *7*, 380.
- (113) Perez, J. M.; Simeone, F. J.; Saeki, Y.; Josephson, L.; Weissleder, R. *J. Am. Chem. Soc.* **2003**, *125*, 10192.
- (114) Kaittanis, C.; Santra, S.; Perez, J. M. *J. Am. Chem. Soc.* **2009**, *131*, 12780.
- (115) Fang, X.; Tan, W. *Acc. Chem. Res.* **2010**, *43*, 48.
- (116) Herr, J. K.; Smith, J. E.; Medley, C. D.; Shangguan, D.; Tan, W. *Anal. Chem.* **2006**, *78*, 2918.
- (117) Smith, J. E.; Medley, C. D.; Tang, Z.; Shangguan, D.; Lofton, C.; Tan, W. *Anal. Chem.* **2007**, *79*, 3075.
- (118) Deng, T.; Li, J.; Zhang, L. L.; Jiang, J. H.; Chen, J. N.; Shen, G. L.; Yu, R. Q. *Biosens. Bioelectron.* **2010**, *25*, 1587.
- (119) Medley, C. D.; Smith, J. E.; Tang, Z.; Wu, Y.; Bamrungsap, S.; Tan, W. *Anal. Chem.* **2008**, *80*, 1067.
- (120) Shangguan, D.; Cao, Z.; Meng, L.; Mallikaratchy, P.; Sefah, K.; Wang, H.; Li, Y.; Tan, W. *J. Proteome Res.* **2008**, *7*, 2133.
- (121) Chen, Y.; O'Donoghue, M. B.; Huang, Y. F.; Kang, H.; Phillips, J. A.; Chen, X.; Estevez, M. C.; Yang, C. J.; Tan, W. *J. Am. Chem. Soc.* **2010**, *132*, 16559.
- (122) Tang, Z.; Shangguan, D.; Wang, K.; Shi, H.; Sefah, K.; Mallikaratchy, P.; Chen, H. W.; Li, Y.; Tan, W. *Anal. Chem.* **2007**, *79*, 4900.
- (123) Sefah, K.; Tang, Z. W.; Shangguan, D. H.; Chen, H.; Lopez-Colon, D.; Li, Y.; Parekh, P.; Martin, J.; Meng, L.; Phillips, J. A.; Kim, Y. M.; Tan, W. H. *Leukemia : official journal of the Leukemia Society of America, Leukemia Research Fund, U.K* **2009**, *23*, 235.
- (124) Sefah, K.; Meng, L.; Lopez-Colon, D.; Jimenez, E.; Liu, C.; Tan, W. *PLoS One* **2010**, *5*, e14269.

- (125) Shangguan, D.; Meng, L.; Cao, Z. C.; Xiao, Z.; Fang, X.; Li, Y.; Cardona, D.; Witek, R. P.; Liu, C.; Tan, W. *Anal. Chem.* **2008**, *80*, 721.
- (126) Liu, J.; Cao, Z.; Lu, Y. *Chem. Rev.* **2009**, *109*, 1948.
- (127) Jain, P. K.; Huang, X.; El-Sayed, I. H.; El-Sayed, M. A. *Acc. Chem. Res.* **2008**, *41*, 1578.
- (128) Hunter, T. *Cell* **2000**, *100*, 113.
- (129) von Ahsen, O.; Bomer, U. *Chembiochem : a European journal of chemical biology* **2005**, *6*, 481.
- (130) Cohen, P. *Nature reviews. Drug discovery* **2002**, *1*, 309.
- (131) Levinson, S. S.; Elin, R. J.; Yam, L. *Clin. Chem.* **2002**, *48*, 1131.
- (132) Harrison, J. F.; Lunt, G. S.; Scott, P.; Blainey, J. D. *Lancet* **1968**, *1*, 371.
- (133) Klockars, M.; Reitamo, S.; Weber, T.; Kerttula, Y. *Acta Med. Scand.* **1978**, *203*, 71.
- (134) Cox, J. C.; Ellington, A. D. *Biorg. Med. Chem.* **2001**, *9*, 2525.
- (135) Wang, B.; Yu, C. *Angew. Chem. Int. Ed.* **2010**, *49*, 1485.
- (136) Saito, N. *Leuk. Lymphoma* **1990**, *2*, 347.
- (137) Leculier, C.; Couprie, N.; Francina, A.; Archimbaud, E.; Adeleine, P.; Treille, D.; Denoyel, G.; Fiere, D. *Blood* **1992**, *79*, 760.
- (138) Bray, D. *Cell Movement: from Molecules to Motility (2<sup>nd</sup> Edition)*; Garland publishing, 2001.
- (139) Schliwa, M.; Woehlke, G. *Nature* **2003**, *422*, 759.
- (140) Muller, B. K.; Reuter, A.; Simmel, F. C.; Lamb, D. C. *Nano Lett.* **2006**, *6*, 2814.
- (141) Tian, Y.; He, Y.; Chen, Y.; Yin, P.; Mao, C. *Angew. Chem. Int. Ed.* **2005**, *44*, 4355.
- (142) Bath, J.; Green, S. J.; Turberfield, A. J. *Angew. Chem. Int. Ed.* **2005**, *44*, 4358.
- (143) Li, J. J., Tan, W. *Nano Lett.* **2002**, *2*, 4.
- (144) Chen, Y.; Wang, M.; Mao, C. *Angew. Chem. Int. Ed.* **2004**, *43*, 3554.

- (145) Fang, X.; Li, J. J.; Perlette, J.; Tan, W.; Wang, K. *Anal. Chem.* **2000**, *72*, 747A.
- (146) Liu, X.; Farmerie, W.; Schuster, S.; Tan, W. *Anal. Biochem.* **2000**, *283*, 56.
- (147) Strick, T. R.; Allemand, J. F.; Bensimon, D.; Bensimon, A.; Croquette, V. *Science* **1996**, *271*, 1835.
- (148) Chiou, C. C., Huang, Y. Y., CHIANG, M. H., Lee, H. H., Lee, G. B. *Nanotechnology* **2006**, *17*, 8.
- (149) Lang, M. J.; Fordyce, P. M.; Engh, A. M.; Neuman, K. C.; Block, S. M. *Nat. Methods* **2004**, *1*, 133.
- (150) Huang, H.; Dong, C. Y.; Kwon, H. S.; Sutin, J. D.; Kamm, R. D.; So, P. T. *Biophys. J.* **2002**, *82*, 2211.
- (151) Hosu, B. G.; Jakab, K.; Banki, P.; Toth, F. I.; Forgacs, G. *Rev. Sci. Instrum.* **2003**, *74*, 4158.
- (152) Bamrungsap, S.; Phillips, J. A.; Xiong, X.; Kim, Y.; Wang, H.; Liu, H.; Hebard, A.; Tan, W. *Small* **2011**, *7*, 601.
- (153) Willner, I.; Shlyahovsky, B.; Zayats, M.; Willner, B. *Chem. Soc. Rev.* **2008**, *37*, 1153.
- (154) Breaker, R. R. *Nat. Biotechnol.* **1997**, *15*, 427.
- (155) Breaker, R. R. *Science* **2000**, *290*, 2095.
- (156) Breaker, R. R.; Joyce, G. F. *Chem. Biol.* **1994**, *1*, 223.
- (157) Cuenoud, B.; Szostak, J. W. *Nature* **1995**, *375*, 611.
- (158) Santoro, S. W.; Joyce, G. F.; Sakthivel, K.; Gramatikova, S.; Barbas, C. F., 3rd *J. Am. Chem. Soc.* **2000**, *122*, 2433.
- (159) Mei, S. H.; Liu, Z.; Brennan, J. D.; Li, Y. *J. Am. Chem. Soc.* **2003**, *125*, 412.
- (160) Wang, H.; Kim, Y.; Liu, H.; Zhu, Z.; Bamrungsap, S.; Tan, W. *J. Am. Chem. Soc.* **2009**, *131*, 8221.

## BIOGRAPHICAL SKETCH

Suwussa Bamrungsap was born in Samutsongkhram, in 1981 to Somkuan and Wasana Bamrungsap. She obtained the scholarship from the Development and Promotion of Science and Technology Talent Projects (DPST) to complete her high school at Sriboonyanon School in 1999 and attended Kasetsart University to study Chemistry. After Suwussa received her bachelor's degree with the second class honors in 2003, she continued her master's degree in physical chemistry at Kasetsart University under the supervision of Dr. Jumras Limtrakul. She obtained the scholarship under the National Nanotechnology Center, Thailand from the Royal Thai government and began her Doctorate study under the supervision of Dr. Weihong Tan at the University of Florida in fall 2006. She received her Doctor of Philosophy degree in chemistry in August 2011.